Surface-Sensitive Adsorption of Water and Carbon Dioxide on Magnetite: $Fe_3O_4(111)$ versus $Fe_3O_4(001)$

Vorgelegt von M. Sc. -Chem.
Eman Ahmed Ahmed Mohammed Zaki
ORCID: 0000-0001-6875-2514

von der Fakultät II - Mathematik und Naturwissenschaften
der Technischen Universität Berlin
zur Erlangung des akademischen Grades

Doctor rerum naturalium
(Dr. rer. nat.) im Fach Chemie

genehmigte Dissertation

Promotionsausschuss:

Vorsitzender: Prof. Dr. Peter Hildebrandt Technischen Universität Berlin
Gutachter: Prof. Dr. Hans-Joachim Freund, Fritz-Haber-Institut, MPG
Gutachter: Prof. Dr. Reinhard Schomäcker, Technischen Universität Berlin

Tag der wissenschaftlichen Aussprache: 20. December 2019

Berlin 2020

Diese Dissertation wurde von Februar 2016 bis Juni 2019 in der Abteilung Chemische Physik am Fritz-Haber-Institut der Max-Planck-Gesellschaft unter der Anleitung von Herrn Professor Dr. Hans-Joachim Freund, in der Arbeitsgruppe Struktur und Reaktivität, Gruppenleiter Dr. Shamil Shaikhutdinov, angefertigt.

"The secret of happiness, you see, is not found in seeking more, but in developing the capacity to enjoy less."

Dr. Mostafa Mahmoud

Abstract

The interaction of water with solid surfaces is important in many scientific fields such as corrosion, electrochemistry, geology, and heterogeneous catalysis. Chemistry at water/oxide interfaces plays a crucial role in surface's properties and reactivity. Employing model systems structurally and electronically characterized under well-defined conditions offers deep insights into the chemistry of the water/solid interfaces at an atomic level. This knowledge allows one to tune and optimize catalytic processes.

Its strong relevance to the economical and environmental concerns (climate change) has driven growing worldwide attention to carbon dioxide (CO_2). It is highly desirable to find a promising route to transform CO_2 into valuable chemicals such as fuels for further applications. In this respect, iron oxides were considered as suitable catalysts for activation of CO_2, not only because of their natural abundance, but also due to their important catalytic role in many industrial processes, such as the Fisher-Tropsch synthesis, the Haber process (NH_3 synthesis), and the high-temperature water gas shift reaction.

The Thesis aims to investigate the interaction of water and CO_2 on magnetite (Fe_3O_4) surfaces and the role of water on CO_2 activation. I also investigated the influence of surface orientation ((111) vs (001)) on the adsorption behavior. Well-defined magnetite surfaces were prepared as thin ordered films on metal substrates (Pt(111) and Pt(001)). For structural characterization and reactivity studies we used Temperature Programmed Desorption (TPD), low energy electron diffraction (LEED), Temperature-Programmed LEED (TP LEED), and Infrared Reflection Absorption Spectroscopy (IRAS).

First, I addressed the surface termination of the films using CO as a probe molecule. In the next step, individual adsorption of water and CO_2 was studied. In the case of Fe_3O_4(111), water dissociates resulting in the formation of O_sH and O_wH hydroxyl groups, consisting of oxygen atoms from the magnetite surface (s) and water (w) molecule, respectively. These hydroxyl groups act as an anchor for the incoming water molecules to form a dimer complex, which ultimately forms (2×2) hexagonally ordered structure (seen by LEED) via hydrogen bond network. The latter is proved by DFT calculations to be thermodynamically favorable.

In contrast to the (111) surface, the water molecularly adsorbs on $Fe_3O_4(001)$-$(\sqrt{2} \times \sqrt{2})R45°$. Upon increasing coverage, water molecule starts to partially dissociate which reinforces the interaction between the formed dimer or trimer and the oxide surface. Water ordering directly observed by LEED suggests that the water ad-layer follows the symmetry of iron oxide underneath, thus ice-like layers are formed on (111) and (001) in hexagonal and square symmetry, respectively. This is the first time that water ordering has been experimentally observed in two different structures on the same oxide. We believe that the experimental results provide a strong basis for theoretical calculations of water/oxide interfaces, and can even serve as benchmarks for the investigation of ice nucleation on solid surfaces.

When compared to water, CO_2 molecules are rather weakly interacting with both $Fe_3O_4(111)$ and (001) surfaces. However, strongly bound CO_2 species may be formed as minority species at a low coverage regime, which are, most likely, related to surface defects. Based on isotopic experiments, there is no evidence of CO_2 dissociation. TPD spectra on (111) facet manifest a competition between CO_2 and residual gases (water and CO) from the UHV background. In fact, even traces of water may considerably alter CO_2 interaction with the oxide. Therefore, careful precautions have to be taken while studying CO_2 interaction with the oxide surface. The results show that on the (111) surface, CO_2 may adsorb more strongly in the presence of surface hydroxyls, resulting in CO_2 desorption at 250 K (compared to $\sim$200 K on the clean surface).

According to the TPD results, a water precovered magnetite (001) surface enhances CO_2 interaction, probably via the formation of bicarbonate species which decompose at $\sim$350 K.

We believe that the results presented in this Thesis shed more light on the complex interaction of "simple" molecules with oxide surfaces.

Zusammenfassung

Die Wechselwirkung von Wasser mit festen Oberflächen ist in vielen wissenschaftlichen Bereichen wie Korrosion, Elektrochemie, Geologie und heterogener Katalyse wichtig. Die Chemie an Wasser-Oxid-Grenzflächen spielt eine entscheidende Rolle für die Oberflächeneigenschaften und die Reaktivität. Der Einsatz von strukturell und elektronisch unter definierten Bedingungen charakterisierten Modellsystemen bietet tiefe Einblicke in die Chemie der Wasser-Feststoff-Grenzflächen auf atomarer Ebene. Dieses Wissen ermöglicht es, katalytische Prozesse zu optimieren.

Seine starke Relevanz für die wirtschaftlichen und ökologischen Belange (Klimawandel) hat dazu geführt, dass die weltweite Aufmerksamkeit für Kohlendioxid (CO_2) wächst. Es ist sehr wünschenswert, einen vielversprechenden Weg zu finden, um CO_2 in wertvolle Chemikalien wie Kraftstoffe für weitere Anwendungen zu verwandeln. In diesem Zusammenhang wurden Eisenoxide als geeignete Katalysatoren für die Aktivierung von CO_2 angesehen, nicht nur wegen ihrer großen natürlichen Vorkommen, sondern auch wegen ihrer wichtigen katalytischen Rolle in vielen industriellen Prozessen, wie der Fisher-Tropsch-Synthese, dem Haber-Prozess (NH_3-Synthese), der Hochtemperatur-Wassergas-Shift-Reaktion.

Die Arbeit zielt darauf ab, die Wechselwirkung von Wasser und CO_2 auf Magnetitoberflächen (Fe_3O_4) und die Rolle von Wasser bei der CO_2 Aktivierung zu untersuchen. Ich untersuchte auch den Einfluss der Oberflächenorientierung ((111) vs. (001)) auf das Adsorptionsverhalten. Gut definierte Magnetitoberflächen wurden als dünn geordnete Schichten auf Metallsubstraten (Pt(111) und Pt(001)) hergestellt. Für die Strukturcharakterisierung und Reaktivitätsstudien verwendeten ich Temperaturprogrammierte Desorption (TPD), niederenergetische Elektronenbeugung (LEED), Temperaturprogrammierte LEED (TP LEED) und Infrarot-Reflexionsabsorptionsspektroskopie (IRAS).

Zuerst habe ich mich mit der Oberfläche-Terminierung der Schichten unter Verwendung von CO als Sondenmolekül beschäftigt. Im nächsten Schritt wurde die individuelle Adsorption von Wasser und CO_2 untersucht. Im Falle von $Fe_3O_4(111)$ dissoziiert Wasser, was zur Bildung von O_sH- und O_w

H-Hydroxylgruppen führt, die aus Sauerstoffatomen der Magnetitoberfläche (s) bzw. des Wasser(w)-Moleküls bestehen. Diese Hydroxylgruppen wirken als Anker für die einströmenden Wassermolekülen und bilden einen Dimer-Komplexe, die schließlich über ein Wasserstoffbrücken-Netzwerk eine (2×2) hexagonale geordnete Struktur (gesehen von LEED) bildet. Letzteres wurde durch DFT-Berechnungen als thermodynamisch günstig nachgewiesen.

Im Gegensatz zur (111) Oberfläche adsorbiert Wasser molekular an Fe_3O_4(001)-($\sqrt{2}$ $\sqrt{2}$)R45°. Mit zunehmender Bedeckung beginnen Wassermolekül teilweise zu dissoziieren, was die Wechselwirkung zwischen dem gebildeten Dimer oder Trimer und der Oxidoberfläche verstärkt. Die direkt von LEED beobachtete Wasserordnung deutet darauf hin, dass die Wasseradsorbat-Schicht der Symmetrie des darunter liegenden Eisenoxids folgt, so dass eisartige Schichten auf (111) und (001) in hexagonaler bzw. quadratischer Symmetrie gebildet werden. Es ist das erste Mal, dass die Wasserordnung auf zwei verschiedenen Oberflächen desselben Oxids beobachtet wurde. Wir glauben, dass die experimentellen Ergebnisse eine solide Grundlage für theoretische Berechnungen von Wasser-Oxid-Grenzflächen bilden und sogar als Maßstab für die Untersuchung von Eiskeimbildung auf festen Oberflächen dienen können.

Im Vergleich zu Wasser wechselwirken CO_2-Moleküle eher schwach mit Fe_3O_4(111) und (001) Oberflächen. Allerdings können stark gebundene CO_2-Spezies als Minoritätsspezies bei geringer Bedeckung gebildet werden, die höchstwahrscheinlich mit Oberflächendefekten zusammenhängen. Basierend auf Isotopenversuchen gibt es keine Hinweise auf eine Dissoziation von CO_2. TPD-Spektren auf (111) Facette zeigen eine Konkurrenz zwischen CO_2 und Restgas (Wasser und CO) aus dem UHV-Hintergrund. Tatsächlich können sogar Spuren von Wasser die CO_2-Interaktion mit dem Oxid erheblich verändern. Daher müssen bei der Untersuchung der CO_2-Interaktion mit der Oxidoberfläche sorgfältige Vorsichtsmaßnahmen getroffen werden. Die Ergebnisse zeigen, dass auf der (111) Oberfläche CO_2 stärker in Gegenwart von Oberflächenhydroxylen adsorbieren kann, was zu einer CO_2 Desorption bei 250 K führt (verglichen mit $\sim$ 200 K auf der sauberen Oberfläche).

Gemäß den TPD-Ergebnissen verbessert die wasservorbedeckte Magnetitoberfläche (001) die CO_2-Wechselwirkung, wahrscheinlich durch die Bildung

von Bikarbonatspezies, die sich bei ∼350 K zersetzen.

Wir glauben, dass die in der Dissertation vorgestellten Ergebnisse mehr Licht auf die komplexe Interaktion von "einfachen" Molekülen mit Oxidoberflächen werfen.

Contents

List of Figures

List of Tables

Chapter 1

Introduction

Catalysis refers to the phenomenon (kinetic, not thermodynamic) by which the rate of a chemical process is altered by a substance (the catalyst) which is not appreciably consumed in the process. Based on the phase of the catalyst material and reacting species the catalytic process can be divided into homogeneous catalysis and heterogeneous catalysis. In the latter, the heterogeneous catalyst is present in a different phase from the reactant; commonly, the catalyst is a solid material, while the reactant is in the gaseous or liquid phase. The catalysts are primarily metal and metal oxide-based materials. The catalytic processes are involved in 85 % of processes in the chemical industry, and 80 % of these catalytic process concern heterogeneous catalysis, which makes it an important branch of chemistry.[1]

The application of model systems, particularly in heterogeneous catalysis, has made crucial progress in understanding the behavior of active sites and unraveling fundamental information on various reactions taking place on surfaces. Herein lies the beauty of such systems, as they enable the investigation of the reactivity of catalysts while avoiding the complexity of "real" catalysis.

This thesis is divided into six chapters. Chapter 1 provides a brief introduction to iron oxides especially magnetite Fe_3O_4. The structure of both Fe_3O_4(111) and (001) facets and their termination are included as well. Chapter 2 describes the experimental setup (UHV machine) and explains the fundamental concept of various techniques used in the study. Chapter 3 illustrates the preparation of samples (films), and surface terminations using CO as a probe molecule. Chapter 4 deals with detailed studies of water adsorption

on both Fe_3O_4(111) and (001) films using techniques such as temperature-programmed desorption (TPD), low energy electron diffraction (LEED), and infrared reflection-absorption spectroscopy (IRAS). The adsorption studies of CO_2, and the induced effect of water on it, are also mentioned in Chapter 5. Finally the results and highlights of various studies are summarized in the conclusion section.

1.1 Iron oxides

Iron oxides naturally occur in abundance in the earth's crust. Of the 16 recognized iron oxides and hydroxides [2], magnetite (Fe_3O_4), maghemite (γ-Fe_2O_3), and hematite (α-Fe_2O_3) are the most common forms in nature. Several significant reviews have summarized and highlighted the properties and reactivities of iron oxide, and can be found in Ref. [3–5]. The variety of the structures and properties of iron oxides prove widespread applications. Table 1.1 summarizes a selection of industrial catalytic application of the iron oxides.

Table 1.1: Iron oxide catalysts in industrial reactions. Adapted from ref.[2].

Reaction	**Catalyst or catalyst precursor**
Synthesis of ammonia $N_2 + 3\ H_2 \rightarrow 2\ NH_3$	Fe_3O_4 promoted with Al_2O_3/ K_2O/CaO
Water gas shift reaction $CO + H_2O \rightarrow H_2 + CO_2$	Fe_3O_4/ Cr_2O_3
Fischer-Tropsch synthesis $CO + H_2 \rightarrow$ hydrocarbons + H_2O	Fe_3O_4/5-10% Cr_2O_3 Hematite promoted with SiO_2/K_2O
Dehydrogenation of ethylbenzene to styrene	Hematite/K_2O
Vapour phase oxidation of alcohols to aldehydes and ketones	Hematite/MoO_3
Liquefication of H_2 to 100% parahydrogen	"Hydrated" iron oxides
Steam gasifiaction of brown coal	Ultrafine FeOOH

Magnetite (Fe_3O_4), hematite (α-Fe_2O_3), and wüstite (FeO) are oxides of different stoichiometry, which are formed under specific conditions (oxygen

pressure and temperature) and are easily convertible to each form. Therefore, it is important to control the experimental conditions for preparing a particular form of iron oxides, as shown in the phase diagram (fig.1.1) for iron- oxygen systems. The preparative conditions play a key role in the stoichiometries and the final surface structure of the oxides is either a single crystal or thin film. Figure 1.2 shows a side and a top view of wüstite (FeO), hematite (α-Fe_2O_3), and magnetite (Fe_3O_4) crystal models.

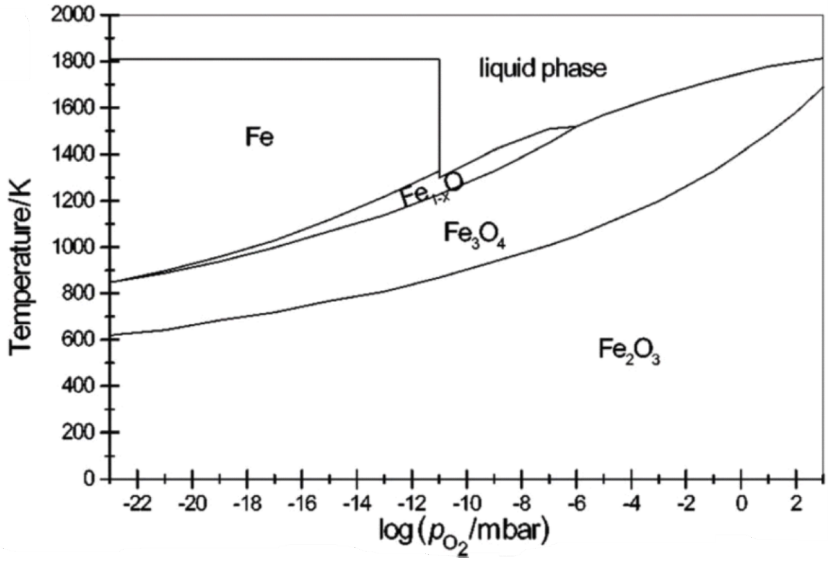

Figure 1.1: Phase diagram of different iron-O_2 systems. Adapted from [6].

Wüstite (FeO), has a cubic unit cell (fcc) consisting of a closely-packed lattice of large oxygen anions, providing octahedral interstitial Fe^{2+} sites. The lattice constant varies between 4.28 $\mathring{A}$ and 4.323 $\mathring{A}$ depending on the stoichiometry.[7] Wüstite has a non-stoichiometric form FeO_{1-x}, (where $(1-x)$ ranges from 0.83 to 0.95),[8]. The non-stoichiometry is occupied by cation vacancies.

Hematite (α-Fe_2O_3) has the corundum structure. The hexagonal unit cell has lattice constants of a = 5.034 $\mathring{A}$ and c = 13.746 $\mathring{A}$.[9] The lattice parameters of synthetic hematite depend on the preparation temperature, i.e. by increasing the temperature from 25 to 100 °C, the lattice a changes from 5.042 to 5.033$\mathring{A}$. [7, 10] However, the naturally grown crystals exhibit six formula units in the hexagonal unit cell due to different contributions of OH.

Since this study focuses on the adsorption behavior of various molecules

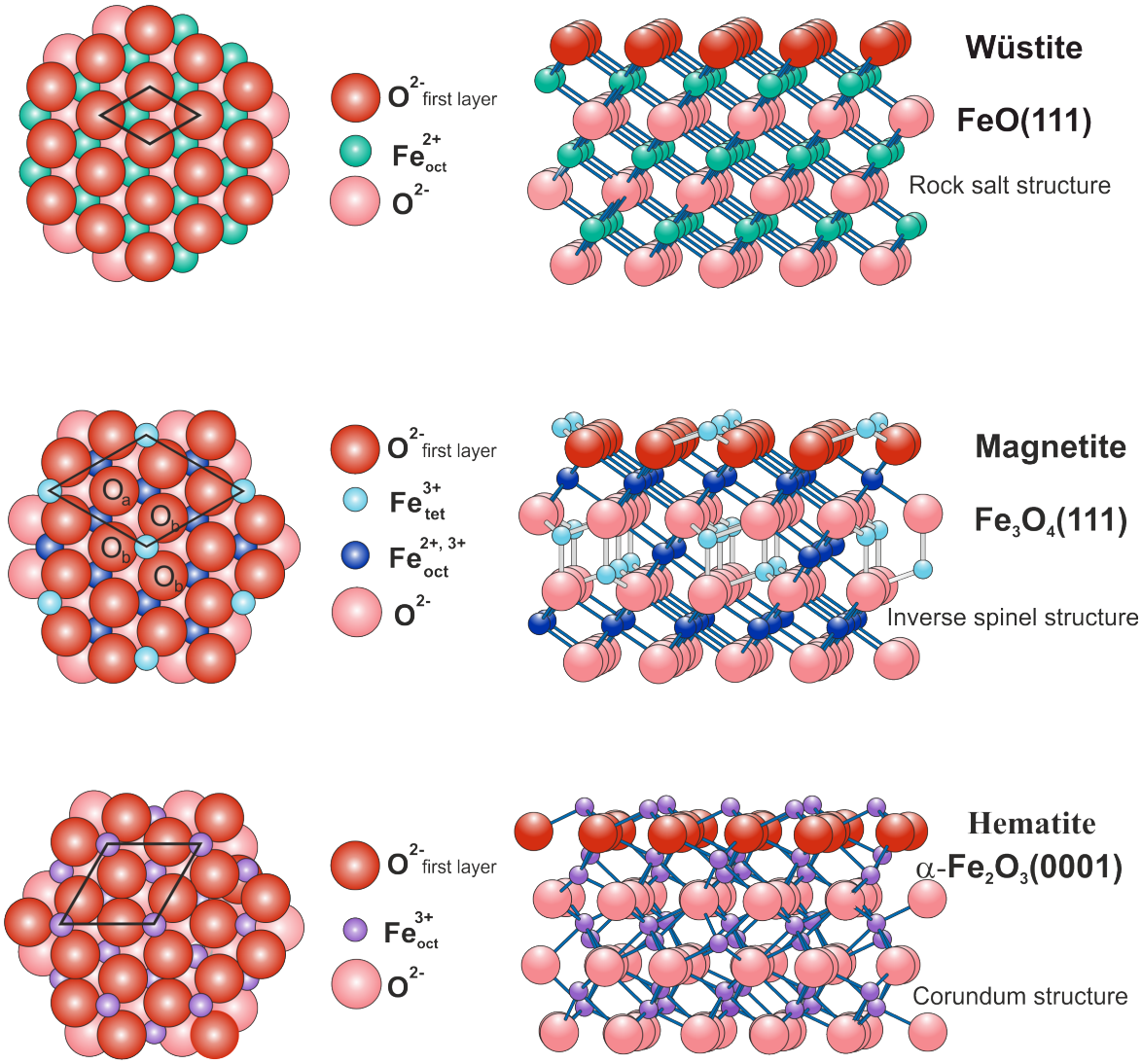

Figure 1.2: The side view (right) and top view (left) of wüstite (FeO), hematite (α-Fe_2O_3), and magnetite (Fe_3O_4) crystals.

on the magnetite, the following part gives a brief introduction to the crystal structure and surface termination (which strongly influences the surface chemistry) of both (111) and(001) facets of magnetite.

1.2 Magnetite

Hercules stone,lodestone, black iron oxide, ferrous ferrite, or magnetic iron ore are all names given to magnetite. Magnetite has important temperatures where its properties alter: i.e., (i) below 120 K, Verwey transition temperature

T_V, the electrical conductivity of magnetite (due to electrons hopping between Fe^{3+} and Fe^{2+} ions in octahedral sites) decreases by two orders of magnitude. Thus it turns into an insulator.[11] (ii) between 120 K and 850 K, T_c, the Curie temperature, magnetite is ferrimagnetic due to the cancellation of ferromagnetic moments on tetrahedral sites by antiferromagnetic moments on octahedral sites.[12] (iii) above 850 K, magnetite exhibits superparamagnetic behavior where net magnetization is zero.[12]

Magnetite has been widely explored for many applications, i.e., spintronics devices[13, 14], in magnetic storage of information,[15], and in heterogeneous catalysis.[16]

Depending on the physical properties, crystal structure, and phase, magnetite has applications in various areas. For instance, the superparamagnetic property of magnetite nanoparticles has been exploited as contrast agents in magnetic resonance imaging (MRI),[17] and as ferrofluids.[2] Besides these, magnetite is also used for drug delivery particularly in cancer treatment.[18]

Magnetite is also used as catalyst in industry, where the water–gas shift (WGS) reaction reaction [19] and the Fischer–Tropsch synthesis of hydrocarbons are involved.[20]

Interestingly, magnetite can serve as a navigational tool, where bacteria synthesize and use it to guide themselves through their preferred environment.[21]

Magnetite crystallizes in the cubic inverse spinel structure and can be written as AB_2O_4 or $Fe^{3+}_{tet}[Fe^{2+}, Fe^{3+}]_{oct}O^{2-}_4$. Where oxygen anions O^{2-} form the close-packed face centered cubic sublattice with Fe^{3+} cations occupy 1/4 of tetrahedral A sites (Fe_{tet1}). Where Fe^{2+} and Fe^{3+} coexist equally and they occupy 2/3 octahederal B sites (Fe_{oct}). The cubic unit cell has a lattice constant of 8.396 $\mathring{A}$.[7]

1.2.1 $Fe_3O_4(111)$

$Fe_3O_4(111)$ (see fig.1.4) is classified as a Tasker type-3 polar surface, consisting of positively charged layers (Fe cations) and negatively charged fcc close-packed oxygen ions ($O^{-2)}$).[23] It exhibits a surface unit cell with a lattice constant $\sim$6 $\mathring{A}$. The stability and electronic structure of the surface terminations have

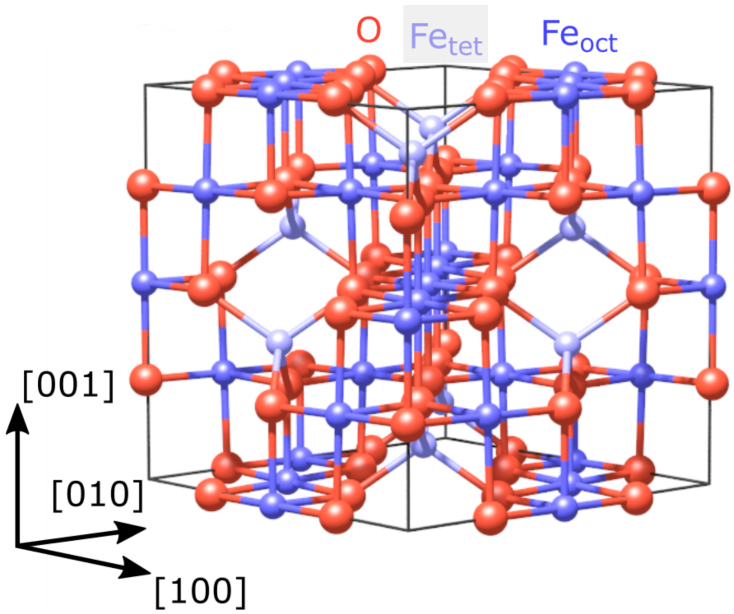

Figure 1.3: The inverse spinel structure of bulk Fe_3O_4. The red, light blue and dark blue colors refer to oxygen anions, tetrahedral Fe cations, and octahedral Fe cations respectively. Adapted from [22].

been experimentally and theoretically investigated.

LEED analysis has been applied to determine the surface structure of $Fe_3O_4(111)$ films [24, 25]. The films exposed a 1/4 monolayer of Fe_{tet1} over a close-packed oxygen layer which is strongly relaxed (see Fig. 1.4(a)). The reliability of this finding has been questioned due to a high Pendry R-factor (R_P=0.46). In another attempt Ritter et al.[26] combined LEED and STM measurement to investigate surface termination. The results, having a Pendry R-factor of R_P=0.20, revealed that the surface terminated by 1/4 ML Fe_{tet1} on top of oxygen (as in fig. 1.4(a)). The authors indicated that the surface relaxation is driven by the minimization of both the electrostatic surface energy and the number of dangling bonds. A further LEED investigation reported by Ritte et al,[26] on $Fe_3O_4(111)$ films, exhibited 1/4 ML tetrahedral termination. A systematic LEED I/V study by Sala et al.[27] illustrated that an Fe_{tet1} terminated surface was obtained after annealing at 900 K in UHV. The results provided a very reasonable R_P factor= $\sim$0.1, and provided strong evidence of the influence that the preparation conditions have on surface structure.

Kim et al.[28] have utilized low energy electron diffraction (LEED), X-ray diffraction (XRD) and STM, concluding that the stable (111) termination

might have oxygen. The results obtained by Shvets et al.[29] show that oxygen terminated surfaces can be formed by cooling the sample in an oxygen atmosphere (10^{-6} Torr) after annealing.

Using scanning tunneling microscopy (STM), Lennie et al.[30] reported two coexisting terminations depending on the surface preparation of $Fe_3O_4(111)$ single crystal. Upon annealing in oxygen (10^{-7} mbar, 1173 K for 30 min), the most stable termination has 3/4 ML of Fe_{oct1} and 1/4 ML of oxygen atoms, revealing single protrusion with 6$\mathring{A}$ periodicity. (The latter model is no longer considered after the same group revised it, observing a so-called "biphase ordering" upon reduction of the crystal surface.[31]) While in the case of annealing in UHV (1973 K for 20 min), the unreconstructed termination has 1/2 ML of iron (Fe_{oct2}-Fe_{tet1}) exposed over a closely packed oxygen layer. The authors suggested that the substrates or surface preparation may explain these differences between the surface models of films and single crystal.

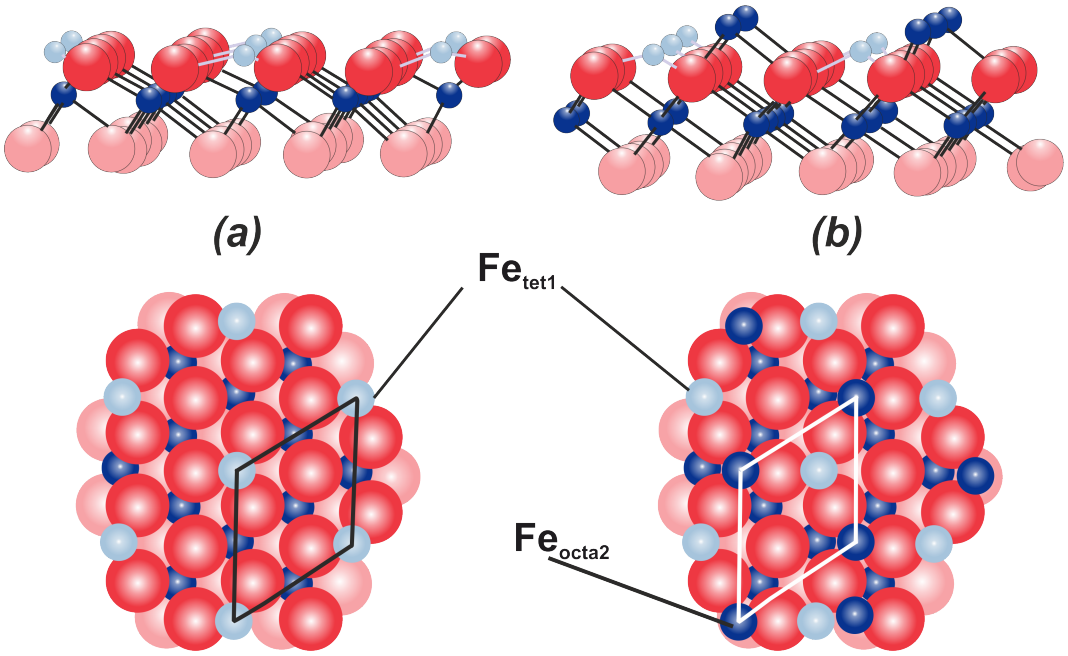

Figure 1.4: Side and top views represent the two terminations of $Fe_3O_4(111)$, under consideration, (a)Fe_{tet1} and (b)Fe_{oct2}. Oxygen anions are red in the topmost layer and light red in the layer underneath. Light blue and dark blue are Fe_{tet1} and Fe_{oct2}, respectively.

Further insights into the surface structure of $Fe_3O_4(111)$ have been provided by adsorption studies. Using CO as a probe molecule, Lemire et al.[32]

studied adsorption by TPD, IRAS, and HREELS. The results illustrated three distinct adsorption states. Depending on the stretching frequencies and desorption temperature (T_d) these states are identified as: α =2115–2140 cm^{-1} (T_d=110 K), β=2080 cm^{-1} (T_d at 180 K), and γ =2207 cm^{-1} (T_d=230 K). The authors have assigned α peak to the physisorption of weakly bound CO, while, the strongly bound CO (chemisorption) β and γ are associated with Fe^{2+} and Fe^{3+} cations, respectively. Due to the observation of divalent Fe cation, the surface was concluded to be octahedrally Fe_{oct2} terminated (see fig. 1.4(b)).

STM investigations of water adsorption on single crystal Fe_3O_4(111) indicated that water dissociation occurs on Fe_{tet1} sites (1/4 ML) (see fig. 1.4(a)).[33]

Certainly, the theoretical approach will be very beneficial in drawing a uniform picture about surface structure and overcoming the experimental challenges. Various groups have conducted research into the surface termination of (111) facet.[34–37] Ahdjoudj et al,[37] have utilized ab initio periodic Hartree-Fock calculations to consider various models. The results reveal that, upon ideal bulk cleavage, Fe_{oct2}-Fe_{tet1} forms the outermost stable layer. In contrast, as a deviation from bulk stoichiometry (the net dipole moment of the entire slab was canceled by imposing the symmetry), Fe_{oct2}-Fe_{tet1}-O is the most stable slab, in which all octahedral and tetrahedral sites are occupied by Fe^{2+} and Fe^{3+}, respectively. The latter suggestion is in agreement with the results obtained by Lemire et al.[32]

Zhu et al.[38] applied the GGA and LDA+U calculations and the results suggested that Fe_{oct2}-Fe_{tet1} is the most stable termination at equilibrium with an oxygen environment. In contrast, the GGA+U approximation, predicted that Fe_{tet1} and Fe_{oct2}-Fe_{tet1} are energetically very close.[39]

Grillo et al., [40] employed a GGA+U approximation and found that, at relevant oxygen pressures at both 300 K and 1200 K, the surface terminated with Fe_{tet1} has the lowest surface energy.

A study of PBE+U calculations shows the chemical potentials obtained under UHV conditions; Fe_{tet1} termination is favoured over Fe_{oct2}. Layer relaxations have also been indicated.[41] These predictions are in good agreement with the results obtained from LEED IV analysis.

As evidenced by the above illustration, there is inconsistency concerning

the surface termination of $Fe_3O_4(111)$. Hence the issue is still under debate.

1.2.2 $Fe_3O_4(001)$

In contrast to the (111), $Fe_3O_4(001)$, single crystals and films, have been experimentally studied by various research groups. These studies show that the (001) facet undergoes a major reconstruction $(\sqrt{2} \times \sqrt{2})R45°$. The surface is B ($Fe_{oct}$) terminated. Many structure models have been proposed (e.g. the distorted bulk truncation (DBT) model) and discussed.[5]

The subsurface cation vacancy (SCV) structure is currently the most accepted model.[42] This proposed SCV model was compiled with a LEED IV investigation, which reported a R_p =0.125. According to the SCV model, the surface is distorted (undulated) by a rearrangement of the cations in the subsurface layers in which, two Fe_{oct2} cations in the third layer are replaced by an additional interstitial Fe_{tet} atom (Fe_{int}) from the second layer. The unit cell thus has one less Fe atom. Eventually, the two surface O atoms (in the first layer) are without a subsurface Fe_{tet} neighbour, per unit cell.

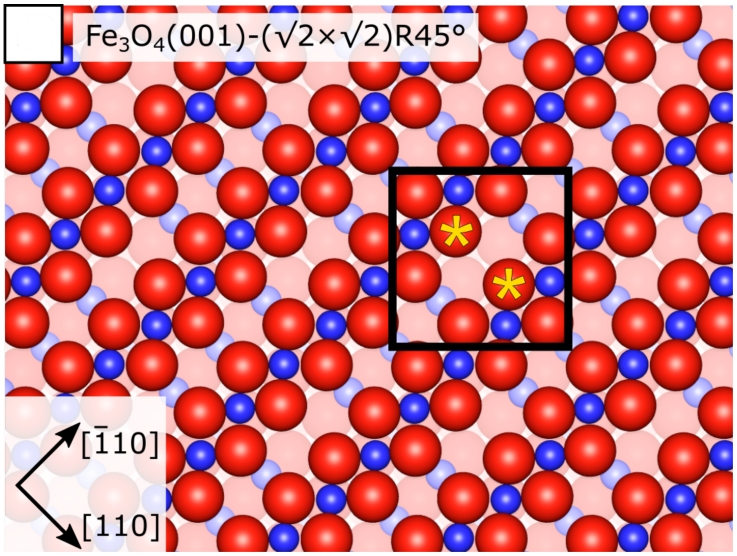

Figure 1.5: $Fe_3O_4(001)$ surface displays $\sqrt{2} \times \sqrt{2})R45°$ reconstruction due to distortion in the arrangement of the surface cations. Fe_{tet1} and Fe_{oct2} are light blue and dark blue respectively. The oxygen is red and a yellow star refers to oxygen anions missing the neighbor subsurface Fe_{tet1}. Adapted from [22]

It must be stressed that, just as for the (111) facet, the preparation

procedure plays an important role in the surface structure of (001) as well. Studies on either single crystals or films have reported the Fe-rich (or Fe-dimer) terminated surfaces. For instance, Parkinson and co-workers [43] have found that such termination (Fe-rich) can occur after sputter/anneal cycles of (001) single crystal, due to the reduction of the surface during Ar^+ sputtering. The authors have suggested that to recover the Fe_{oct}-O termination surface, the final preparation must be to anneal the single crystal at ∼900 K in 10^{-7}-10^{-5} mbar oxygen (O_2).

In the case of growing Fe_3O_4(001) films on Pt(001) crystal, Davis et al. [44] have observed the Fe-rich terminated surface by increasing the Fe buffer layer thickness.

Chapter 2

Methods and Materials

The fundamental investigations in surface science, particularly those concerning model systems, are carried out under ultra-high vacuum (UHV) conditions. This is to enable clean, well-defined surfaces to be prepared and maintained in a contamination-free state during the study. Additionally, it facilitates the use of electron and ion-based experimental surface techniques, allowing electrons to travel without scattering on gas-phase molecules.

This chapter focuses on the experimental setups utilized in this study and also provides an introduction to the applied techniques. However, the preparation of Fe_3O_4 (111) and (001) films will be discussed separately in Chapter 3, due to the importance of the preparation conditions on the surface structure of magnetite.

2.1 Experimental Setup

The experiments presented in this work were performed in two different stainless steel UHV chambers. These chambers are named the "TPD chamber" and the "IRAS chamber" based on the main method implemented there (temperature-programmed desorption, infrared reflection absorption spectroscopy). Let us first consider the TPD chamber in which the majority of work was carried out (see fig.2.1). It is equipped with the following:

• A sputter gun is used to clean the crystal surface by Ar^+ ion bombardment.

• A four-grid optics for low energy electron diffraction (LEED) and also

for Auger electron spectroscopy (AES) (Omicron) to monitor the surface ordering and chemical composition, respectively.

• Electron beam assisted metal evaporators (Focus EFM3) for iron deposition, to prepare the desired samples.

• A quadrupole mass spectrometer (QMS, Hiden Analytical, HAL 301/3F) for temperature-programmed desorption (TPD) experiments. The QMS is shielded by a gold-plated cone to minimize signals from the sample heating stage. In TPD measurements, the samples were kept 1 mm away from the nozzle.

• A "high- pressure" reactor cell (HP cell, ∼30 ml, Au-plated Cu massive block), for reactivity investigations under realistic pressure (as shown in fig. 2.2 (b)). A Viton O-ring located at the top of HP reactor fits the flange at the end of the manipulator and is used to seal the HP cell during experiments to avoid breaking the vacuum in the chamber.

• A gas chromatograph (GC, Agilent Technologies) connected to the HP cell via the gas line in order to control the composition of the gas and the reaction kinetics.

In addition, a system of gas lines facilities the handling of multiple gases of high purity (fig. 2.2). Argon (Ar, Linde), carbon monoxide (CO, Linde), oxygen ($^{16}O_2$ and $^{18}O_2$ from Campro Scientific), carbon dioxide (CO_2, Linde; Carbon Dioxide-97 atom % ^{18}O, Campro Scientific) and water ((Deuterium Oxide "100", min. 99.96% D, D_2O^{16}, Sigma-Aldrich); D_2O^{18} (Deuterium Oxide labeled, Sigma-Aldrich)) are the main gases used during the study. Before CO_2 gas is admitted to the chamber, it passes through a cold trap (a mixture of liquid nitrogen and KCl (saturated solution)) to minimize impurities, particularly water. Before water (D_2O) is used, it is degassed in series of freeze–pump–thaw cycles. The gases are introduced to the chamber either by a directional gas doser (10 μm pin-hole in the Mo foil) of the King-Wells type [45] or by a manual leak-valve (back-filling). Before dosing any gas, the whole gas line is "washed" with this gas several times and pumped to avoid gas contamination from the gas line walls. The pressure in the gas line and inside the UHV chamber is monitored by Varian ionization gauge.

The UHV regime is achieved by a combination of pumps, specifically a rotary pump, a Pfeiffer turbomolecular pump, and a Varian titanium (Ti) sub-

limation pump and a Varian ion pump. Water, H_2, CO, CO_2 and hydrocarbons are the predominant residuals gases.

At room temperature, the internal chamber instruments and walls continually desorb gases, particularly water, leading to an increase in the base pressure. Therefore, the entire system is baked out at temperature in excess of 130 °C for 48 hours. Ultimately the chamber pressure decreases to 2×10^{-10} mbar.

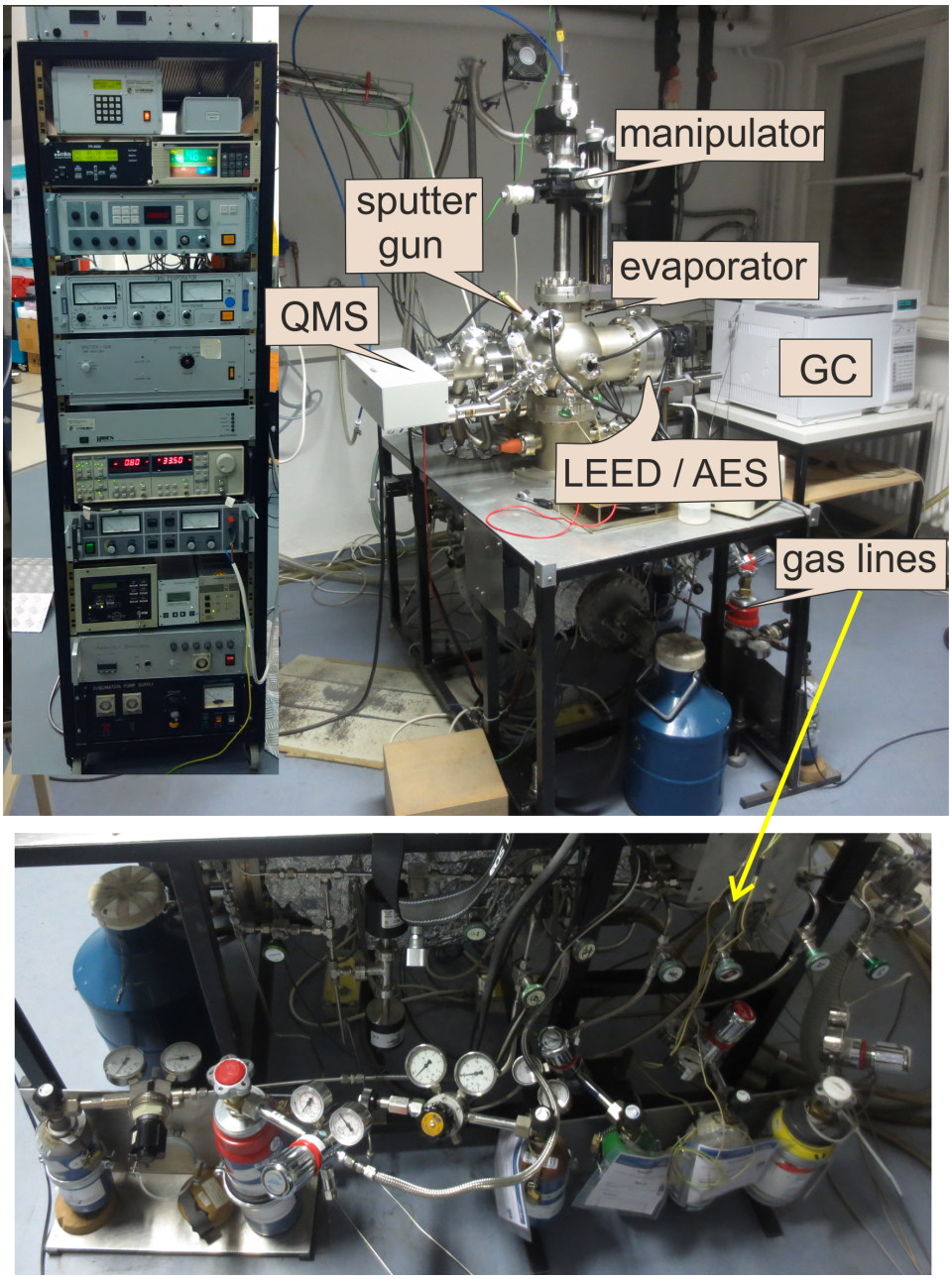

Figure 2.1: Picture of the experimental setup (TPD-chamber).

The rotatable manipulator is vertically central to the chamber and can be moved in x-, y-, and z directions enabling the sample to approach all the equipment.

Figure 2.2 (a) shows the sample holder. A crystal polished on one side (Pt(111) or Pt(001) of 1.5 mm in thickness and 10 mm in diameter) is spot-

welded to a tantalum wire (0.25 mm), on the edge of the crystal, and fixed between two parallel Ta (1 mm) rods. It is possible to heat the sample by resistive heating up to 1400 K. The temperature is monitored by thermocouples (type K, chromel-alumel) spot-welded to the unpolished side (back) of the crystal. For cooling the samples, the manipulator is filled with liquid nitrogen (LN_2). The entire sample holder is connected to the end of the manipulator through a KF-type flange with a four-pin electrical feedthrough.

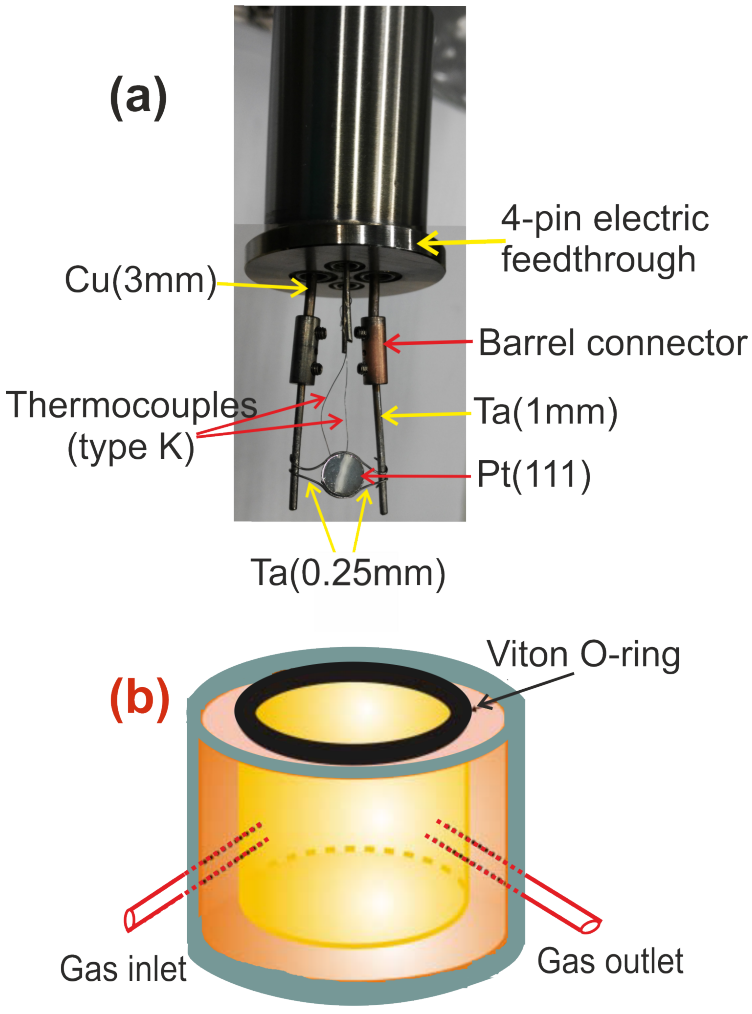

Figure 2.2: (a) The sample holder. (b) Schematic sketch shows the high-pressure cell in the experiment setup.

Secondly, the "IRAS chamber", in which the IR measurements were performed using the Fourier Transform Infrared Spectrometer (Bruker IFS 66v/s), at a grazing angle of 8° and 4 cm^{-1} resolution, which is attached to the UHV

chamber via two KBr windows.

2.1.1 Surface sensitivity

Surface sensitive techniques are mainly aimed to probing those atoms which are located at or near the surface, within a few atomic layers. The majority of such techniques are based on irradiating the surface with photon, electron, or ion beams, and then monitoring the outcome signal. Of course, it is important to ensure that the measured signal originates from the "surface region" more than from the bulk. It is therefore essential to know the penetration depth of the collected data. Figure 2.3 illustrates the relationship between the experimental values of the electron inelastic mean free path for different solid materials and the electron kinetic energy in the range of 5-2000 eV. The inelastic mean free path (IMFP) is defined as the average distance that electrons of a given kinetic energy can travel before suffering from an inelastic (energy loss) collision. Initially, the plot decreases with kinetic energy forming a broad minimum and then slowly increases. The optimum surface sensitivity can be achieved at the minimum of the "universal" curve, where electrons with kinetic energies in the range of 50-100 eV exhibit the lowest mean free path (penetration depth) of ∼0.5-1 nm.

2.1.2 Low energy electron diffraction

Low energy electron diffraction (LEED) is a technique widely used to check the crystallographic structure of well-ordered surfaces. The basic physical principles and many important details about LEED have been described in the literature.[47–50]

In principle, the LEED experiment depends on the duality of electrons.[51] Electrons exhibit both particle and wave characteristics. The de Broglie wavelength (λ) of an electron is given by:

$$\lambda = \frac{h}{\sqrt{2m_e E}} \tag{2.1}$$

where E the energy of the incoming electron beam (roughly at the minimum

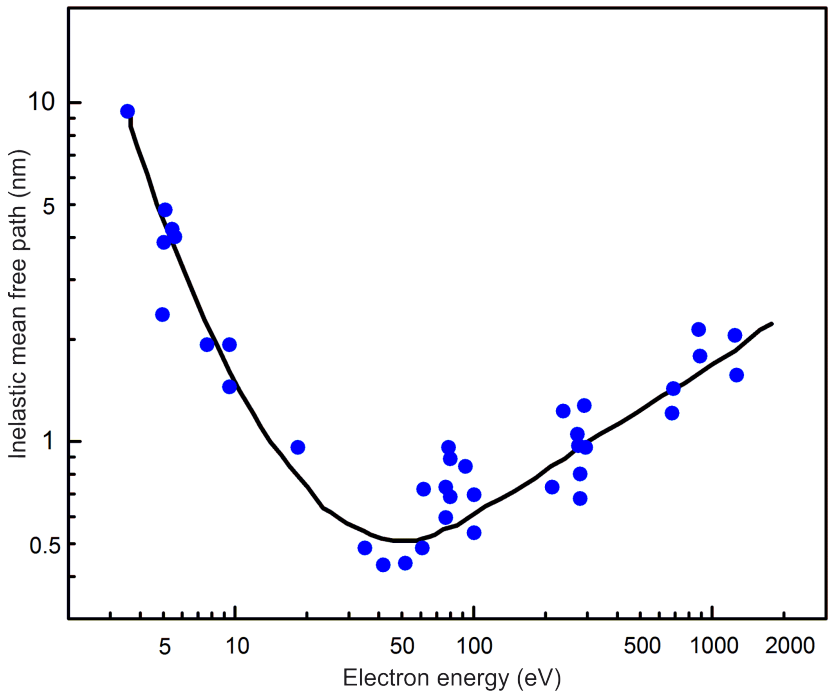

Figure 2.3: Inelastic mean free path as a function of electron energy. Taken from [46].

in the "universal" curve), h is Planck's constant (6.626×10^{-34}Js), m_e is the electron mass (9.11×10^{-31}kg).

The diffraction process (see fig.2.4) is explained by Bragg's law (eq. 2.2).[52] This law illustrates the relationship between the inter-planar spacing between atomic planes ("d-spacing") and the wavelength of the incident beam λ. The latter is given by de Broglie relationship in 2.2.

$$n\,\lambda \;=\; 2dsin\theta \tag{2.2}$$

where n is an integer, θ is the angle between the incident wavevector and the backscattered beam.

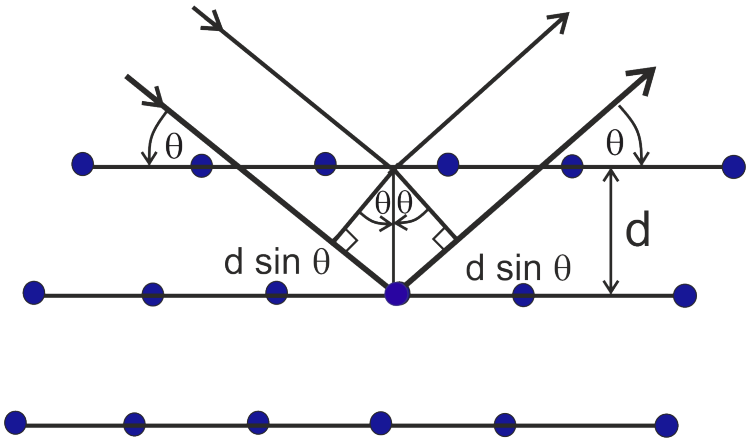

Figure 2.4: Schematic diagram of the diffraction process.

Figure 2.5 depicts the experimental arrangement for LEED, which allows direct observation of the diffraction pattern. The LEED setup comprises an electron gun, a hemispherical fluorescent screen, and 4- hemispherical grids (G_1-G_4). The sample under investigation is positioned in the center of the curvature of these hemispherical grids.

A beam of electrons with energy E (20-200 eV) is generated by the electron gun unit (cathode, a Wehnelt cylinder and electrostatic lenses), and hits the sample surface. The electrons that back-scatter from the sample surface to the grids, are of two kinds, i.e. elastic and inelastic scattering electrons.

(i) The elastic scattered electrons reach the first grid and are accelerated towards a hemispherical fluorescent screen, which is biased at a high positive potential (5 kV). Thus the electrons in the diffracted beams create a pattern of bright LEED spots. Both first and fourth grids are grounded to create a field-free region.

(ii) The inelastically scattered electrons are rejected by the G_2 and G_3 grids, which are kept at a negative potential (suppressor voltage). These electrons may contribute to the background intensity, i.e. diffuse background.

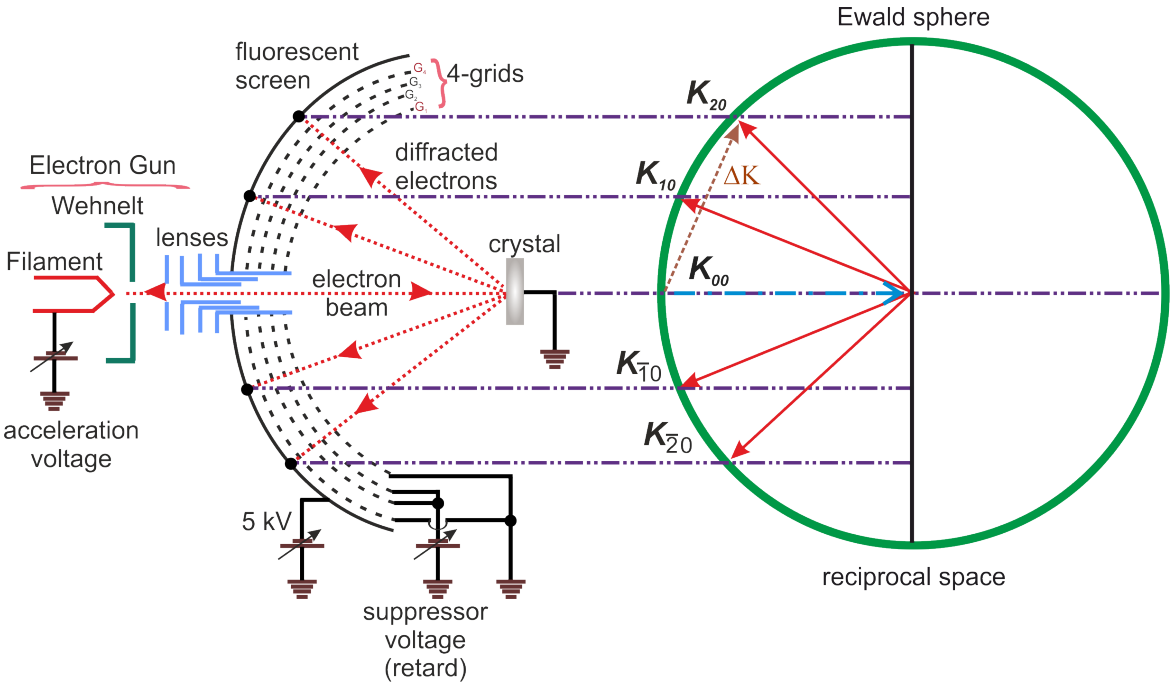

Figure 2.5: Schematic diagram of the LEED optics setup and the Ewald sphere construction.

It is noteworthy that the LEED pattern obtained is a representation of the reciprocal space; the distance between LEED spots is inversely proportional to the distance between points in the "real" surface lattice.

Figure 2.5 presents a Ewald's sphere which is used to describe the diffraction process in reciprocal space.[53, 54] An electron beam at normal incidence, i.e. along the (0,0) direction, is drawn as an incident wave vector k_0 and its length is defined as the radius of the Ewald sphere,

$$|k| = \frac{2\pi}{\lambda} \tag{2.3}$$

When the energy of the incident beam is increased, the diffracted spots move toward the center of the LEED pattern and hence the radius of the Ewald sphere increases. All diffraction points are intersected by the Ewald sphere, k' is the wave vector of any scattered beam (e.g. k_1, k_2,..), and $|k_0| = |k'|$ as both are radii of the Ewald sphere. The difference reciprocal lattice vector,

$\triangle k$, the change in momentum on scattering, can be given as,

$$\triangle k \ = \overrightarrow{k}' - \overrightarrow{k} = G\overrightarrow{_{hkl}} \tag{2.4}$$

where *hkl* are the Miller indexes. As the diffraction that occurs on the surface is 2D, because of the absence of a diffraction condition vertical to the surface, the equation 2.4 can be written as,

$$\triangle k \ = G\overrightarrow{_{hk}} \tag{2.5}$$

Thus the LEED spots can be identified using Miller indexes with (hk), e.g. (0.0), (0,1), .etc. Due to the inverse relationship between the reciprocal and real spaces, peaks observed at small diffraction angles (small $\triangle k$ values, $\triangle k = \frac{4}{\lambda}\pi \ sin\theta$) correspond to large atomic spacing d in real space. By assessing the LEED pattern (brightness and sharpness) one can deduce the symmetry and structure of the clean well-ordered surfaces.

2.1.3 Auger electron spectroscopy

Auger electron spectroscopy (AES) yields information about the chemical composition of the surface. Auger electrons are named after Pierre Auger.[55] For more detailed discussions on AES (hardware and instrument) see refs. [56–59].

AES is based on the detection of the Auger electrons emitted from the surface by electron bombardment of 2-5 keV. Figure 2.6 shows the Auger process. When the sample is irradiated with a beam of electrons (or photons) the atoms become ionized, and electrons are ejected from the K-shell, which creates a core hole (see fig.2.6 (a and b)). Two mechanisms might occur: (i) An energetically higher electron fills this core hole, producing energy which is liberated in the form of x-ray fluorescence (radiation). (ii) This hole is filled by an electron from a higher lying level, i.e., L_1, which initiates another hole. The energy difference is transferred to a third electron of the same atom (see fig.2.6 (c)). The Auger process involves three electron transitions, therefore Auger transitions can occur in all elements of the periodic table, except for H and He (because atoms have less than three electrons).

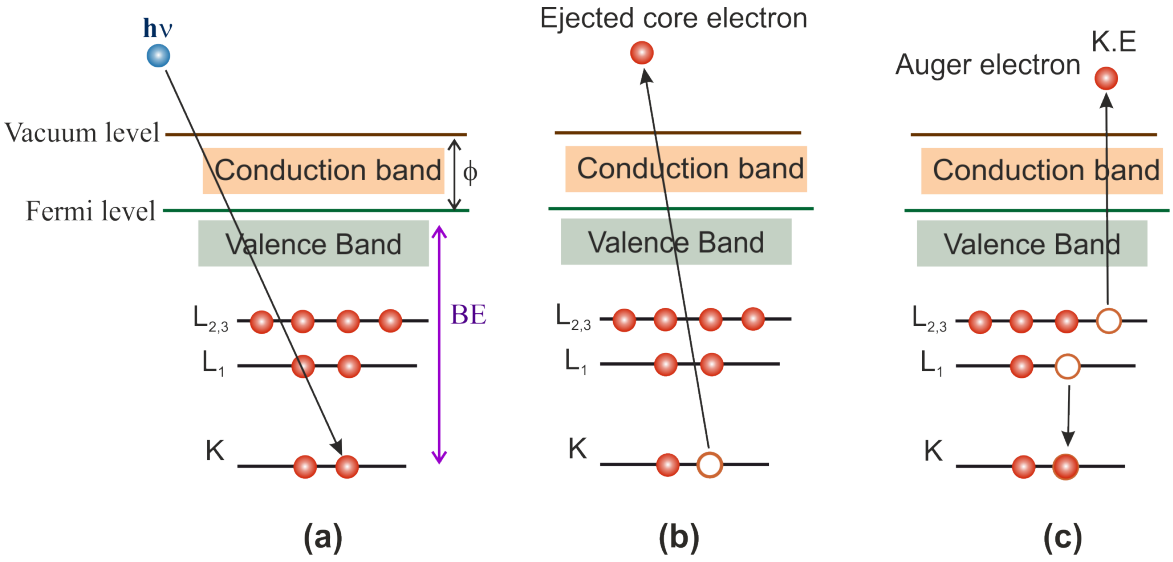

Figure 2.6: Schematic diagram of an Auger emission process in a solid.

Based on the location of the initial hole and the location of the final two holes, the Auger transition is characterized and the kinetic energy $E_{kL_1L_{2,3}}$ can be estimated as follows:

$$E_{kL_1L_{2,3}} = E_k - E_{L_1} - E_{L_{2,3}} - \Phi \tag{2.6}$$

where $E_k, E_{L_1}, E_{L_{2,3}}$ are the binding energies of the respective electronic levels, and ϕ is the work function of the material, $\phi = E_{vacuum} - E_{Fermi}$. The kinetic energy of an Auger electron is in the range of 50 to 1000 eV AES, which makes the technique surface sensitive (see fig.2.3). The energy of the emitted Auger electron is a well-defined characteristic allowing for the identification of chemical elements in the sample.

2.1.4 Infrared reflection absorption spectroscopy

Infrared spectroscopy is an informative technique which allows for the identification of the nature of surface phonon, adsorbate molecules, and interactions that occur between adsorbate-substrate or between adsorbate-adsorbate.[60–64] (Phonon refers to the lattice vibrations in the crystal).

The infrared light can be divided into three regions: near infrared (12.500 to 4000 cm^{-1}), mid infrared (4.500 to 400 cm^{-1}), and far infrared (400 to

12.5 cm^{-1}).

The infrared reflection-absorption spectroscopy (IRAS) is based on the interaction between electromagnetic radiation in the infrared region and the surface atoms. The infrared spectrum is measured by either absorbance mode or percent transmittance mode on the y-axis and wavenumber (cm^{-1}) to measure the position of an infrared absorption on the x-axis.

According to the "weight on a spring" model, atoms can be modeled as a mass hanging from a spring attached to a fixed ceiling.[65] The frequency of the vibrational modes for diatomic molecules can be calculated using the harmonic oscillator, which considers the atomic mass of both atoms as well as the strength of the bond. The absorption frequency can be calculated as follows:

$$\nu \;=\; \frac{1}{2\;\pi\;c}\sqrt{\frac{k\;(m_1\;+\;m_2)}{m_1\;m_2}} \tag{2.7}$$

where m_2, m_2 are the masses of vibrating atoms, c is the velocity of light (3×10^{10} cm/sec), k is the force constant (bond strength, dynes/cm), and ν is the wavenumber (cm^{-1}).

In general, not all molecular vibrations are IR active, only vibrations with nonzero net dipole moments are IR observable. If a molecule is adsorbed on a metal surface, the absorption of the IR light by this molecule will be affected by the dielectric behaviour of the metal surface. This is known as the "surface selection rule" (SSR),[66, 67] which is schematically displayed in fig.2.7.

In the case of a dipole parallel to the surface, the net dipole moment is equal to zero and the electric field does not interact (IR inactive). Therefore, the parallel dipole moment to the surface plane is not accessible. Only those vibrations which are perpendicular to the metal surface will be contribute to the IR absorption spectrum, i.e. for which

$$\left(\frac{\partial\overrightarrow{\mu}}{\partial\varrho_k}\right)_{\perp} \neq 0 \tag{2.8}$$

where ϱ_k is the normal vibrational coordinate, and $\overrightarrow{\mu}$ is the operator of the molecular electric dipole.[68]

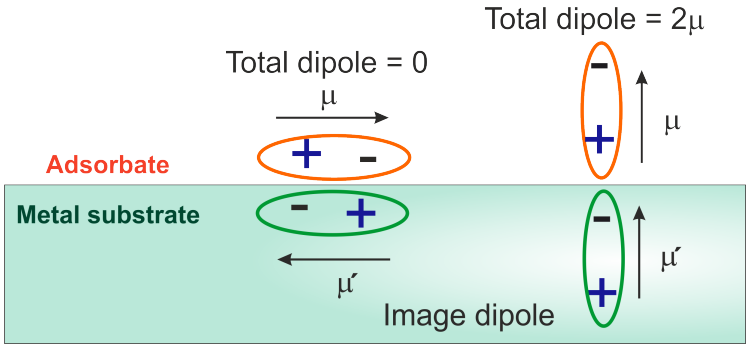

Figure 2.7: The metal surface selection rule.

Another important aspect is the polarization components (S- and R) of IR light and its phase shifts upon reflection.[69] It turns that the reflection experiment performed with p-polarized light at grazing incidence achieved the maximum surface electric field as well as the maximum absorption peak intensity.

To increase the signal-to-noise ratio of the absorption bands, IRAS is performed using Fourier-Transform instruments (FT-IRAS). The latter also provides a high resolution of spectra ($\sim$1 cm^{-1}) and faster scanning through the frequency range.

For an accurate assignment of the IR spectra, the absorption bands, frequency shifts, and the intensity of vibrations have to be carefully rationalized. For instance, mechanical renormalization or wall effect, [70, 71]polarization effect, chemical shift[72], and charge transfer [73] are commonly caused a frequency shift either to a higher wavenumber (blue-shift) or to a lower wavenumber (red-shift).

2.1.5 Temperature programmed desorption

Since temperature programmed desorption (TPD) is the main technique used in this study, it will be discussed in more detail. TPD is one of many techniques that are extensively used in surface science. The technique is derived from the so-called flash desorption (flash-filament) method, which was first illustrated by L.R. Apker.[74] In the flash desorption method, gas adsorption on a well-defined single crystal under high vacuum condition is examined. The activation energy of desorption and the order of reaction are determined

from the obtained results. The method was evaluated and the importance of the pumping speed was highlighted by Redhead.[75] In 1963, Amenomiya and Cvetanovic [76] modified the flash desorption method and first proposed the term TPD. Since then the experimental setup and the method have been upgraded and modified for different purposes, e.g. for the investigations of oxidation, reduction and sulfidation reactions. Therefore, the related techniques are referred to as temperature programmed oxidation (TPO), temperature programmed reduction (TPR) and temperature programmed sulfidation (TPS), respectively.

The TPD technique provides quantitative and qualitative information about surface interactions between adsorbed molecules and the substrate surface. Important kinetic parameters such as reaction order, the pre-exponential factor, and the activation energy can be determined by analysis of the TPD data.

TPD is applicable for the study of the adsorption process of gaseous on solid surfaces. The discrimination between different desorbed species within the same temperature region is perfectly achieved by the mass spectrometer. Figure 2.8 depicts the quadrupole mass spectrometer (QMS) instrument used in the TPD setup. In principle, QMS aims to separate ions according to their mass-to-charge (m/z) ratio.[77] QMS combines both a DC and radio frequency (RF) electric field applied to four parallel rods. The cathode produces electrons ($\sim$70 eV) to ionize gas atoms or molecules. A constant potential of both the DC component and an oscillating RF component ($V cos\ \omega t$) is applied to one pair of rods while the opposite voltage is applied to the other pair. The field is rapidly switching and sends most ions between the four rods. Ions with a certain m/z ratio follow a stable periodic trajectory of limited amplitude until they reach the ion detector. The latter includes a secondary electron multiplier or a Faraday cup.[78] In a typical TPD experiment, the sample is kept at a constant temperature T_0. Then the gaseous molecules under investigation are adsorbed with known dosages. After that the sample is heated with linear ramp $T_t = T_0 + \beta\ t$, where t is the time and β is the heating rate. Eventually, the dependence of the desorbed gas partial pressure (rate) on temperature changes is accomplished and referred to as the desorption spectrum. Figure 2.9 illustrates the obtained TPD spectrum when both temperature and coverage

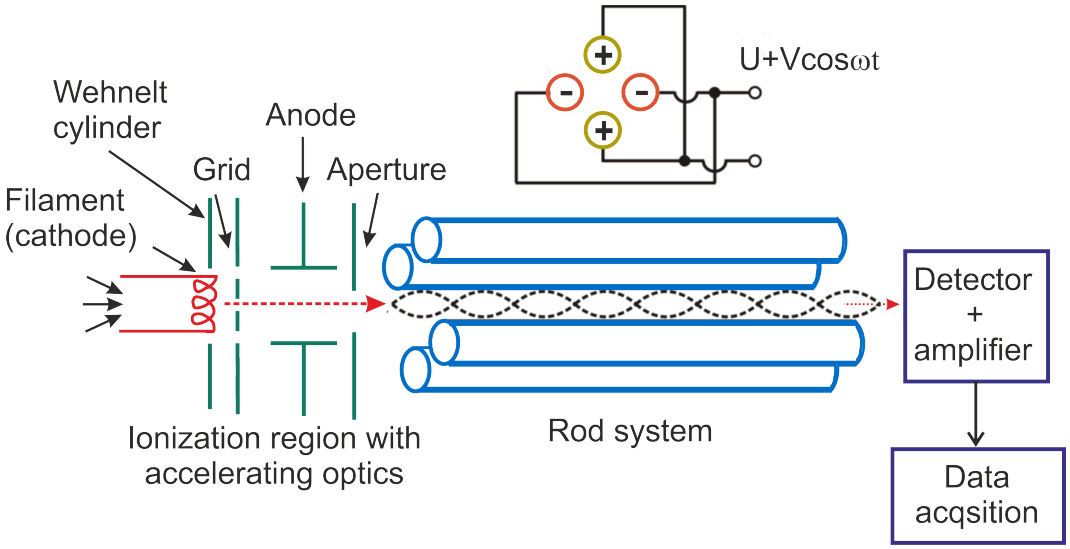

Figure 2.8: Sketch of the quadrupole mass spectrometer setup for TPD measurements.

change with the same desorption rate.

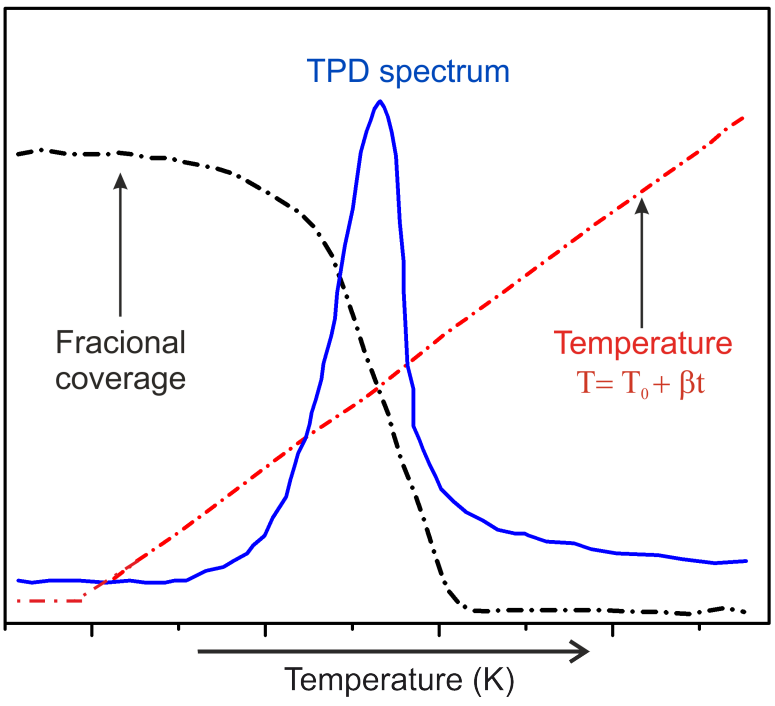

Figure 2.9: Desorption rate β, surface coverage Θ, and temperature dependence on time during temperature, taken from [79].

The desorption rate per unit area $(\mathrm{d}\theta/\mathrm{d}t)$ of the adsorbent is described

as follows;

$$\frac{d\theta}{dt} \;=\; \left(\frac{V}{A\ K_B\ T_g}\right)\left(\frac{dP}{dt} \;+\; \frac{SP}{V}\right) \tag{2.9}$$

where S is the pumping speed; V is the volume of the desorption chamber; A is the surface (adsorbent) area; T_g is the gas phase temperature; θ is the surface coverage (molecule cm^{-2}); and P is the pressure increase above the background. K_B is the Boltzmann constant (1.3806×10^{-23} J K^{-1}), alternatively $R = N_A \times K_B$, where N_A is Avogadro's number, 6.02214×10^{23}. Whenever the heating rate $dT/dt = \beta$ is low and the pumping speed to volume ratio (S/V) is large, then $dP/dt \ll (S/V)P$ is well proportional to the increase in the pressure P. In the TPD experiment, the readsorption is negligible because of fast pumping i.e., the pumping speed $\propto$ - $d\theta/dt$.[80]

Furthermore, the rate of desorption can also be written as follows for a linear heating ramp;

$$r_{des} \;= -\frac{d\theta}{dt} \;=\; k_n\ \theta^n \tag{2.10}$$

where n is the order of desorption. The desorption rate constant k_n can be described by the Arrhenius equation:

$$k_n \;=\; \nu\ exp\left(-\frac{E_{des}}{RT}\right) \tag{2.11}$$

in which r_{des} is the rate of desorption that is measured by mass spectrometer; E_a is the activation energy of desorption; and T is the temperature.[80] ν is the pre-exponential factor of desorption that describes the frequency (or lattice oscillations) of adsorbed species that vibrates towards desorption (commonly has an assumed value of about 10^{13} s^{-1}).

The equation that represents the desorption rate (r_{des}) as a function of coverage and temperature is generally known as the Polanyi-Wigner equation (Eq. 2.12):

$$r_{des} \;=\; -\;\frac{d\theta}{dt} \;=\; \nu_n\ \theta^n\ e^{-\ E_{des}\ /\ R\ T} \tag{2.12}$$

The Polanyi-Wigner equation (eq. 2.12) is used to analyze TPD data, and to determine the kinetic parameters of the adsorption process.

The overall shape of the TPD spectra for several initial coverages can provide information (n=0) about the adsorption kinetic. A zero-order desorption profile is typically observed for weak adsorped species, which is characterized by shearing the leading edge of a nonsaturated peak with sharp descending (see fig.2.10 (a)). In the case of first-order desorption (n=1), the spectra symmetrically appear around the peak maximum, fig.2.10 (b), with the independence of peak maximum temperature on the coverage. Figure2.10 (c) presents second-order desorption (n=2), in which the peak position shifts toward lower temperatures as coverage increases, as is commonly observed in many dissociative adsorption reactions.

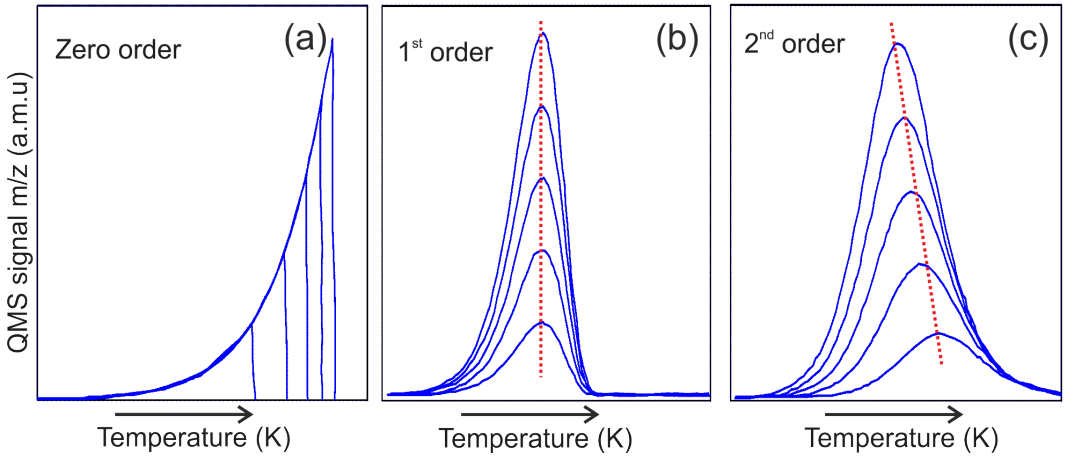

Figure 2.10: The kinetic orders of desorption process, (a) a zero order, (b) first order, and (c) second order desorption process.

Interpretation and evaluation of TPD spectra can provide significant information about adsorption kinetics. Numerous methods have been introduced to analyze TPD spectra. These methods have been critically reviewed in ref. [81–83] Here, we will demonstrate some of these different procedures that have been introduced for calculating desorption parameters from TPD spectra.

2.1.6 Methods of Analyzing TPD Data

Complete analysis

This analysis is also known as the Taylor-Weinberg-King method.[80] The indicated method allows the desorption energy E_{des} to be determined precisely

without any assumption about ν. The TPD spectra (see figure 2.11) are integrated to obtain the coverage as a function of temperature (coverage vs temperature). Then the coverage at a certain known value θ' is chosen (e.g., $\theta =$ 0.15 ML). The desorption rate (r_{des}) value that corresponds to θ' is determined on all spectra with initial coverage higher than θ', taking into account that the value of θ' is reached at different temperatures for each spectrum. Finally, an Arrhenius plot of the corresponding natural logarithm of the desorption rate $\ln(r_{des})$ versus the reciprocal of the temperature $1/T$ is constructed.

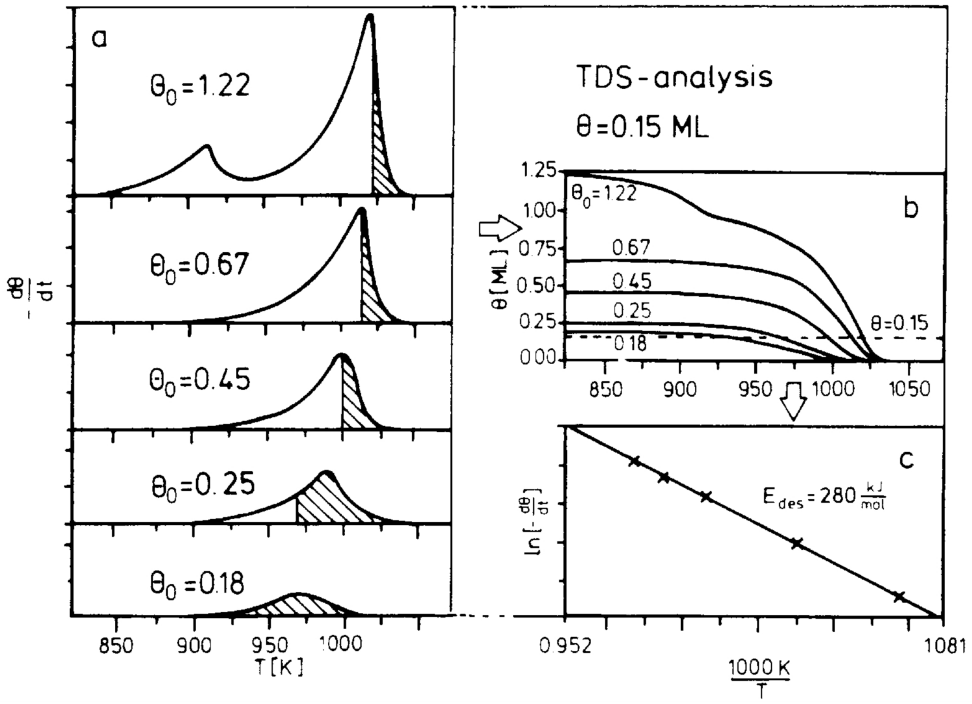

Figure 2.11: The different steps of Taylor-Weinberg-King method. The figure adapted from Ref. [84]

The slope of the plot presents $E(\theta')$. Meanwhile, the intercept of the Arrhenius plot yields (n ln θ'+ ln $\nu(\theta')$). If the desorption order n is known, and assuming that $\nu(\theta)$ is temperature independent, then $\nu(\theta')$ can be estimated. The term n ln θ' is much smaller than ln $\nu(\theta')$, for coverage above 0.1.

Inversion analysis of Polanyi-Wigner equation

This analysis relies on two assumptions in order to derive the functional dependence of E_{des} on coverage, namely: the desorption is a first-order process, and ν is coverage and temperature independent.[85] By integrating the desorption rate signal with respect to the temperature from T to the limit $T \rightarrow \infty$, i.e.,

$$\theta\ (T)\ =\ \frac{1}{\beta}\int_{T}^{\infty}\frac{d\theta}{dT\ '}\ dT\ ' \tag{2.13}$$

where $\lim_{T\rightarrow\infty}\ \theta\ \ (\mathrm{T})\ =0$ and $\beta = dT/dt$. If we take the Polanyi–Wigner equation (2.12) and apply mathematical inversion and rearranging, it yields Eq. 2.14.

$$E_{des}(\theta)\ =-\ R\ T\ ln\left[-\ \frac{d\theta\ /\ dt}{\nu\ \theta}\right] \tag{2.14}$$

where $E_{des}(\theta)$is the coverage-dependent desorption activation energy. As n=1, and ν (assumed value) are known, the energy curve ($E_{\ des}(\theta)$ versus θ) for each TPD spectrum can be obtained.

Notice that the general behavior (shape) of the obtained energy curve is the same for every value chosen for ν (e.g., E_{des} increases with increasing ν). Furthermore, the energy curve reveals E_{des} descending with increasing coverage, which can be explained by adsorbate–adsorbate interactions and/or different adsorption sites.

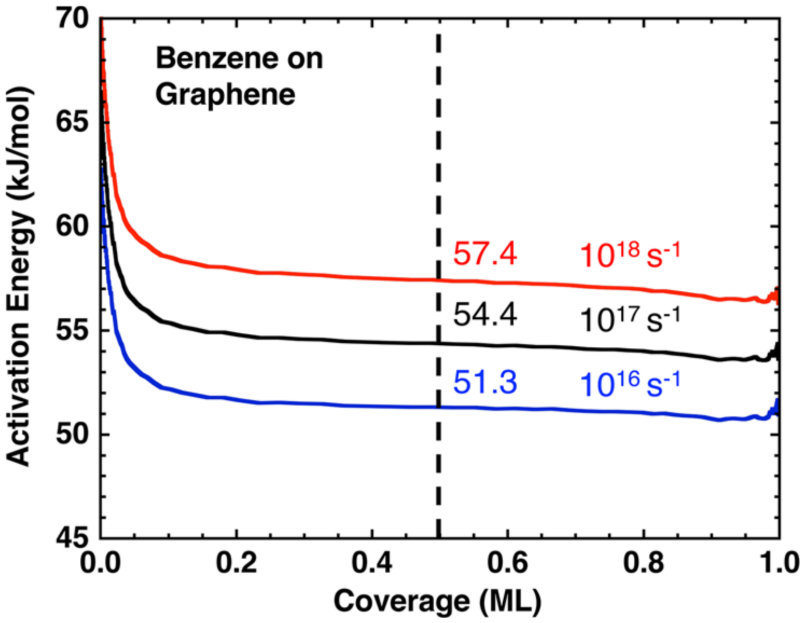

Figure 2.12: Coverage-dependent desorption energy curves for benzene on graphene covered Pt(111). The vertical dashed line is at a coverage of 0.5 ML, at which the desorption energies (kJ/mol) and the pre-factors are indicated. Adapted from [86]

Redhead's peak maximum method

This method is applicable for first order desorption that follows the Polanyi-Wigner equation. Both E_{des} and ν are coverage independent. Redhead [75] reformulated the Polanyi-Wigner equation to simply obtain the desorption energy E_{des} (independent of coverage) at desorption peak maximum. For 1^{st} order desorption ($n = 1$) and the sample temperature $T_t = T_0 + \beta\, t$, when T reaches maximum (T_m) then the derivative (- $d\theta^2$ / dT^2) = 0. By using the Polanyi-Wigner equation (Eq. 2.12), the relation between T_m, E_{des} and β can be represented as follows (for 1^{st} order desorption);

$$E_{des}/\ R\ T_m^2\ =\ (\nu/\beta)\ exp\ (-E_{des}\ /\ R\ T_m) \tag{2.15}$$

After taking natural logarithm and rearranging, we arrive at;

$$E_{des}\ =\ RT_m\ \left[ln\frac{\nu\ \ T_m}{\beta}\ -\ \ ln\frac{E_{des}}{R\ T_m}\right] \tag{2.16}$$

Knowing that E_{des} and T_m are linearly correlated for certain ν and β values, then $ln(E_{des}/R\,T_m)$ is estimated, and given in eq. 2.17.

$$E_{des} = RT_m \left[ln\frac{\nu\, T_m}{\beta} - 3.64 \right] \tag{2.17}$$

This estimation has an error below 1.5% for (ν / β) values between 10^8 to 10^{13} K $^{-1}$. Note that, for estimating E_{des} value, ν is usually assumed to be = 10^{13} s^{-1}. Additionally, Redhead proposed another equation (see eq. 2.18) that can be used to determine ν if E_{des} is already known (from another method).

$$\nu = (E\ \beta\ /\ R\ T_m^2\ \theta_0^{n-1})\ exp\ (E\ /\ R\ T_m), \quad for\ \ n > 0 \tag{2.18}$$

The Habenschaden-Küppers (HK) or leading edge analysis

Habenschaden and Küppers [87] have suggested a simple procedure for estimating E_{des} without any assumption about ν, which can be calculated later at low coverage. The low temperature side of TPD spectra is selected in order to keep both ν and T constant. Then these selected points are plotted as $ln\ r_{des}$ versus $1/T$, as stated in the logarithmic Polanyi-Wigner equation (eq.2.19):

$$ln(r_{des}) = -\frac{E_{des}}{RT} + ln\ \nu + n\ ln\ \theta \tag{2.19}$$

This results in the Arrhenius plot with a slope (- E_{des}/R), where R is the gas constant (8.314 $J.K^{-1}.mol^{-1}$). The intercept of the obtained straight line is represented in the term ($n\ ln\ \theta + ln\ \nu(\theta,T)$), from which ν can be determined with high accuracy, as long as the coverage is low ($\theta \longrightarrow 0$). For the reliability of this method, a high signal to noise ratio is required at the leading edge.

Heating rate variation method (HRV)

In this method TPD spectra of the same coverage are collected at different heating rates β, assuming that at all heating rates the fractional coverage left on the surface is the same, once the peak reaches the maximum. Furthermore, both ν and E_{des} are coverage independent and heating rate dependent. Lord

and Kittelberger [88] had discussed this method in detail applying Eq. 2.21.

$$ln\left(\frac{T_m^2}{\beta}\right) = \frac{E_{des}}{RT_m} + ln\left(\frac{E_{des}}{\nu R}\right) \tag{2.20}$$

$$ln\left(\frac{T_m^2}{\beta}\right) = \frac{E_{des}}{R}\left(\frac{1}{T_m}\right) + ln\left(\frac{E_{des}}{\nu R}\right) \tag{2.21}$$

Plotting $\ln({T^2}_m/\beta)$ versus $1/T_m$ as a function of the heating rate β results in a straight line that yields E_{des} from the slope, and the frequency factor ν from the intercept.

In the case of 2^{nd} order desorption, E_{des} and ν can be determined by plotting $\ln({T^2}_m\ {\theta^{n-1}}_m\ /\ \beta)$versus $1/T_m$, if the coverage is known. Keeping the same surface coverage in each experiment (for every heating rate) is essential, otherwise the obtained plot will be scattered. Also, the heating rate β should be changed by at least one order of magnitude for reliability with this method.[75]

According to Jong and Niemantsverdriet,[82] evaluation of the previous analysis procedures, the complete analysis described by King [80], or the leading edge analysis [87], provide a meaningful data for E_{des} and pre-exponential factor. However, the kinetic order of desorption has to be determined beforehand.

Recently, these authors have followed up their work in ref. [83] and have highlighted the rule of the "compensation effect" phenomenon on the evaluation of kinetic parameters obtained from TPD data. At a higher coverage, the kinetic parameters of the desorption processes become dependent on coverage, due to lateral interactions. Consequently a new term called "compensation effect" has to be considered. Otherwise, false estimated values of both the activation energy and the pre-exponential factor might happen.

Chapter 3

CO adsorption as a probe for surface terminations of Fe_3O_4 (111) and (001) films

This chapter presents the preparation procedure for Fe_3O_4(111) and Fe_3O_4(001) films, which were grown on Pt(111) and (001), respectively. We investigated the adsorption of CO, as a probe molecule, on both (111) and (001) facets, to determine the surface termination. The results of this part are published in reference [89].

3.1 Preparation of Fe_3O_4(111) films on Pt(111)

Pt(111) was chosen as the substrate for the growth of Fe_3O_4(111) films. After each step of the preparation procedure, the chemical composition and morphology of the surface were explored by LEED and AES, respectively, as illustrated in fig. 3.1(a-d).

The clean Pt(111) surface was achieved by repeated cycles of argon ion sputtering and annealing to 1100 K, followed by oxidation (P_{O_2}=10^{-6} Torr at 900 K), in order to burn off the carbon impurities that segregated from the bulk during the annealing step. Finally, the surface was flashed to 1100 K in UHV. The LEED shows a clear hexagonal (1×1) pattern (fig. 3.1(a)). The

absence of any contamination signals in AES spectra is considered to be good evidence that the Pt(111) surface is clean (fig.3.1(d)). Besides that, CO TPD was always performed before growing the film (fig. 3.2).

Fe_3O_4(111) films were prepared by following the recipe presented in Ref. [3, 27]. However we put a lot of effort into adjusting the preparation parameters (e.g. oxidation temperatures, oxygen partial pressures, and annealing temperature) to obtain a well ordered film surface showing a single termination.

Hence the Fe_3O_4(111) film was produced as follows: (i) Fe was deposited on Pt(111) at RT, and then oxidized with 10^{-6} Torr oxygen at 1000 K for 2 min to form 1 ML FeO layer. The latter exhibits a Moire LEED pattern due to the lattice mismatch, as in fig.3.1(b). The AES spectrum shows Fe and oxygen signals. (ii) The Fe_3O_4(111) film was finally obtained by repeating 2-3 cycles. Each cycle consists of 8-10 ML Fe deposited at RT in UHV and then oxidized in 5 $\times 10^{-7}$ Torr oxygen at 940 K. (iii) The sample was then annealed at 900 K for 5 min in UHV.

A Fe_3O_4(111) film exhibited a sharp hexagonal LEED pattern of well ordered surface (fig. 3.1(c)). As the film thickened the signal of Pt substrate attenuated until it completely disappeared (fig. 3.1(d)). According to the amount of deposited iron and previous cross-sectional TEM studies, the films are > 5 nm in thickness.

Since CO adsorbs at room temperature on Pt(111) substrate and not on iron oxide, CO uptake curves reflect the surface coverage. Therefore, the Fe evaporator was calibrated by CO titration of the Pt(111) surface (via TPD) after the growth of various FeO films that were formed by different Fe deposition times (with the same flux). Based on TPD spectra of CO, the surface was assumed to be covered with a monolayer equivalent once the CO uptake signal had completely disappeared. The results of these measurements and the coverage profile (obtained by integration the CO peak) are illustrated in fig. 3.2.

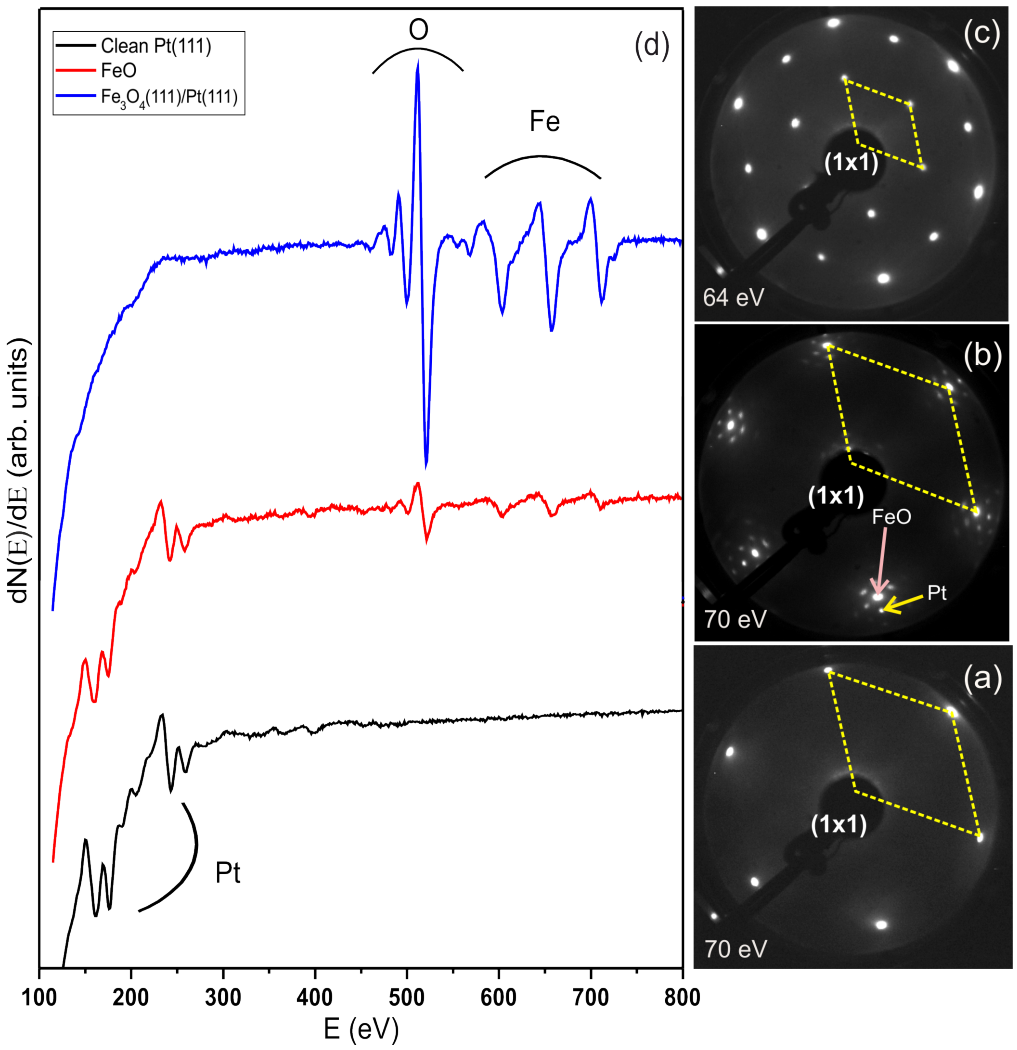

Figure 3.1: LEED pattern taken for (a) the Clean Pt(111), (b) FeO and (c) Fe_3O_4(111), at the indicated energies. The (1×1) unit cell is also indicated. The AES spectra of these surfaces are displayed in (d). All spectra were recorded at 3 kV primary beam energy.

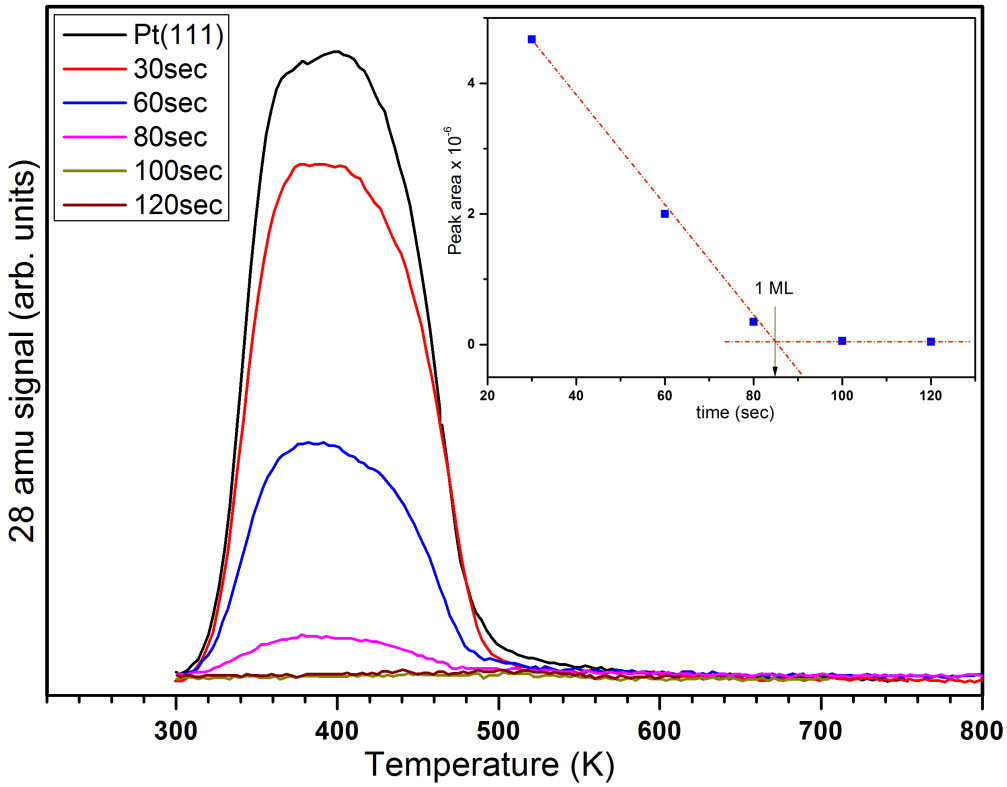

Figure 3.2: TPD data obtained upon adsorption of 1 L CO at RT on clean Pt(111) and on FeO films grown with different iron deposition times as indicated. The inset exhibited the TPD peak area as a function of iron evaporation time. The arrow points to 1 ML equivalent. The heating rate is 3 K/s.

3.2 CO adsorption

Several studies are reported on the interaction of carbon monoxide on the surfaces of metal and metal oxides, since CO appears either as product or reactant in reactions such as Fischer–Tropsch synthesis [20], the water-gas shift (WGS) reaction [19], the reverse water gas shift (RWGS)[90] etc..

CO is a simple molecule with high dissociation energy which is often used as a probe molecule. Since oxides are ionic compounds exposing acidic and basic sites, their interaction with CO can be used to evaluate the acidic/basic properties of the surfaces. For instance, CO interacts poorly with weak acidic sites on surfaces (e.g., TiO_2 rutile (110) [91, 92]), while surfaces with strong acidic sites form a stronger bond with CO (e.g., Co_3O_4(111) [93] and (001)

[94]).

The adsorption of CO on magnetite film surfaces has been studied by Udovic et.al.,[95] using TPD. The authors concluded that CO is weakly adsorbed on the magnetic surface through formation of carbonyl species, with a desorption heat of 46 kJ/mol. However, this finding was contradictory to the results from thin Fe_3O_4 film on Fe metal.[96] The latter surface displayed stronger interaction with CO.

Lemire et al.,[32] utilized various experimental techniques such as IRAS, HR-EELS and TPD to examine CO adsorption on $Fe_3O_4(111)$ film. The surface exhibited three desorption states at 110, 180, and 230 K. Based on TPD and IRAS results, the surface was suggested to be octahedrally (Fe_{oct2}) terminated.

The density functional theory calculations for CO adsorption with different coverage on both terminations Fe_{tet1}-and $Fe_{oct2-tet1}$ of $Fe_3O_4(111)$ were examined by Huang et al.,[35]. It was concluded that surface termination with $Fe_{oct2-tet1}$ is more favored, with adsorption energy in the range -1.94 to -0.83 eV, while adsorption of CO on Fe_{tet1} is less stable. In the case of (001) surface, DFT + U method indicated that CO is strongly bound to the defective B-layer of $Fe_3O_4(001)$ surface than the defectless surface.[97]

Due to the discrepancy in the literature about the surface termination (Fe_{tet1} or Fe_{oct2}), the termination of our film has to be verified. Therefore, CO was used as a probe molecule, where TPD, IRAS and DFT calculations were combined to estimate the most stable surface termination of $Fe_3O_4(111)$. The CO-TPD results are presented in more detail below.

$Fe_3O_4(111)$ was kept at 90 K then exposed to 1 L CO. The TPD curve reveals that CO desorbs in three peaks at 105, 170 and 230 K denoted as α, β and γ (as in ref.[32]), respectively. In order to achieve better resolution of β and γ peaks, the experiment was repeated at a higher adsorption temperature of 140 K. The CO-TPD profiles at 90 K and 140 K are illustrated in fig. 3.3.

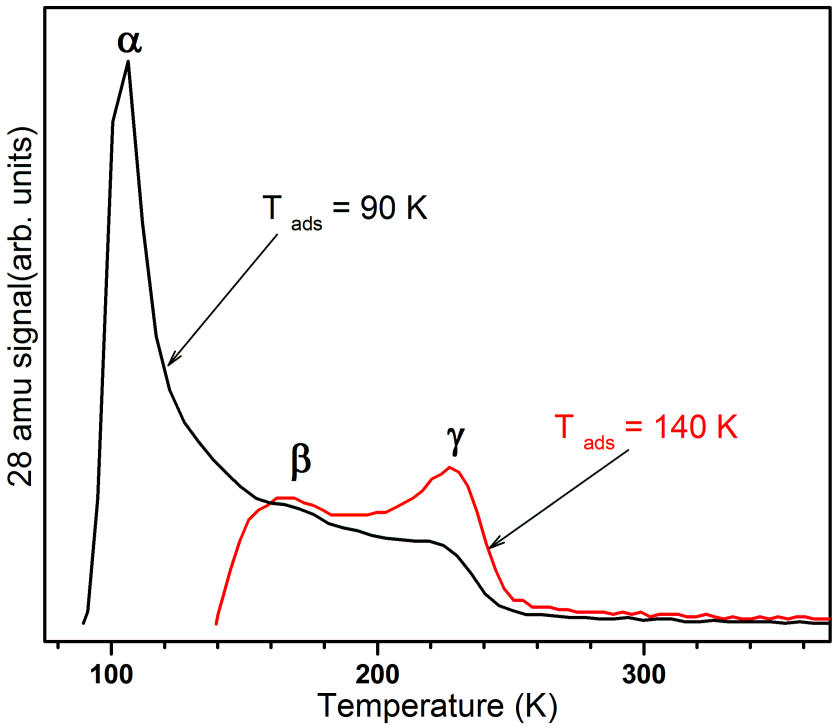

Figure 3.3: TPD spectra of 1 L CO adsorbed at 90 and 140 K on Fe_3O_4(111) film. The surface was heated to 600 K (spectra are cut off at 400 K) with a heating rate of 3 K/s.

The TPD data for CO on the clean Pt(111) substrate was suitable as a reference to quantify CO coverage on Fe_3O_4(111) film, especially since all measurements were performed in the same setup. Figure 3.4 shows a comparison between TPD spectra obtained from clean Pt(111) and Fe_3O_4(111) upon the adsorption of 1 L CO at 140 K. The CO coverage was estimated from the integrated area of the thermal desorption peak. Ertl et al.[98] reported two different LEED patterns $(\sqrt{3} \times \sqrt{3})$R30° and c(4×2) of CO on clean Pt(111) at a coverage of about θ= 1/3 and θ= 0.5, respectively. Clearly the CO superstructure is dependent on the adsorption temperature and coverage. Therefore, the LEED pattern was recorded after the adsorption of 1 L CO at 140 K (see the inset in fig. 3.4). The obtained LEED pattern displays c(4×2) and the same pattern has been reported by Steininger et al.[99] for CO coverage of about $0.5 < \theta < 0.58$. Knowing that, the c(4×2)-CO structure at 0.5 ML coverage corresponds to a CO density of 7.4×10^{14} cm^{-2}. Bearing this in mind, the lattice constant of Pt(111) and Fe_3O_4(111) are 2.77 Å and 6 Å,

respectively, and the β and γ states in TPD spectra are equivalent to 8×10^{13} cm^{-2} CO coverage, i.e 0.25 ML. 1 ML is referred to 3.2×10^{14} atoms cm^{-2}, i.e., one atom per Fe_3O_4(111) unit cell. Apparently, this coverage value is small to be assigned to the regular surface sites and hence it is attributed to defect sites.

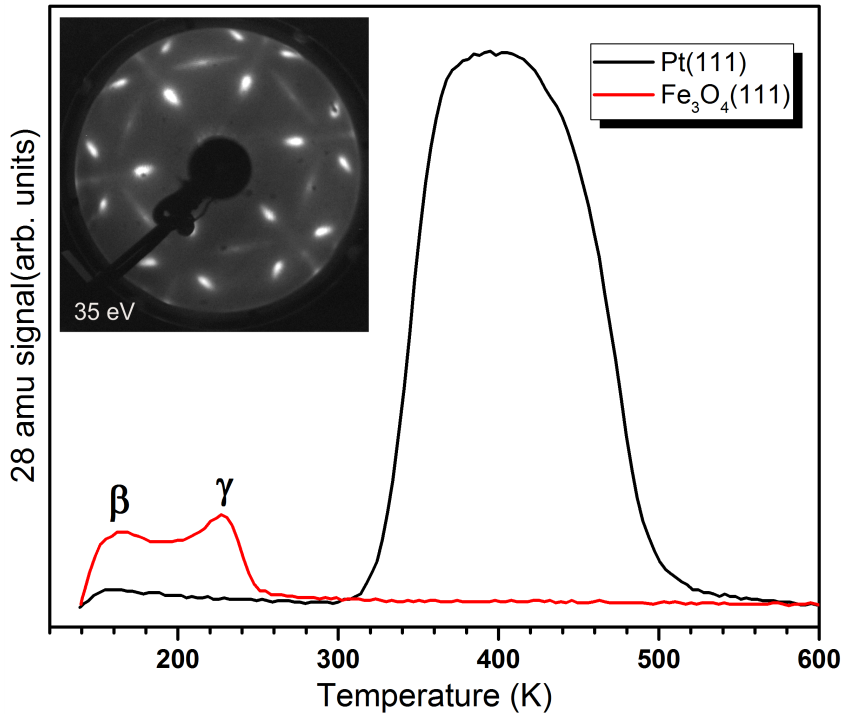

Figure 3.4: TPD spectra of 1 L CO adsorbed on clean Pt(111) (black spectrum) and Fe_3O_4(111) (red spectrum) at 140 K and heated by 3 K/s. The LEED pattern reordered after CO adsorption on clean Pt(111) is presented in the inset and shows the c(4×2)-CO structure.

To address the apparently low intensity of the β and γ peaks peak (in fig.3.3) as compared to those reported in Ref.[32], the residual water in the UHV background was also monitored during the CO TPD experiments.

Figure 3.5 (a) demonstrates the TPD profile for both CO and water after dosing 1 L CO at 140 K. As shown in both repeated experiments, the lower participation of residual water shows the higher intensity of the γ peak and vice versa.

Thus it may be inferred that water adsorption may take place on the surface while the sample is cooled to 140 K. Therefore, the film was cooled

down to 140 K in a CO atmosphere (backfilling the whole chamber) after flashing to 700 K. The TPD profiles obtained for CO and H_2O are shown in fig. 3.5 (b). It can be seen that the water adsorption still occurs, despite the presence of high CO content, and this adsorption prohibits CO adsorption in the γ peak. Despite the water contribution is lower than that in fig.3.5 (a).

An apparent trend can be observed in that the water and CO (γ peak) signals are inversely related. Thus water adsorption on the surface blocks CO adsorption in γ peak. The latter observation may be the reason for the attenuation in γ peak for CO adsorbed at 90 and 140 K (see fig. 3.3). Clearly, even under UHV, adventitious adsorption of water is difficult to avoid. Hence, the Fe_3O_4(111) films were always flashed to 900 K in UHV prior to any adsorption experiment. Furthermore, it is, therefore, logical that the next step has to be about the water interaction with magnetite surfaces before investigating CO_2 adsorption.

Here this raises the question about the possibility of CO_2 formation, so the signal of the mass 44 amu was always monitored. We did not detect CO_2 production, by the reaction with CO, in the TPD spectra.

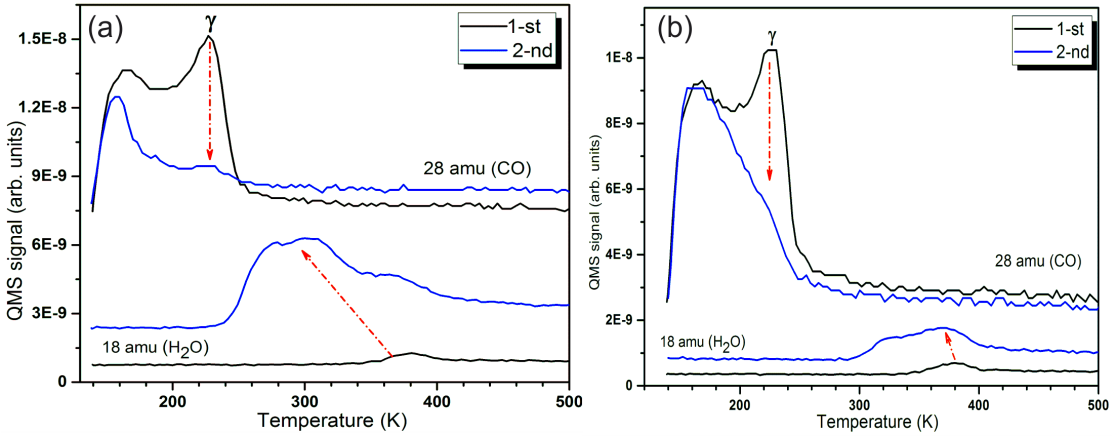

Figure 3.5: TPD spectra of CO (28 amu) and H_2O (18 amu). Signals were obtained during the heating of the Fe_3O_4(111) film to 700 K (spectra cut at 500 K) by 3 K/s. (a) The data obtained after exposure to 1 L CO at 140 K. (b) The spectra recorded after cooling the film from 700 K to 140 K in CO atmosphere. The spectra in (a) and (b) are not offset in order to observe the different levels of water in the residual gases.

Furthermore, IRAS and DFT calculations were compiled to rationalize

the results from CO adsorption on Fe_3O_4(111); more details can be found in Ref.[89] Now let us highlight the main points that bridged the experimental and theoretical results. DFT inspected CO adsorption on four model structures (each exposes a different termination) and are labeled as: - Structure (1) is Fe_{tet1} terminated surface. - Structure (2) is octahedrally terminated surface (Fe_{oct}). - Structure (3) and (4) are defect sites (step edges) of type A (Fe_{oct2}) and type B (Fe_{oct1} or "Fe-rich")[32, 100], respectively, each type being modified by an additional O-layer. Figure 3.6 shows the calculated vibrational frequencies of CO stretching mode and adsorption energy (at 1 ML CO coverage) of these structures gathered with the experimentally observed ν CO bands for comparison.

The calculated ν(CO) frequency (fig. 3.6, red column) of structure 2 is red shifted with respect to free CO (fig. 3.6, black column). Moreover, the adsorption energy of -102.6 kJ/mol, CO bound to Fe_{oct}, is the highest for all four structures. Applying Redhead analysis with a pre-factor of 10^{13} s^{-1} results in CO desorption peak $\sim$ 400 K , which have never been experimentally observed (see TPD spectra in fig.3.5 and fig.3.3). Based on this comparison, the octahedral termination can be safely excluded.

In the case of structure 3 (defect sites of type A), the calculated frequency is very close to the observed γ peak and exhibits blue shift concerning the stretching frequency of CO gas (2204 cm^{-1}). This blue shift can be explained by the "wall effect "[101] due to the repulsion between surface O^{2-} ions and the lone electron pair of the C atom.

The predicted CO stretching frequencies of both structures 1 and 4 fall within the range of experimental observation. As earlier observed, the β peak is relatively low pronounced and sensitive to the adsorption temperature (see fig.3.3), therefore, it is rational to assign β state to adsorption on the defect sites of type B (Fe-exposing step edge). On the other hand, α state dominated the spectra at low temperature and was thus attributed to regular sites, Fe_tet1.

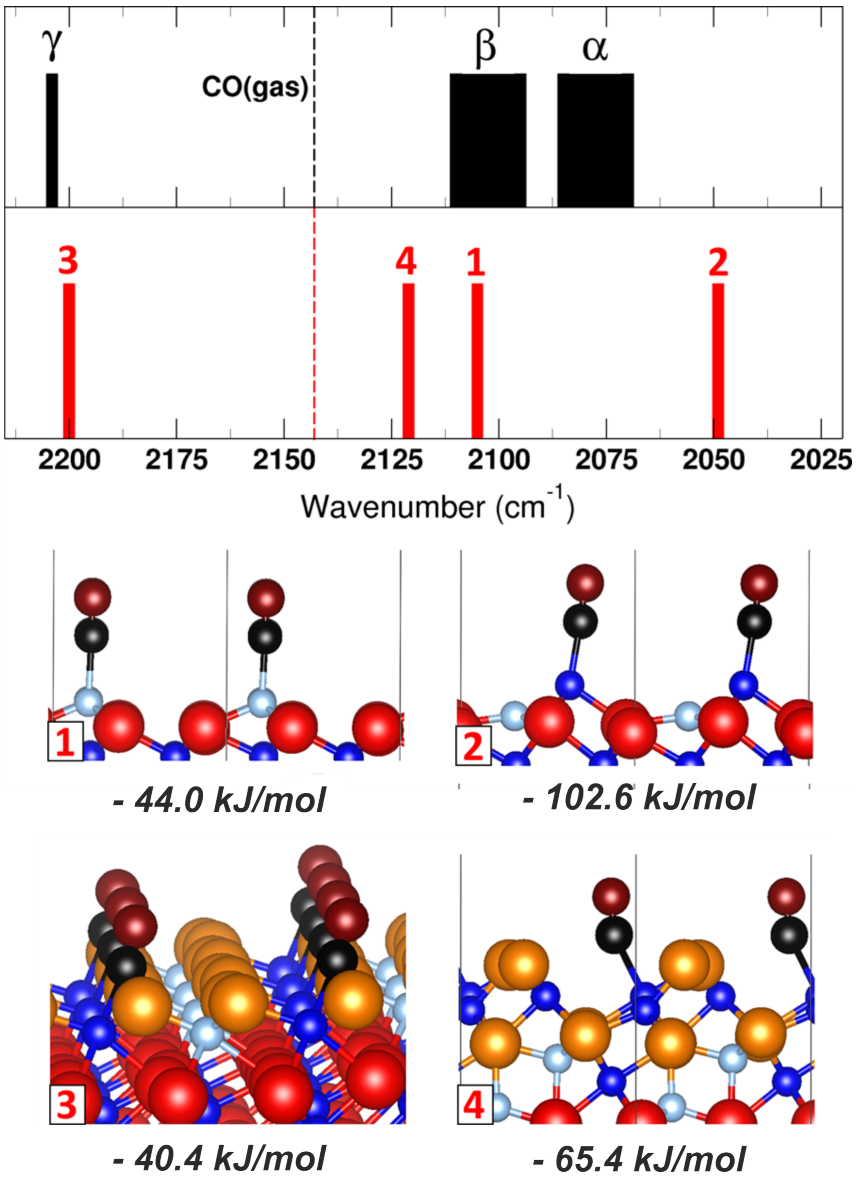

Figure 3.6: The upper panels and present the experimentally observed (black columns) and calculated (red columns) ν (CO) bands corresponding to the structures (1-4) displayed below. The calculated adsorption energies of 1 ML CO coverage (i.e., 1 CO molecule per (1×1) unit cell) are given in kJ/mol. Dark blue, light blue and red colors are referred to Fe_{oct}, Fe_{tet1} and lattice oxygen, respectively. The oxygen-adlayers in structure 3 and 4 are in orange. CO molecule is colored in dark red (O) and black (C). Adapted from [89].

Consequently, the DFT calculation and experimental results are consistent with the assumption that the $Fe_3O_4(111)$ surface is a single terminated, exposing 1/4 monolayer of tetrahedrally coordinated Fe^{3+}. However, the na-

ture of the defects responsible for high-temperature CO desorption remains unclear and and subject to speculation.

3.3 Preparation of Fe_3O_4(001) films on Pt(001)

The clean Pt(001) surface was achieved using standard cleaning procedures, i.e. sputtering and annealing in UHV and oxygen. Thereafter the surface quality was evaluated by LEED and AES as shown in fig.3.7. It can be seen that no additional signals other than Pt are observed in the AES spectra, and the hex-reconstructed Pt(001) surface is very clear in LEED (fig. 3.7(a)). CO TPD was investigated and the clean Pt(001) exhibited the well known profile of a sharp desorption peak at ∼520 K with a shoulder at 440 K.

Following the recipe developed in our department in Ref. [44], that was developed in our department, after optimizing the preparation parameters, well ordered reconstructed Fe_3O_4(001)-($\sqrt{2} \times \sqrt{2}$)R45° was formed, as is evident in the LEED pattern (see fig. 3.7(b)). The preparation consists of three main steps. In the first step, the metallic iron is evaporated on the clean Pt(001) at RT in UHV forming a buffer layer of ∼15 ML (according to Fe calibration on Pt(111)). Reactive deposition of iron is the second step, where 25 ML Fe was deposited at RT and in an oxygen atmosphere (i.e.,7×10^{-6} Torr). Subsequently the surface was annealed at 960 K for 20 min in oxygen 7×10^{-6} Torr. The corresponding LEED pattern clearly reveals ($\sqrt{2} \times \sqrt{2}$)R45° reconstruction with respect to the (100)-unreconstructed Fe_3O_4 surface unit cell (see fig. 3.7(b)). Due to the absence of a Pt signal in the AES spectra, and based on the amount of deposited Fe and the previous cross-sectional TEM studies, the thickness of the films is more than 5 nm.

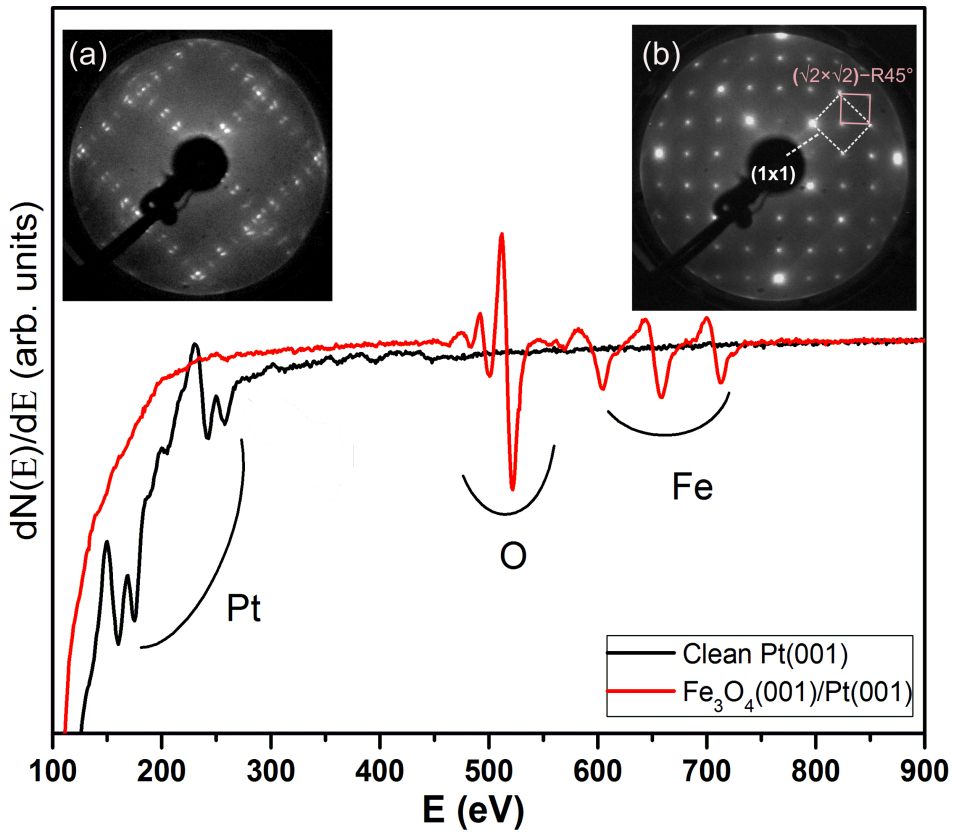

Figure 3.7: The LEED pattern of (a) clean Pt(001)-hex and (b) Fe_3O_4(001)-($\sqrt{2}$ × $\sqrt{2}$)R45° are shown with an electron energy of 95 eV. The bulk truncated and reconstructed unit cells display in white and pink squares, respectively. AES spectra are taken for both surfaces.

Figure 3.8 illustrates the difference in the CO profile on Fe_3O_4(001) and (111) films. The α state appearsin both surfaces and is regarded as a "tail" of the desorption peak at lower temperature. The latter observation is in agreement with the TPD results on a single crystal Fe_3O_4(001), revealing a weak interaction via adsorption on regular sites.[102] Contrary to (111), Fe_3O_4(001)-($\sqrt{2}$ × $\sqrt{2}$)R45° lacks β and γ peaks. This implies either that the (001) facet has fewer defects [5, 44] or, more probably, that the defects that do exist are inert to CO.

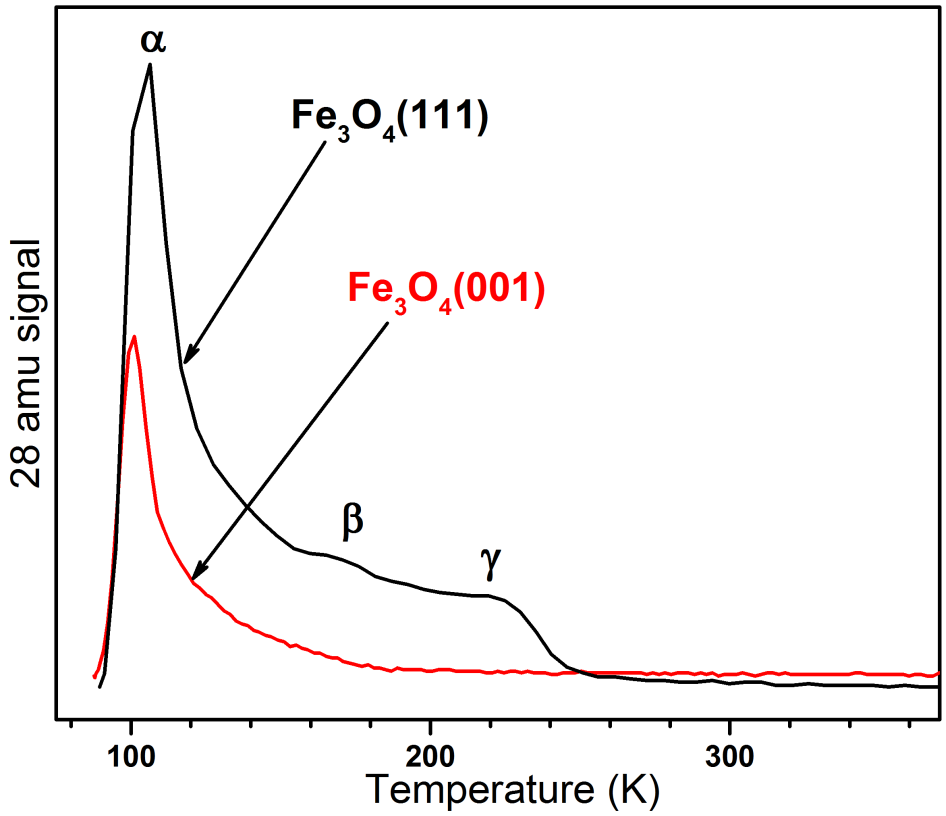

Figure 3.8: CO TPD data after adsorption of 1 L CO on Fe_3O_4(111) and (001) films at 90 K. The heating rate was 3 K/s.

Concerning the β and γ desorption states on Fe_3O_4(111), which are assigned to surface defects, these are found to be crucially dependent on the film preparation and vacuum conditions. Thus the prediction or control of the surface quality is difficult and should be precisely evaluated prior to any study. Additionally, since the interference from UHV residual gases may lead to misinterpretations, these gases should be carefully monitored.

3.4 Summary

The Fe_3O_4(111) surface is tetrahedrally terminated Fe^{3+}_{tet1}, while defect sites which are manifested themselves by β and γ desorption states may expose other terminations. The adsorption of CO on both Fe_3O_4(111) and Fe_3O_4(001)-$(\sqrt{2} \times \sqrt{2})$R45° surfaces is relatively weak, showing a main desorption peak at temperatures lower than 100 K. However, CO may be strongly bound to

the defect sites, although the exact nature and extent of these defects on the magnetite (111) and (100) surfaces are not known. The Fe_3O_4 (111) surface is very sensitive to traces of water in the UHV background. The latter affects CO adsorption in the γ state, and it seems that both CO and water compete for the same adsorption sites.

Chapter 4

Water adsorption on Fe_3O_4

4.1 Introduction

Water is ubiquitous and abundant in the environment; it covers 70 percent of the Earth's surface. The heat of the sun and the pull of gravity result in the continuous exchange of water between the earth and the atmosphere. From the physical perspective, "water properties" are unique compared to other liquids. Water appears as a reactant, a product, a solvent and a reaction medium that is associated with all life on earth and for most activities of human society. On a wider level, one can find the pervasive role of water in the world of science, which includes meteorology, geology, heterogeneous catalysts, electrochemistry, solar energy, corrosion chemistry, and physical chemistry. These scientific disciplines of water-related sciences demand a comprehensive detailed understanding of water interactions, especially at the atomic-scale.

In many interfacial systems water appears as an important adsorbate, making the interaction of water with surfaces, particularly metal oxides, a topic of interest. Water/iron oxide interfaces play key roles in many important heterogeneous catalytic processes, such as in photocatalytic splitting of water [103], the Fischer–Tropsch synthesis of hydrocarbons [20](i.e. $nCO + (2n+1)H_2 \longrightarrow C_n\ H_{2n+2} + nH_2O$), the dehydrogenation of ethylbenzene to styrene [104] and WGS reaction [19]. Magnetite has a significant importance in these processes. Therefore, the WGS reaction in particular exemplifies the significant importance of magnetite.

WGS reaction, i.e. $CO + H_2O \leftrightharpoons CO_2 + H_2$, is an industrial process

that is used in hydrogen production for fuel cell applications. WGS utilizes different catalysts depending on the temperature range. The high temperature step (320-450 °C) utilizing the Fe_3O_4-Cr_2O_3 catalyst, while the low temperature step (200-250 °C) uses Cu/ZnO/Al_2O_3 catalysts.[105] Magnetite provides a surface for adsorption and interaction of the WGS reactant species to form product species followed by desorption. Moreover, it acts as an oxygen transfer medium and is alternately oxidized and reduced via a "regenerative" mechanism.[19] Water dissociation has been reported as one of the rate-limiting steps of WGS reaction. Indeed getting more insights about water/Fe_3O_4 interface will help in increasing H_2 production efficiency.

Despite intensive studies, many questions concerning interface water structure are still elusive: Does water adsorb dissociatively or intact? What is the energy difference? Which adsorption sites are involved? In the following section, we will address these questions. Furthermore, we will demonstrate the important role of the metal oxide surface structure in the water/magnetite interaction.

As far as water adsorption on magnetite Fe_3O_4 is concerned, different studies are highlighted here.

A comparative study between FeO(111) and Fe_3O_4(111) films upon water adsorption demonstrated that FeO(111) is chemically inert while the dissociation occurred only on Fe_3O_4(111).[106, 107] The latter surface exposed 1/4 Fe (Fe_{tet1}) atoms over a close-packed oxygen layer underneath which act as a Lewis acid and Broensted bases, respectively.

Leist et al.[108] combined IRAS and TPD spectroscopy in order to investigate water adsorption on epitaxially grown FeO(111), Fe_3O_4(111) and Fe_2O_3 (biphase) films in the range 110–320 K. The authors found that at low coverage water adsorbed dissociatively on Fe_3O_4(111), followed by dimers formation with increasing coverage. The authors suggested that these dimers could act as nucleation centers for 3D-ice formation. Meanwhile, IR spectra displayed two adsorption bands at 2712 and 2691 cm^{-1} that were assigned to O_sD and O_wD-Fe_{tet1} species. O_sD and O_wD are hydroxyl groups interacting via oxygen atoms from Fe_3O_4(111) lattice (O_s) and oxygen atoms from water molecule (O_w), respectively. Contradicting these findings, a recent study [109] assumed that Fe_3O_4(111) is Fe_{oct2} terminated surface. The authors also suggested the

formation of a "half-dissociated" complex as a result of binding of two OH groups (resulting from dissociated water molecules) with non-dissociated water molecules.

Adib et al.,[110] applied TPD to investigate D_2O on $Fe_3O_4(111)$ single crystal. They observed that TPD spectra showed complex desorption features in the range of 300–770 K. This observation has been rationalized on the basis of multiple adsorption sites e.g., different terminations and defects.

Another study was carried out by Kendelewicz et. al [111] on $Fe_3O_4(111)$ and (001) single crystals using O 1s and Fe 2p photoemission spectra and Fe L-edge and O K-edge near-edge extended X-ray absorption fine structure (NEXAFS) spectra before and after water adsorption at 298 K. The study revealed that water similarly adsorbed independent of crystallographic orientation. New electronic states appeared depending on water partial pressure. Additionally, the study pointed to the critical issue of controlling the surface structures and stoichiometry of iron oxide samples.

However, the study done by Cutting et. al. [33] on $Fe_3O_4(111)$ single crystal using scanning tunnelling microscopy (STM) and with X-ray photoemission (XPS) and UV-photoemission (UPS), demonstrated that water dissociated at 200 K and at lower water partial pressure than that reported by Kendelewicz et. al.[111]. This discrepancy was explained by the intermolecular mechanism of water molecules that plays a critical role in promoting water dissociation on the Fe_3O_4 (111) surface. At the same time, STM images suggested that hydroxyl groups are sitting atop Fe^{3+} (Fe_{tet1}) ions. Similar findings have been reported applying STM and DFT calculations on $Fe_3O_4(111)$ single crystal surface, prepared by a reduced surface of hematite single crystal α-$Fe_2O_3(0001)$.[112]

Further insights into this framework have been brought by theoretical investigations. In the work of Grillo et al.[40] they used Spin-density functional theory and on-site Coulomb interactions (GGA+U) to study water/$Fe_3O_4(111)$ interaction. The result validated the dissociation of the initial water molecule into OH groups over Fe sites (Fe_{tet1}) and H atoms on surface oxygen. Next H_2O molecule bridges the OH and H groups forming a hydronium-ion-like bridge structure OH_3^+-OH. The estimated adsorption energy of water dissociation and molecular H_2O over the hydroxylated magnetite surface were -95.40 and

-75.34 kJ/mol, respectively. As reported by Rim et al. [112] dissociative pathway has an adsorption energy of about -126 kJ/mol and is more stable than molecular adsorption by 47 kJ/mol.

Another attempt applying DFT predicted that water dissociation on $Fe_{oct2-tet1}$ terminated $Fe_3O_4(111)$ is energetically favorable at low coverage.[113] Therefore, Li et al, [114] have addressed water adsorption on Fe_{oct2} and Fe_{tet1} terminated $Fe_3O_4(111)$. The calculations revealed that, adsorption on Fe_{oct2} (dissociative) is favorable over the Fe_{tet1} (molecular) terminations.

Obviously, differences and debates on these insights exist and studying the water/Fe_3O_4 interface remains a challenging task. One reason for this discrepancy is uncertainty regarding the surface termination (i.e. Fe_{oct2} vs Fe_{tet1} terminated) $Fe_3O_4(111)$ surfaces. Accordingly, identifying surface termination was the mandatory step in this study (Fe_{tet1} as mention in the previous Chapter) before going forward to investigate water adsorption. With this knowledge about surface termination will enable us to rationalize our results.

This chapter demonstrates the influence of the crystallographic orientation of magnetite films on water adsorption. The main results of this section are published in references [22, 115, 116].

4.2 Water Adsorption on $Fe_3O_4(111)$

4.2.1 Temperature programmed desorption

Herein D_2O is used instead of H_2O to differentiate between the water we introduced on the surface and the one that present in the background of the vacuum chamber.

Figure 4.1 displays TPD spectra for different water (D_2O, m/z = 20 amu) exposures (in Langmuirs (L), 1 L = 10^{-6} Torr $\times$ sec) upon adsorption at room temperature (RT) on $Fe_3O_4(111)$, and heating to 700 K with a heating rate 3 K/s (the spectra cut at 600 K). The TPD spectra show a broad desorption feature within 320 - 380 K range for each exposure, which suggests that adsorbed water molecules are interacting strongly with $Fe_3O_4(111)$. Moreover, a small amount of water ($\sim$ 0.1 L) is sufficient for saturating the desorption signal. After this observation of water desorption above room temperature,

$Fe_3O_4(111)$ films were always flashed to 900 K in UHV prior to measurements. In a further step, water adsorption on $Fe_3O_4(111)$ film was conducted at lower adsorption temperature (T_{ads} = 140 K).

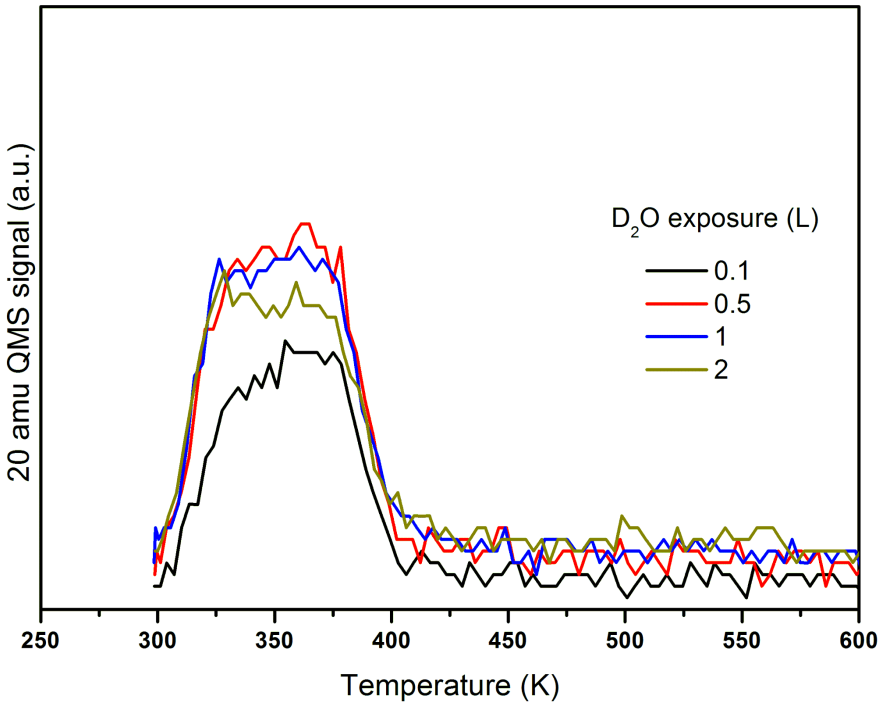

Figure 4.1: TPD spectra of D_2O (20 amu) adsorbed on $Fe_3O_4(111)$ at RT upon increasing exposures as indicated. The heating rate is 3 K/s.

Figure 4.2 shows TPD spectra measured upon increasing of D_2O dosage at 140 K and heating to 700 K with a heating rate of 3 K/sec (the spectra cut at 600 K). As the dosage increases, several desorption peaks appear ranging from ∼160 to 375 K.

At low water exposure (0.1 and 0.15 L), there are two desorption peaks at 375 and 315 K. The first one at ∼375 K, can originate from adsorption on surface defects and may even be saturated by reaction with water in the UHV background during cooling of the sample to 140 K. The second desorption signal at ∼315 K, shifts to lower temperatures with increasing coverage and gives rise to very broad signal centered at 290 K. This signal is characteristic of second order desorption kinetics. Second order desorption kinetics corresponds to recombinative desorption of dissociated water molecules.

Increasing water exposure (up to 1 L) results in evolution of several sequentially populated desorption peaks at 201 K, 223 K, and 255 K. The peaks' position is almost unchanged with increasing water coverage, thus exhibiting 1^{st} order desorption kinetics.

Upon further water exposure (> 1 L), a new desorption signal at ∼160 K starts to grow. This signal exhibits a common leading edge, which is characteristic of zero-order desorption kinetics. It does not become saturated upon further exposure and is consistent with the formation of amorphous solid water (ASW), or "ice" for brevity.

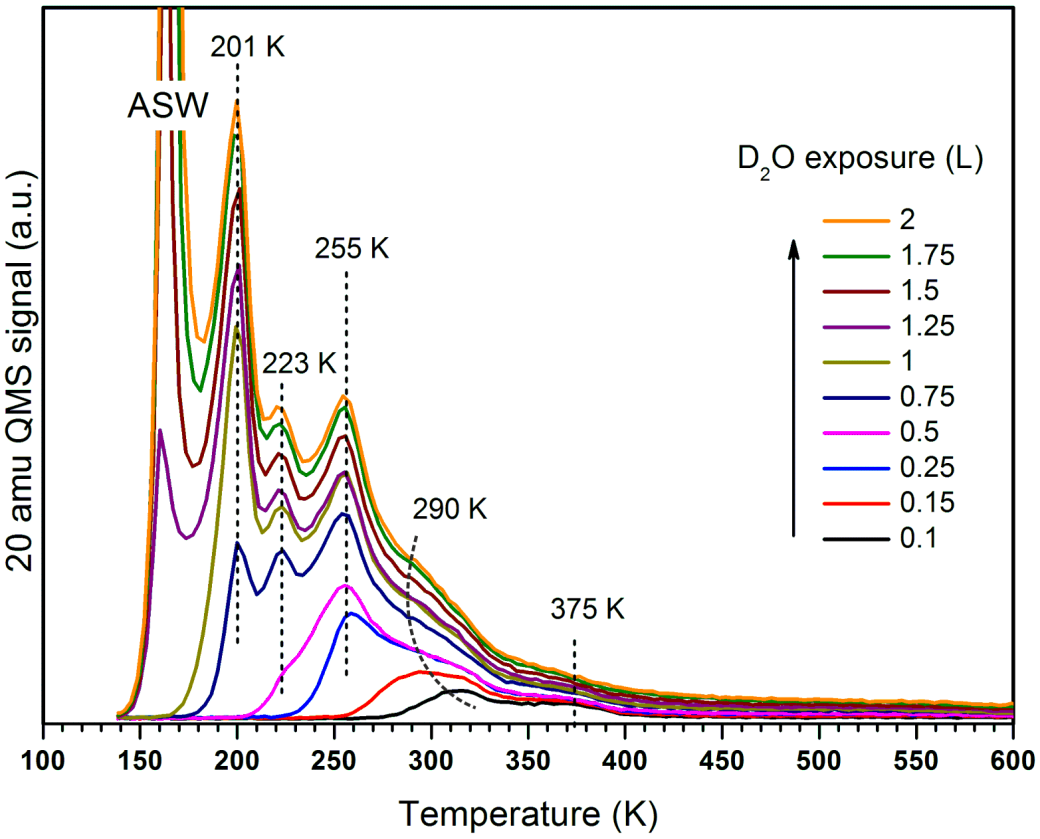

Figure 4.2: TPD spectra of D_2O (20 amu) adsorbed on $Fe_3O_4(111)$ at 140 K at increasing exposures as indicated. The heating rate is 3 K/s and the formation of amorphous solid water is indicated by ASW.

Our TPD spectra shows some similarities to those presented in other studies (ref.[106–108]). However, their TPD spectra displayed broad feature-

less desorption traces in the 200–300 K range, probably, due to the surface heterogeneity and/or experiments conditions. In contrast, our spectra shown in figure 4.2 have well-resolved desorption peaks.

It is important to mention that similar desorption peaks have been noticed for water adsorbed on the $Fe_3O_4(111)$ selvedge surface of hematite $Fe_2O_3(0001)$ natural crystal.[110, 112] The authors interpretation was that these peaks have multiple adsorption sites which exposed different terminations, that unavoidably formed during this surface preparation. Of course that is not the case for our films. As mentioned in previous Chapter on CO adsorption, our films expose a single, i.e. Fe_{tet1}, termination.

To quantify water coverage on $Fe_3O_4(111)$, TPD spectra of D_2O adsorbed on the clean Pt(111) surface were performed for calibration. Water interaction on Pt(111) surface is studied in ref. [117, 118]. Several studies have reported the formation of different structures of well-ordered hexagonal ice "bilayer" on Pt(111) surface. High resolution helium atom scattering measurements were able to determined two highly ordered ice bilayer phases. $(\sqrt{37} \times \sqrt{37})$R25.3° symmetry was interconverted to $(\sqrt{39} \times \sqrt{39})$R16.1° upon completion of the water layer, because water molecules were able to be compressed and rotated to form these supercells.[119] Further growing of a thicker ice bilayer on Pt(111), a hexagonal $(\sqrt{3} \times \sqrt{3})$R30° LEED pattern was observed.[120, 121] $(\sqrt{3} \times \sqrt{3})$R30° superlattice has been considered as a model water structure at interfaces, due to the fact that is has been broadly detected on various metal surfaces such as, e.g. Ru(001)[122], Ni(111)[123], and Rh(111)[124]. The crystalline ice growth on Pt(111) proceeds layer by layer up to the formation of three-dimensional (3D) islands following Stranski-Krastanov (SK) growth mode.[125]

Alternative models have been introduced to determine the positions of the O and H atoms at the contact layer between water molecule and Pt(111). Figure 4.3 (a, b) displays the "ice-like" bilayer model ("H-up") and the flat model "H-down" respectively.

The "standard" model is water "bilayer". It commonly describes the structure of intact water molecules. Bilayer consists of two layers (upper and lower) of water molecules which have six water molecules bonded via hydrogen bond to form a puckered ring on a metal as illustrate in figure 4.3(a).

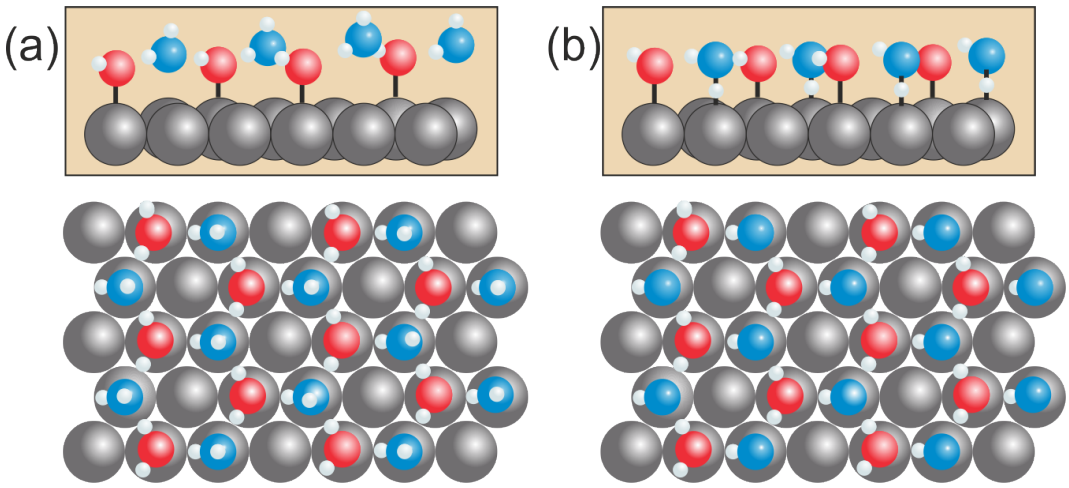

Figure 4.3: The structure of ice bilayer on Pt(111) (side and top view). (a)The red spheres represent O atoms of water molecules bind directly to the surface (lower layer). The blue spheres are O atoms of water molecules (upper layer) directed toward the vacuum in the H-up configuration. (b)the flat ice structure. Adapted from Ref. [126].

The flat ice structure model (figure 4.3 (b)) have been proposed by the authors in ref.[126]. The water molecules are adsorbed through alternating metal-oxygen (M-O) and metal-hydrogen (M-HO) bonds to the surface and to each other through the in-layer H bonds, creating a buckled 2D hexagonal network overlayer.

By conducting TPD measurements on the same setup and using the same Pt(111) crystal that used to grow Fe_3O_4(111) film, all apparatus effects are self-cancelled. Figure 4.4 shows TPD spectra of water adsorption on clean Pt(111) at 100 K. The spectra are very similar to that presented by Haq et al.[121] and showed two main peaks. The first peak at 174-178 K, is associated with the first water bilayer desorption. The second peak at 155-160 K is associated with desorption from multilayer ice.

Likewise, the LEED pattern of water on Pt(111) at 110 K was monitored at 55 eV upon increasing exposures. Up to 1.25 L water exposure no additional LEED spots have been viewed, but above that the $(\sqrt{3} \times \sqrt{3})$R30° pattern was observed. The inset of figure 4.4 shows the LEED pattern of 2 L water on Pt(111) at 110 K.

The water coverage in monolayer (ML), is defined as the number of water

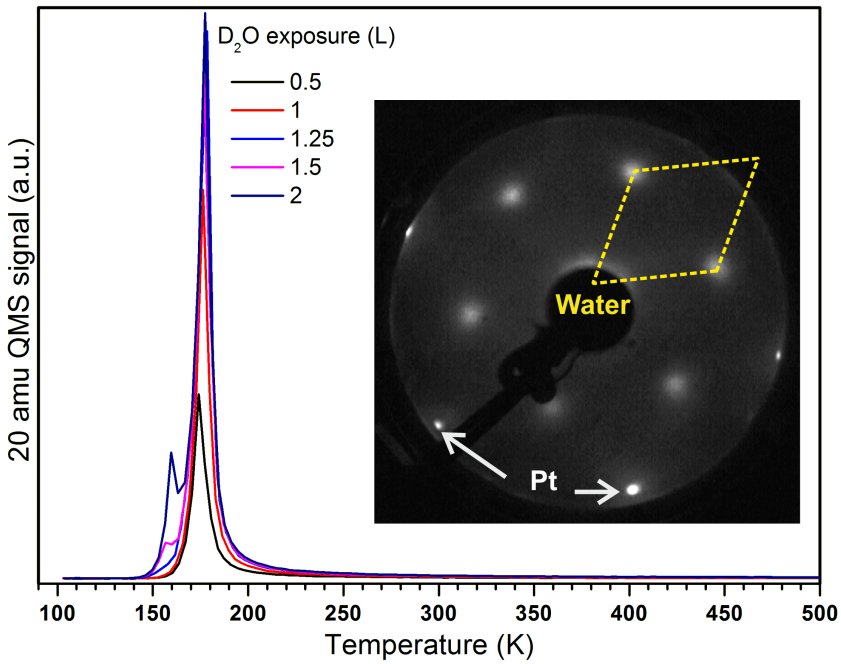

Figure 4.4: D_2O (20 amu) TPD spectra following indicated exposures on Pt(111) at 100 K. The inset shows $(\sqrt{3} \times \sqrt{3})$R30° LEED pattern (at 55 eV) of 2 L D_2O on Pt(111) at 110 K.

molecules that adsorb on Fe_3O_4(111) surface, normalized to the number of water molecules on clean Pt(111) surface. The coverage on Pt(111) was estimated from the integrated area of the thermal desorption peak of TPD spectra that obtained form D_2O adsorption on clean Pt(111) surface measured prior to film growth (knowing that 1 water BL = 1.2×10^{15} cm^{-2}). Using this value for calibration and assuming the saturation coverage of ideal bilayer ice forms a $(\sqrt{3} \times \sqrt{3})$R30° LEED structure on Pt(111), the water coverage was estimated. Considering the lattice constant of Pt(111) and the outermost Fe cations of Fe_3O_4(111) are 2.77 Å and 6 Å, respectively. 1 ML of water on Fe_3O_4(111) corresponds to 3.2×10^{14} cm^{-2}, i.e. one water molecule per Fe_3O_4(111) unit cell. The results showed that the total amount of water that adsorbs on Fe_3O_4(111) prior to the ASW film growth, corresponds to 2.3 ± 0.2 ML.

4.2.2 LEED

Inspired by TPD showing sharp desorption peaks raises the question: Does water on Fe_3O_4(111) form ordered structures, and what do they look like? To

verify this, we employed LEED. LEED patterns were monitored for different water exposures at 140 K. Of course, precautions had to be taken to minimize possible electron beam induced effects on the water ad-layer.

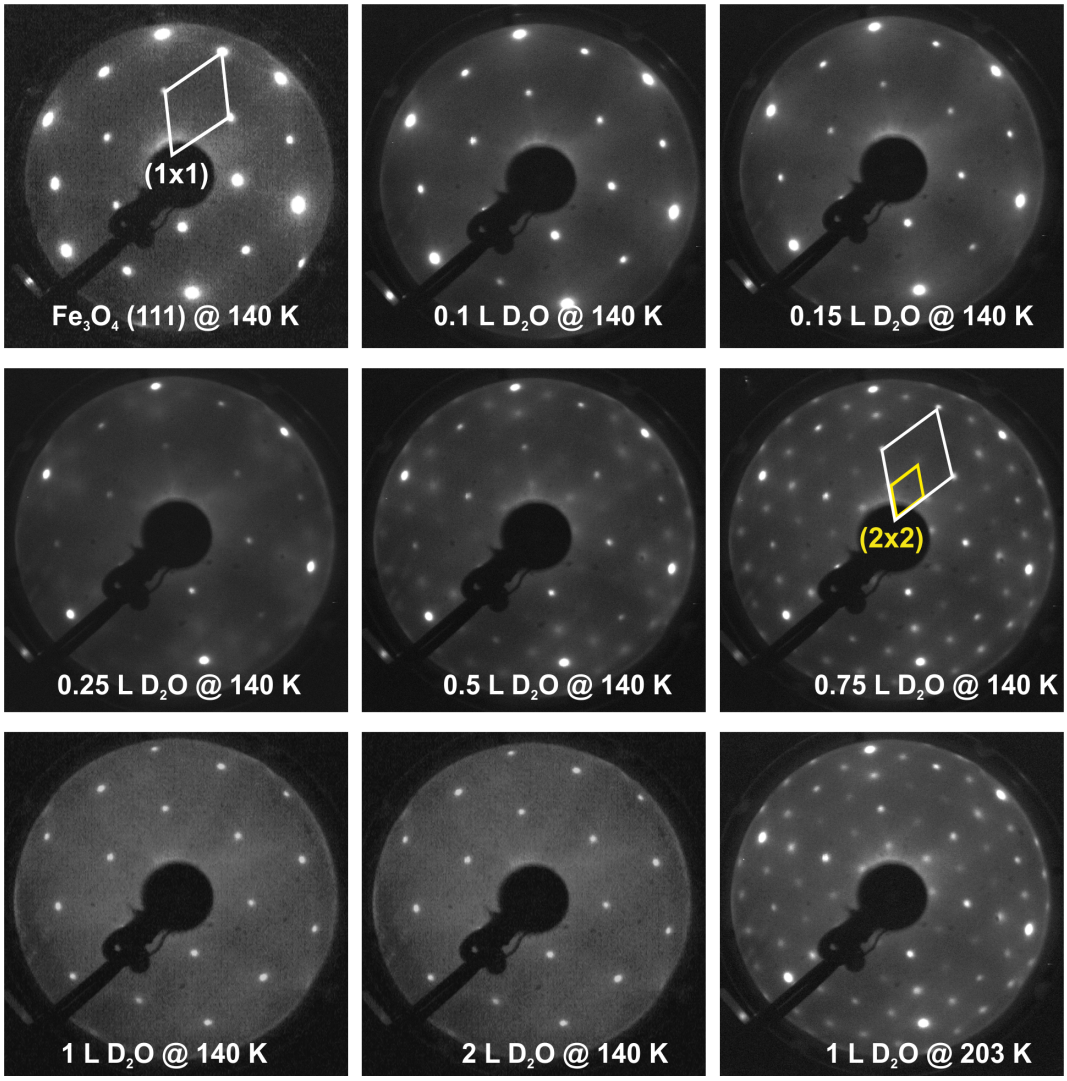

Figure 4.5: LEED patterns at 64 eV following the indicated exposures of water on $Fe_3O_4(111)$ at 140 K and 1 L at 203 K. Rhombus in white and yellow indicate the unit cells for $Fe_3O_4(111)$ (1×1) and water (2×2) overlayer, respectively.

The general behavior of LEED patterns (at 64 eV) as a function of water exposures at 140 K on clean $Fe_3O_4(111)$ are shown in figure 4.5. The clean $Fe_3O_4(111)$ surface shows a sharp (1×1) LEED pattern. At low water coverage (0.1 and 0.15 L) no additional spots are observed. Upon increasing water

coverage (0.25 L) new additional weak and diffuse spots appear. Then these spots become sharper and more intense, giving a (2×2) LEED pattern as the exposures increases (0.5 and 0.75 L). These ordered structures are observed at coverages that coincide with those that have a sharp TPD desorption peaks at 201, 223, and 255 K as in figure 4.2.

With further increases of water exposures to 1 L or higher, the LEED (2×2) of water ad-layer disappears. However, the Fe_3O_4(111) (1×1) LEED pattern is still visible. ASW formation can explain the disappearing of (2×2) LEED structure. Remarkably, the TPD spectrum for 1 L lacks the ASW desorption peak (figure 4.2), even though no (2×2) superstructure is observed. Perhaps the surface adsorbs slightly higher than 1 L water that might be coming from the UHV background (especially after many days of working with water), as water is always present in the UHV background .

It is important to point out that the (2×2) structure appeared in LEED immediately upon electron exposure and showed no visible intensity attenuation (or gain), at least, in minute's scale. Therefore, the beam induced effects on the observed ordering of water ad-layer can be safely ruled out.

Based on the above observations, it seems that at certain coverages water molecules develop a long-range ordered (2×2) structure through the formation of a hydrogen-bonding network, as its minimum energy structure. The ordered pattern is not observed by LEED at low water coverages. This can be explained as follows: the low coverage is not enough to form ordered structure. Moreover, if water molecules are formed in small-range ordered or random clusters, this will be not seen by LEED (typical coherence length is 10–20 nm).

To avoid ASW formation, we increased the adsorption temperature of 1 L water to 203 K, and the LEED pattern shows spots with a symmetry (2×2). This suggested that increasing the surface adsorption temperature allows greater mobility of the water molecules such that more stable bonding configurations can be formed.

Ordered water ad-layer have been reported on a few oxides surfaces, for instance, ZnO(10-10) [127] where half-dissociated water dimers form a (2×1) superstructure. The MgO(001) system has been studied in detail experimentally [128, 129] and theoretically [130]. Water/MgO(001) interfaces have displayed c(4×2) and p(3×2) LEED patterns. DFT calculations described two

stable structures depending on the temperature. A c(4×2) structure is stable at low temperature and consisted of 1.25 H_2O per MgO(001) unit cell (ten water molecules in the supercell). At high temperature, a p(3×2) structure is more stable containing 1 H_2O per unit cell (six water molecules per cell).

The LEED patterns of 1 L D_2O at 140 and 203 K (figure 4.5) open the question of whether the ordered water ad-layer depends on the coverage or on the adsorption temperature. Moreover, the TPD profile in figure 4.2, especially these three sharp desorption peaks that followed first order desorption kinetics, indicates the presence of water molecules having discrete binding energies and desorbing almost simultaneously at certain temperatures, hence implying a certain degree of ordering. Therefore, the entire LEED video is recorded simultaneously while heating the sample with the same heating rate as in TPD measurements (henceforth referred to as temperature programmed (TP)LEED).

After adsorption of 1 L water at 140 K, the (TP)LEED video at 64 eV is recorded during heating with heating rate 3 K/s. Figure 4.6 shows selected snapshots at different temperatures from the LEED video and synchronized with TPD profile during the desorption process. Clearly, the (2×2) structure only forms after water desorbs via the peak at 200 K and is still observed until 250 K. Water ordering is not observed by LEED at 300 K, i.e. in the relative abundance of dissociated water species.

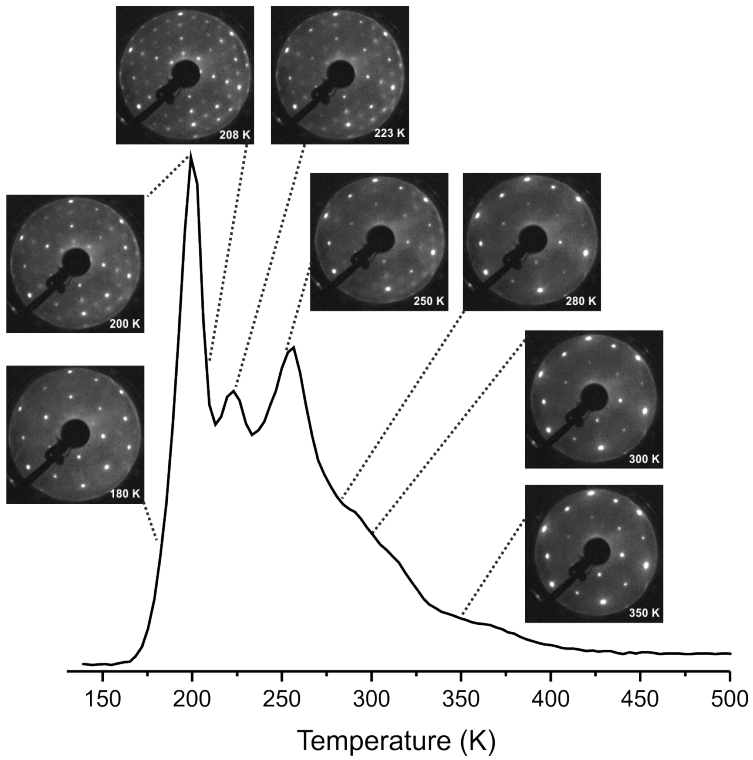

Figure 4.6: Sequence snapshots of LEED video (at 64 eV) during heating (3 K/s) of 1 L D_2O adsorbed at 140 K on $Fe_3O_4(111)$, and the temperatures are indicated.

The general behavior of LEED patterns as a function of temperature was independent of the initial water coverage above about one monolayer. Adsorption of water at higher temperatures produced LEED patterns similar to those seen at that temperature during desorption following low temperature adsorption. Therefore, the observed long-range ordering is thermodynamically driven and not kinetically limited, and only occurs at average coverages between 1.2 and 1.8 ML, as determined by calibration of a mass-spectrometer as described above.

In addition to the observation of (2×2) water overlayer, there are changes in the intensities of $Fe_3O_4(111)$ diffraction spots. Therefore, the intensity of the LEED spots through the whole video was investigated.

In principle, the intensity of a diffraction spot depends on the electron energy. The so-called I-V curves for several different spots are used for a quantitative analysis of ordered surface structures. Commonly, the I-V curve is collected by following the changes of both intensities and position of diffrac-

tion spots during energy sweeping. Increasing the energy range and the number of beams provides higher precision for the structure determination. In fact, it was the I-V LEED analysis that provided compelling evidence for the currently accepted models of both the $Fe_3O_4(111)$ [26, 27] and $Fe_3O_4(001)$-$\sqrt{2} \times \sqrt{2}$)R45° surfaces.[42] Basically, the surface geometry determines the positions of the peaks in I-V curves, whereas their intensities additionally include inelastic losses and thermal vibrations. Obviously, the adsorbate layer may alter the I-V curve, both peak position and its intensity, thus leading to intensity changes at the energy monitored. Taking into account sample damage by the electron beam and residual gas adsorption, precaution should be taken during measurements.

Three diffraction spots were selected for presentation in our study. (0,3/4), (0,1/2) and (0,1) characterize the water, Fe- and O- layers in $Fe_3O_4(111)$, respectively. The integral intensities of spots are presented after background subtraction. Figure 4.7 shows the spots intensities as a function of temperature together with the water desorption profile for 1 and 2 L water exposures.

First, the (2×2) spots, the water adlayer, appear at temperatures between 190 and 250 K, having a maximum at 208 K ±3 K. Meanwhile, the (0,1) spot, i.e. related to the O sub-lattice, shows a monotonous increase as the temperature increases for both 1 and 2 L exposures. Clearly, the signal of the oxygen-sub-lattice spot is very intense.

However, the situation for Fe sub-lattice (0,1/2) spot is different. At 1 L water (fig. 4.7 (a)), the intensity decreases at the beginning of water desorption, and starts to increase after water (2×2) disappears above 250 K. While the intensity profile of 2 L water (fig. 4.7 (b)), starts with intensity lower than at 1 L, once ASW layer has been desorbed the profile mirrors TPD (2 L), then again intensity increases.

Obviously, the intensity drop obtained at 150-250 K for (0,1/2) spot is linked to the shift of the I-V curve in the region close to the energy used here (64 eV), which suggests substantial changes in the Fe_{tet}-O interlayer distance at the oxide surface. This is likely because of the bond of terminal hydroxyl (O_wH) group to the surface Fe_{tet} cation.

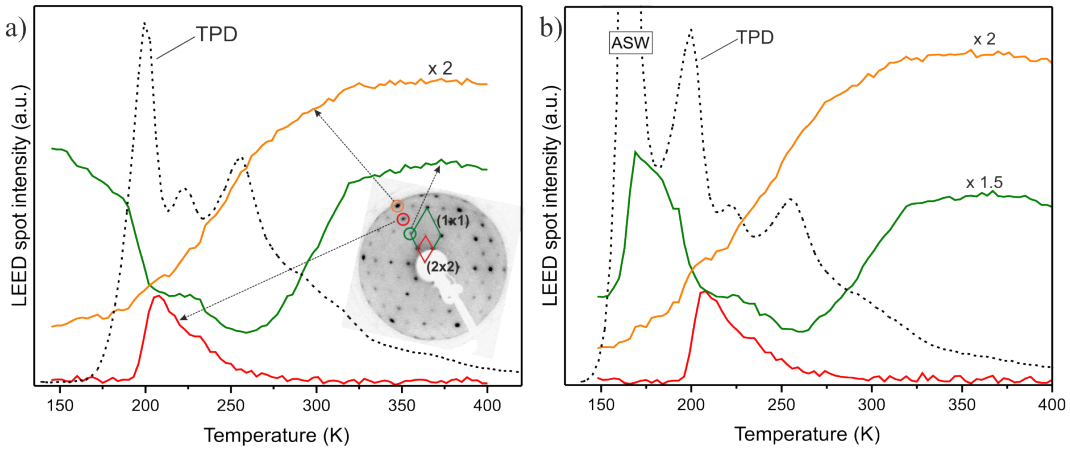

Figure 4.7: Intensity of the selected diffraction spots taken from the TP-LEED movie (at 64 eV) of $Fe_3O_4(111)$ exposed to (a) 1 L and (b) 2 L D_2O at 140 K. The TPD spectra are shown as dashed line and the unit cells are indicated in the inset (snapshot at 220 K).

The latter observation, in turn, raises a question about the intensity profile of these diffraction spots without water. Therefore, the TP-LEED of clean $Fe_3O_4(111)$ has been investigated. Figure 4.8 shows that (0,1) and (0,1/2) spots intensities of the bare $Fe_3O_4(111)$ surface remain almost the same through the investigating temperature range 140-400 K.

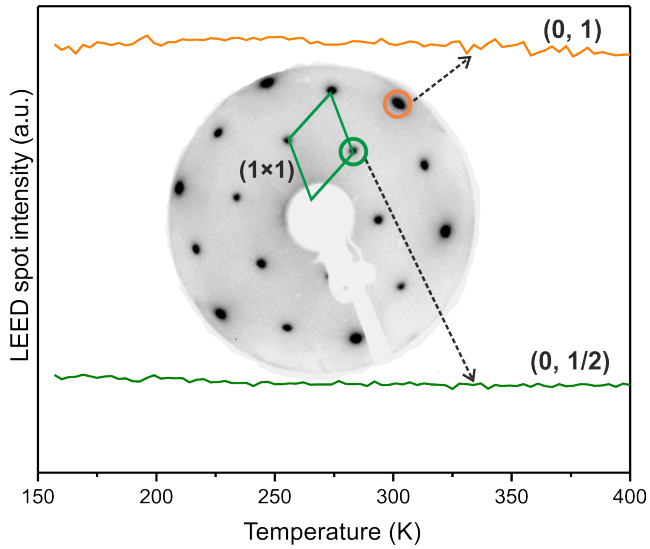

Figure 4.8: The intensity of the selected diffraction spots taken from the TP-LEED movie (at 64 eV) of clean $Fe_3O_4(111)$ (without water) and heating rate 3 K/s.

Such a behavior underlines the reliability of TP LEED intensities analysis for studying long-range ordered adsorbate/oxide interfaces, that result from the adsorption process. A quantitative evaluation of the results is not straightforward at this stage. To date, acquisition of the whole I-V data set during sample heating, which would shed more light on the TP LEED results, remains technically challenging. Our work is considered as the first step in this field. We are certain that experimental and theoretical efforts will lead to valuable results. For instance, the latter could provide a model for interplaying the interlayer distance through controlling the surface coverage, this would probably constitute an important advantage for coming future applications.

4.2.3 Desorption kinetics

In order to get insight into the reaction kinetics of water desorption, the obtained TPD data were utilized to estimate the desorption energy and pre-exponential factor. The activation energy for desorption can be extracted using different TPD analysis methods, i.e. inversion analysis of Polanyi-Wigner equation [85], "leading edge" analysis [82, 87], the Redhead analysis of peak maximum[75], and the heating rate variation method.

Figure 4.9 (a) shows the coverage of water as a function of temperature upon integration (Eq. 2.13, where β= 3 K/s) of desorption curve. Water coverage is normalized to the maximum (θ_{max}) obtained before the ASW related peak sets in. With making assumptions that ν= 10^{13} s^{-1}, and the desorption kinetic is first order, then following Eq. 2.14, the result shows that the desorption energy considerably decreases with increasing coverage, most markedly in the low coverage regime ($\theta/\theta_{max} < 0.1$), as display in figure 4.9 (b). Despite the fact that ν is independent of temperature and coverage, but the absolute values of E_{des} depends on its (ν) assumed value. Thus increasing the pre-factor to 10^{15} s^{-1} leads to a shift of all energies towards higher (i.e. more exothermic) values by about 15 kJ/mol.

Another approach that does not include any assumption about the pre-exponential factor is a "leading edge" analysis. In principle, the desorption leading edge of TPD spectra in figure 4.2 is approximated by the Arrhenius-type behavior. The analysis resulted in an energy of 68 kJ/mol at low coverage that gradually decreases with the increasing coverage as shown in figure 4.9(b).

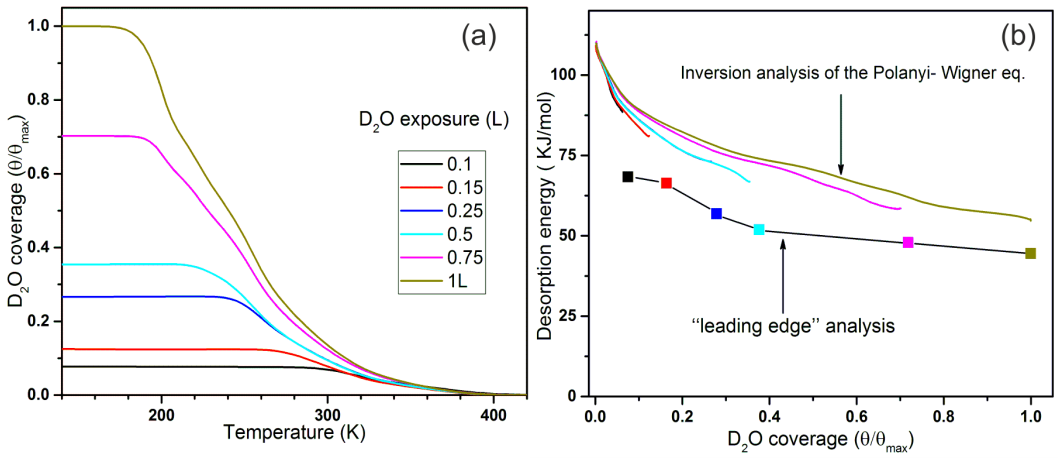

Figure 4.9: (a) Temperature-dependent of D_2O coverage after normalized to the maximum obtained before the ASW related peak sets in. (b) Desorption energy as a function of water coverage obtained by a "leading edge" analysis and by inversion analysis of the Polanyi– Wigner equation with a pre-factor $\nu = 10^{13}$ s^{-1}.

Table 4.1 presents the desorption energy obtained by the conventional Redhead analysis of peak maximum and assumed a pre-factor $\nu = 10^{13}$ s^{-1}. The values are a range of desorption energies from 50 kJ/mol for the peak at ∼200 K up to 95 kJ/mol for the peak at ∼375 K. Changing the pre-factor by one order of magnitude up (or down) increases (decreases) the desorption energies by approximately 5 kJ/mol. These results are very similar to those obtained by "leading edge" analysis, thus suggesting the pre-factor of 10^{13} s^{-1} as a good approximation.

Table 4.1: Desorption energy of water on $Fe_3O_4(111)$ obtained by: (1) Redhead analysis following Eq.2.17, using a pre-factor $\nu = 10^{13}$ s^{-1}. (2) HRV method for 1 L water (fig. 4.10 (f)).

T_m (K)	Desorption energy kJ/mol	
	Redhead	HRV
200	50	61
223	57	73
255	65	84
290	75	–
375	96	97

The heating rate variation method (HRV) can be viewed as a particular

choice that provides us a way to calculate the pre-exponential factor, which, however, requires an assumption about the desorption order. This method is also suitable to determine desorption energy without any assumptions on the pre-exponential factor or the desorption order. Following Eq. 2.21, graphs of $\ln({T^2}_m/\beta)$ versus $1/T_m$ are constructed, and E_{des} is extracted from the slope of the linear fit. The intercept represented the pre-exponential factor, whereas ν is coverage independent for first-order desorption processes.

A series of TPD spectra of a selected water exposures, lower than ASW formation, 0.1, 0.25 and 1 L are shown in figure 4.10 (a), (b), and (c), respectively, as a function of heating rate in the range of 0.25–5 K/s. The calculated values of E_{des} and ν are illustrated in figure 4.10 (d), (e) and (f) for 0.1, 0.25, and 1 L water exposures, respectively, for each fixed desorption peak.

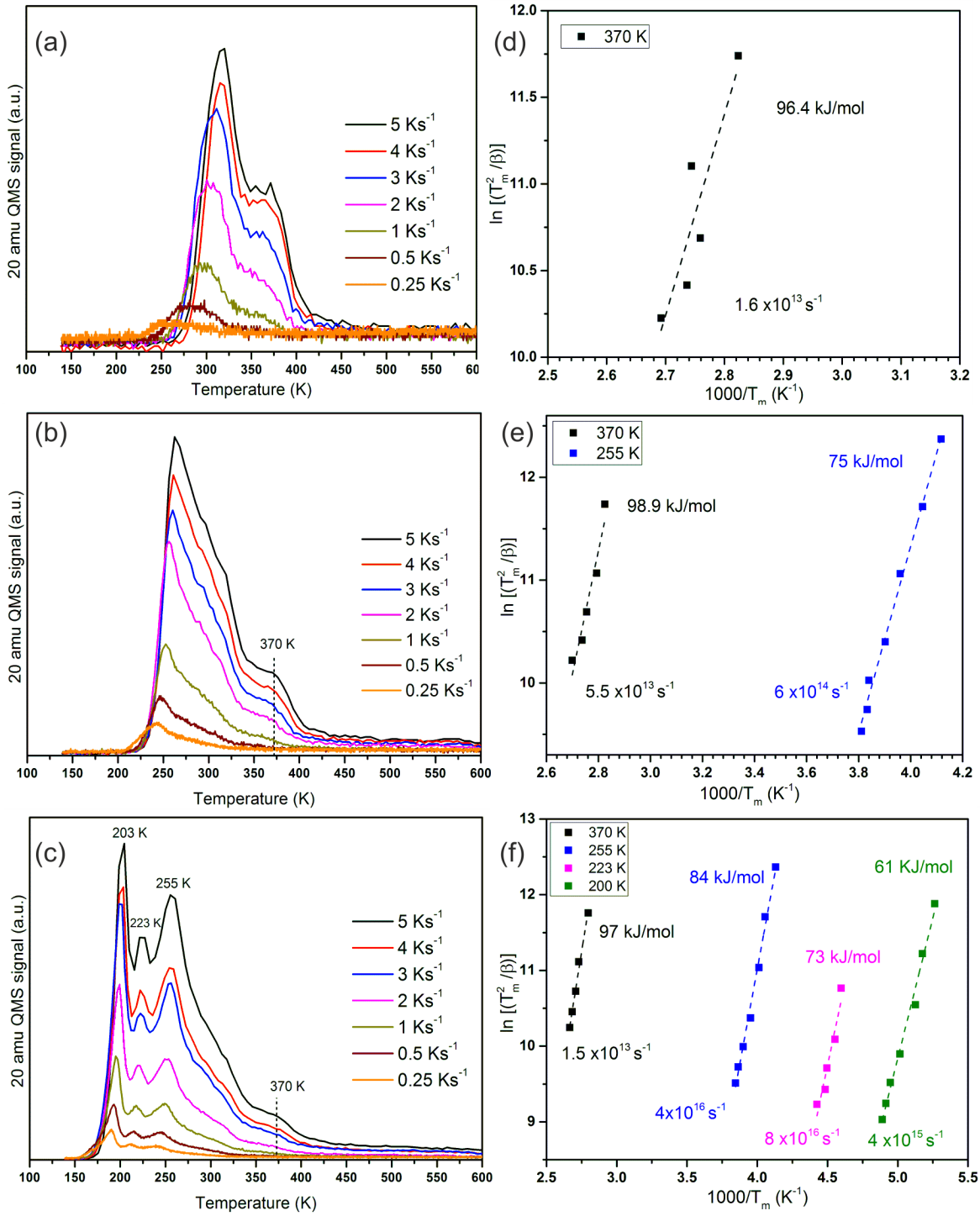

Figure 4.10: TPD spectra of water on $Fe_3O_4(111)$ at 140 K with a variable heating rates (as indicated) and at fixed exposure; (a) 0.1, (b) 0.25 and (c) 1 L. Whereas E_{des} and ν obtained from plotting $\ln({T^2}_m/\beta)$ versus $1/T_m$ are presented in (d), (e) and (f) for 0.1, 0.25, and 1 L water, respectively.

HRV method has often been employed for the analysis of very simple TPD spectra, having a single desorption peak, and at coverages lower than multilayer formation. To the best of our knowledge, this is the first time that the HRV analysis method was applied on such complicated TPD spectra (multiple desorption peaks), as on our case. Thus, to rationalize the obtained kinetics parameters via HRV with other analysis methods, that used here, we have to sum them on all exposures.

Using n=1 in HRV method, the obtained desorption energy (average value over all exposures) for each desorption peak are summarized as follows; E_{370K}= 97.5 kJ/mol, E_{255K}= 79.5 kJ/mol, E_{223K}= 73 kJ/mol, and E_{200K}= 61 kJ/mol. This result is in agreement with the data obtained from other methods. Whereas, the pre-exponential factor values (average) obtained from the intercept of the linear fit are ν_{370K}= 2.8×10^{13} s^{-1}, ν_{255K}= $5\times10^{15\pm1}$ s^{-1}, ν_{223K}= 8×10^{16} s^{-1}, and ν_{200K}= 4×10^{15} s^{-1}.

Clearly as displayed in figure 4.10 (b) and (c), the desorption signal at ∼300 K, which follows second desorption kinetics, at 0.25 and 1 L water exposure is difficult to follow. However, at 0.1 L (fig. 4.10 (a)) the water coverage is not enough to saturate this state, therefore, it appears as a cut off edge. Thus, the kinetic parameters could not be extracted. It should be mentioned that large errors were notified for a second or higher-order process because desorption energy and ν are surface coverage dependent.[88]

Moreover, the desorption energies based on Redhead's peak maximum and HRV analysis methods are gathered in table 4.1 for comparison. There are small variations between the calculated values, i.e., at 200, 223, and 255 K, whereas the exact energy is obtained at 375 K. The latter is due to the perfect match between the calculated and assumed pre-exponential factor in both analysis methods, which is not the case on other temperatures.

Finally, it is important to note that the desorption energy values that obtained via all previous analysis methods fall in the range of 115 kJ/mol at low coverage and decreases with increasing coverage to 50 kJ/mol. Our results are in excellent agreement with data obtained by single crystal adsorption calorimetry (SCAC), ranging from 100 to 55 kJ/mol upon increasing coverage.[109] Most of observed variations in our data of both the prefactor

and desorption energy can be attributed to the distinct analysis methods we employed.

4.2.4 Infrared reflection-absorption spectroscopy

Apparently the above TPD investigation is able to provide only insights about how water desorbs from $Fe_3O_4(111)$ surface, while vibrational spectroscopy is a very important tool to identify adsorbed water species on the surface. Therefore, TPD measurements have been complemented by IRAS investigation. In another UHV chamber, IRAS measurements were carried out on $Fe_3O_4(111)$ films prepared using the same recipe and flashed to 900 K prior to water exposure. Furthermore, TPD and TP LEED measurements were repeated. Again, as in the first UHV chamber, the water ad-layer was found to order in a (2×2) superstructure and TPD spectra revealed similar desorption profiles. These results have further strengthened our confidence to link the TPD and the IRAS results obtained in two different setups.

Figure 4.11 provides the spectra taken upon increasing water (D_2O) exposure on $Fe_3O_4(111)$ at 250 K. At low coverage, the spectra display two bands at 2723 and 2680 cm^{-1}. Upon further increasing exposure, both signals gain considerable intensity, but one shifts to a lower frequency 2718 cm^{-1} while another to a higher frequency 2685 cm^{-1}. This shift is quite small and is close to the spectral resolution 4 cm^{-1}. In addition, a weak broad band that centered at 2570 cm^{-1} starts to grow with increasing exposure. The latter band falls in the range of hydrogen bonded OD species.

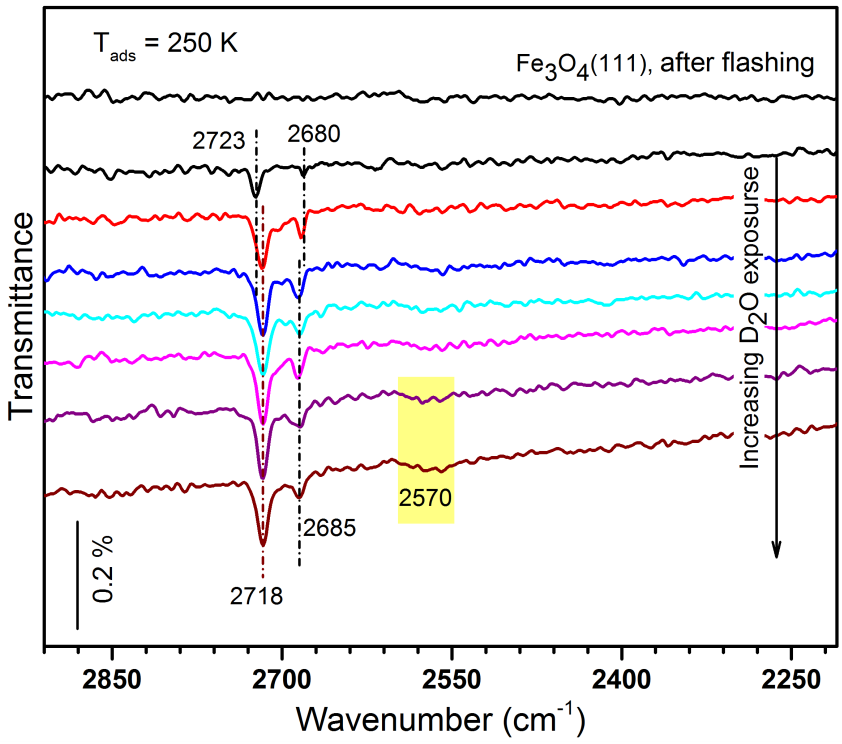

Figure 4.11: IRA spectra of D_2O adsorbed on $Fe_3O_4(111)$ as function of increasing water exposure at at 250 K.

On the basis of DFT calculations, dissociation of a single water molecule on both terminations of $Fe_3O_4(111)$ have been investigated.[109, 114] Table 4.2 summarizes the calculated frequencies. Taking into consideration that terminal O_wD hydroxyl bonded to the Fe cation and surface hydroxyl O_sD (the water proton transferred to surface oxygen) are the expected product from dissociation process. Experimentally, no vibrational bands related to Fe_{oct2} termination were observed. This can be considered as further evidence to discard that $Fe_3O_4(111)$ surface is Fe_{oct2} terminated.

Table 4.2: The computed frequencies in cm^{-1} for hydroxyls groups resulting from dissociation pathway of a single water molecule on $Fe_3O_4(111)$ data are from Ref [109, 114].

	Fe_{oct2-}	Fe_{tet1-}
O_wD	2754	2729
O_sD	2440	2705

While the predicted values of hydroxyl groups over Fe_{tet1-} are very close to the experimental data, in order to identify the origin of 2723 and 2680 cm^{-1} signals isotopic experiment is needed. Isotopically labeled IR investigation is always considered a helpful tool to recognize the different nature of adsorbed species. Therefore, $Fe_3{}^{18}O_4(111)$ and $Fe_3{}^{16}O_4$ (111) were prepared with ^{18}O and ^{16}O, respectively. IR spectra obtained after D_2O adsorption at 250 K are shown in figure 4.12 for comparison.

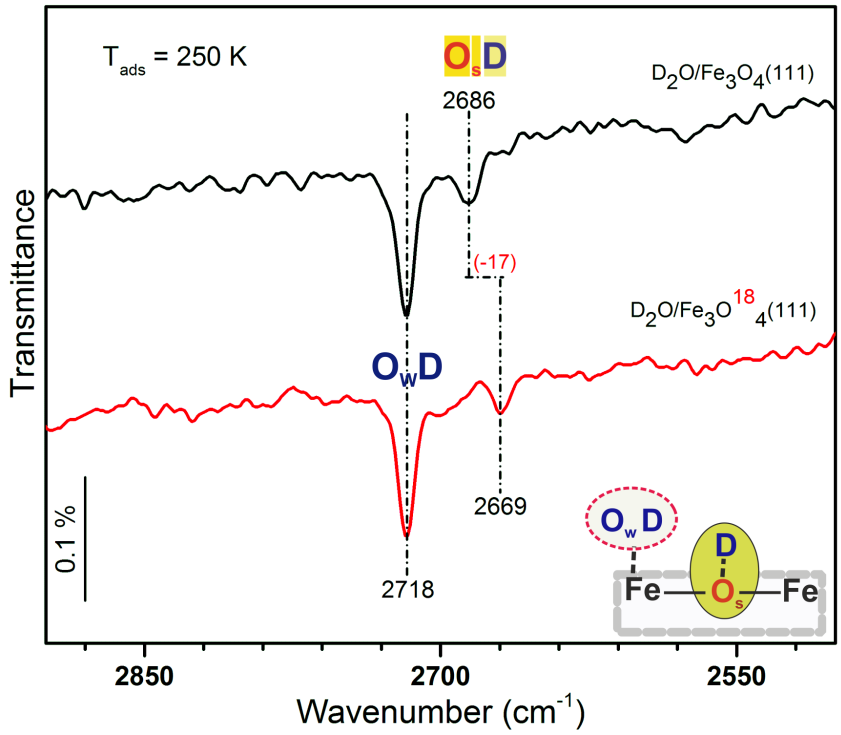

Figure 4.12: Infrared spectra for the adsorption of D_2O on $Fe_3O_4(111)$ prepared with O^{16} (black spectrum) and with O^{18} (red spectrum). The spectra are collected at 250 K and under saturation conditions.

The labeling of surface oxygen results in a frequency shift of about 17 cm^{-1} for the band at 2686 cm^{-1}. Whereas, in the case of adsorbing $D_2{}^{18}O$ (ref.[115] for more details) the band at 2723 cm^{-1} red-shifts $\sim$ 17 cm^{-1}. Consequently, the vibration bands that are experimentally observed at 2723 and 2686 cm^{-1} must be assigned to terminal Fe-O_wD and surface O_sD, respectively.

The main outcome here is that the dissociation of a single water molecule on $Fe_3O_4(111)$ supports the "classical" adsorption model that has been earlier proposed.[108] We would like to stress that surface preparation and vacuum conditions play a crucial role in the formation of a uniform Fe_{tet1}-terminated surface. The latter was probably not well controlled in Ref.[109], this may explain the disagreement with our results about water adsorption mechanism, particularly at low coverage.

4.2.5 Density Functional Theory

In principle, the structures of adsorbed water ad-layer at the water–oxides interfaces are determined by two fundamental competitive forces. Firstly, water-water interaction through the formation of hydrogen bond, as its minimum energy structure. The second force that primarily influential water–oxides connecting layer, is the water-oxides surface interaction.

Density functional theory (DFT) is a useful and supplemental tool that will refine a better understanding to rationalize experimental data. Hence DFT calculations were performed in Humboldt University Berlin, through the collaboration with Prof. Joachim Sauer group (Xiaoke Li and Dr. Joachim Paier). Following our observation of (2×2) ordered structure, the calculations were performed using a (2×2) slab. The calculations for the structural surface models, utilized asymmetric stoichiometric slabs comprising twelve atomic layers and a (2×2)-periodicity, i.e., the clean Fe_{tet1}-terminated $Fe_3O_4(111)$ surface has a cell content equivalent to $Fe_{48}O_{64}$.

As the first water molecule undergoes dissociation pathway, the DFT calculations predicted two distinguishable stretching wavenumbers 2736 and 2699 cm^{-1} for O_wD and surface O_sD groups, respectively. When one compares these values with the observed bands (table 4.3), wavenumbers differences are in good agreement. The latter assignment is based on the assumption that the first appearing band at 2680 cm^{-1} is associated with adsorption on defects.

The strategy of the performed DFT calculations is based on populating the Fe_{tet1}-terminated $Fe_3O_4(111)$ surface ((2×2) cell) with water molecules one by one. As illustrated in figure 4.13 (structure 1), the dissociation of the first water molecule is the most thermodynamically favorable process, having

Table 4.3: The calculated and experimental observed vibrational frequencies in cm^{-1} for both hydroxyls groups O_wD and surface O_sD.

	$\nu_{Exp.}$	$\nu_{cal.}$
Fe_{tet1}-O_WD	2723	2736
O_SD	2685	2699
$\triangle\nu$	38	37

an adsorption energy of -123 kJ/mol. This results in occupying the surface with Fe_{tet1}-O_wD and surface O_sD hydroxyls groups "monomers". Once the second water molecule (i.e. 0.5 ML coverage) approaches the surface, it may either dissociate as the first one on available free sites (structure 2), or form a "dimer" complex (structure 2^{cl}) via anchoring to the preformed hydroxyls "monomer". Dimer complex refers to molecular water binding to dissociated water molecule. On the basis of calculated energies, -100 vs -104 kJ/mol per water molecule both processes are equally possible. Taking into account that the energy gain from monomer formation on the clean surface (-123 kJ/mol) is considerably high, it makes the oxide surface primarily covered by hydroxyls at coverages of nearly to 1 ML (i.e. four H_2O molecules in the (2×2) cell). However, the possibility of dimer formation cannot be excluded.

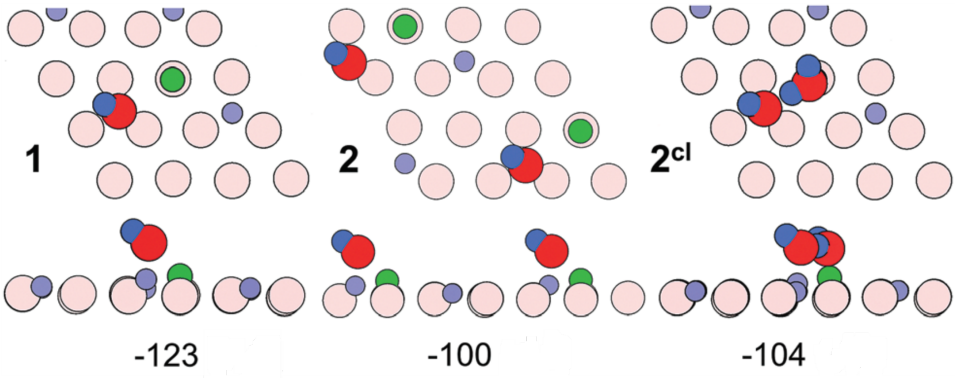

Figure 4.13: Top and side views of several computed structures on the Fe_3O_4(111)-(2×2) cell upon water adsorption. (1) A single dissociated water molecule, (2) two dissociated molecules, and (2^{cl}) a "half-dissociated" dimer complex. Adsorption energies per molecule (in kJ/mol) are displayed below individual structures. Color code; violet is surface Fe_{tet1} ions, pink is surface O_s ions, red is oxygen in water (O_w), proton atop O_s is green, hydrogen in water or hydroxyl is blue. Adapted from [116].

At 1 ML coverage, the surface is completely covered by "monomers" (O_wD and O_sD). Therefore, the fifth water molecule anchors to one of the monomers to form a dimer. The energy of chemical reaction for sequential water adsorption is calculated as in Eq. 4.1.

$$Fe_3O_4(111).nH_2O + H_2O \rightleftharpoons Fe_3O_4(111).(n+1)H_2O,$$

$$\triangle E(n) \ = E_{n+1} - (E_n + E_{H_2O}) \tag{4.1}$$

To analyze the LEED observation of water ad-layer, the coverage increases from 5 to 8 water molecules on (2×2) cell, i.e 1.25-2.0 ML. The structures and calculated energies $\triangle E$ at these coverages are well illustrated in figure 4.14.

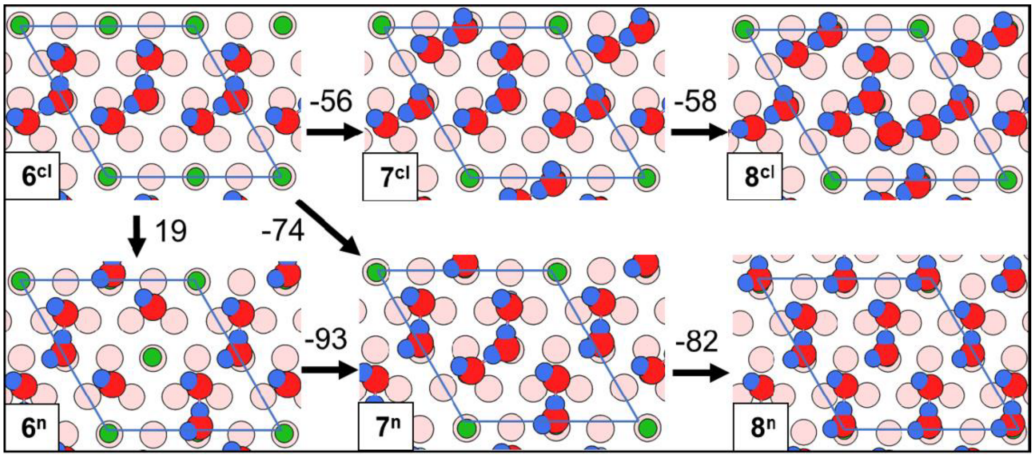

Figure 4.14: Several computed structures containing 6, 7 and 8 water molecules in a Fe_3O_4(111)-(2×2) cell. The top panel describes the formation of cluster (cl). The bottom panel represents development of the hydrogen bonding 2D-network (n). Reaction energies upon adding one H_2O are given in kJ/mol. Adapted from [115].

The obtained structures are formed through two different pathways: clustering and a hydrogen bonded network, henceforth labeled with the superscript cl and n, respectively. In the case of six water molecules (∼ 1.5 ML), the trimer 6^{cl} structure is more stable than a dimer and a monomer 6^n. Until the seventh H_2O molecule is added to either 6^{cl} or 6^n structures, both shows that 7^n is

the more thermodynamically stable structure.

Once the "network" structure 7^n is formed a 2 D network starts to grow through maximizing hydrogen bonds. Accordingly, the thermodynamically favored reaction pathway is a 2D water network formation. Establishing 8^n structure corresponds to our experimental (1×1) LEED pattern at 140 K before the appearance of (2×2) water ad-layer.

Let's summarize the outcome here: initially water dissociates formed two hydroxyl groups. The latter anchored the upcoming water molecules creating a dimer complex. Eventually water molecules arrange themselves through a hydrogen bonding network in a hexagonal arrangement showing a (2×2) LEED pattern in 7^n structure.

4.3 Water Adsorption on $Fe_3O_4(001)$

Several studies have combined experimental and theoretical tools in order to explain what happens at water/Fe_3O_4(001) interfaces. Theoretical studies by Mulakaluri et.al.[131, 132] have calculated coverages of 1, 2, and 4 H_2O per unit cell employing a standard GGA+U functional and a bulk-truncated surface model. The results pointed to dissociative adsorption at both defect sites and regular terrace. Moreover, the authors suggested that molecular and dissociative species coexist on the surface at high water coverage. The same conclusion has been drawn by Liu et.al.[133] applying AES, LEED, and high-resolution electron energy loss spectroscopy.

The Diebold's group [134] reported that dissociative adsorption of water at room temperature results in the hydrogenation of the lattice oxygen O_sH, which upon heating leads to the reduction of the surface. Remarkably, there was a lack of evidence for O_WH species on the surface. These results were obtained from Fe_3O_4(001) single crystal applying scanning tunneling microscopy (STM) and low-energy ion scattering (LEIS). Very recently, the same group drew more conclusions towards water adsorption on an Fe_3O_4(001) single crystal, applying TPD, XPS, and AFM.[135] These techniques were gathered with DFT calculations (considering the SCV structural model of Fe_3O_4(001)-($\sqrt{2}$ × $\sqrt{2}$)R45°) to determine the lowest-energy configurations of water molecules upon increasing coverage from 1 to 8 H_2O/u.c. For the clean surface (as

prepared), the empty-states STM image revealed slightly brighter protrusions assigned to the formation of the terminal O*H groups due to residual water adsorption. However, the DFT calculations, at 1 H_2O/u.c, indicated that the intact isolated water molecule is slightly (by 0.05 eV) more stable than a dissociated molecule (E_{ads}= - 0.59 eV). The latter forms two terminal hydroxyl groups, i.e. surface hydroxyl (O*H) and O_wH group (bound to Fe_{oct} ion). Interestingly, at 2 H_2O/u.c coverage, a partially dissociated water dimer is the most stable configuration of water (E_{ads}= - 0.92 eV per molecule), where one terminal OH and one H_2O, bound to neighboring surface Fe_{oct} atoms (see fig.4.15). Upon increasing coverage to 3 H_2O/u.c the energy degenerated due to the formation of two partially dissociated trimers, i.e. linear H_2O-OH- H_2O trimer and nonlinear isomer (ISO) trimer (labeled as E_3 and $E_{3\ ISO}$ in fig.4.15). The authors detected a discrepancy between their results and Mulakaluri et.al.[132], especially at low coverage, originated from a different structural model used in both studies. In the case of SCV reconstruction, the outermost four layers involve only Fe^{3+} ions, water preferred to interact molecularly. Whereas the bulk-truncated structure, the subsurface layers contains Fe^{2+} cations, promoted water dissociation.

To examine the effect of surface geometry on the adsorption process of water, we performed similar experiments on Fe_3O_4(001) films grown on Pt(001).

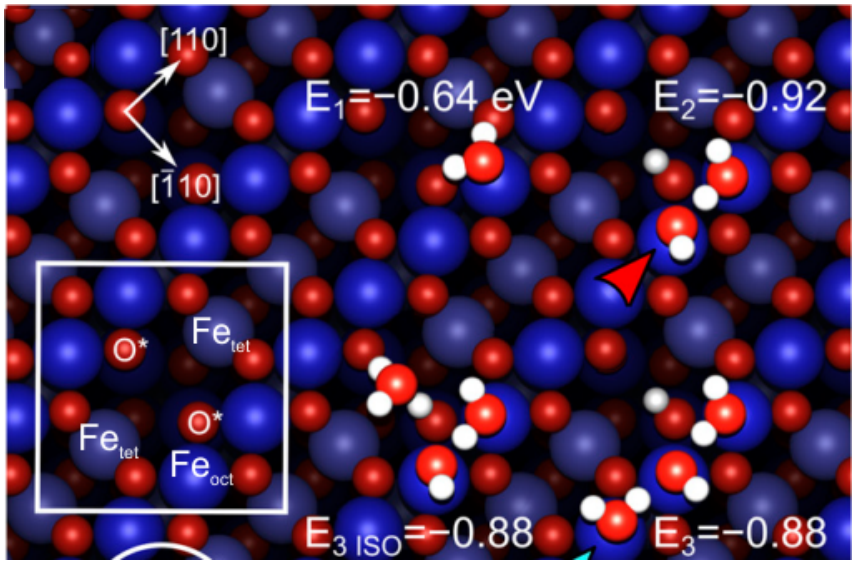

Figure 4.15: Top view of the minimum-energy water structure, at coverages of 1, 2, and 3 H_2O/u.c, derived by DFT. Adsorption energies are given in eV. The white square indicates $Fe_3O_4(001)$-$(\sqrt{2} \times \sqrt{2})R45°$ reconstructed unit cell, and the surface oxygen without a tetrahedrally coordinated Fe_{tet} neighbor in the second layer are marked by O*. Fe atoms are in blue. Adapted from [135].

4.3.1 Temperature programmed desorption

The TPD data collected at different exposures of D_2O at 140 K on $Fe_3O_4(001)$-$(\sqrt{2} \times \sqrt{2})R45°$ are presented in figure 4.16. The surface was heated to 700 K (spectra are cut at 500 K) with a heating rate of 3 K/s. Our spectra are in good agreement with the data that was recently obtained on $Fe_3O_4(001)$ single crystal. [135] Therefore, we can cross-correlate the results obtained in these two studies, labeling desorption peaks α, β, etc as in ref. [135]. For low exposures, a peak at 240 K (δ) appears first. That followed by peaks at 220 (γ) and 200 K (β) subsequently populated with increasing coverage. These three peaks are characterized by first-order (or close to) desorption kinetics. According to the calibration applying TPD and DFT investigations, the estimated coverages were 3, 6, and 8 D_2O/u.c., to saturate δ, γ and β peaks, respectively. [135] It is important to point out that the water signal above 250 K keep gaining intensity (tiny) upon increasing exposure (fig. 4.16), instead of all spectra sharing the same descending edge (ideal situation). Therefore, the desorption tail above 250 K is considered to be artificial due to the limitation of pumping

speed for the mass spectrometer.

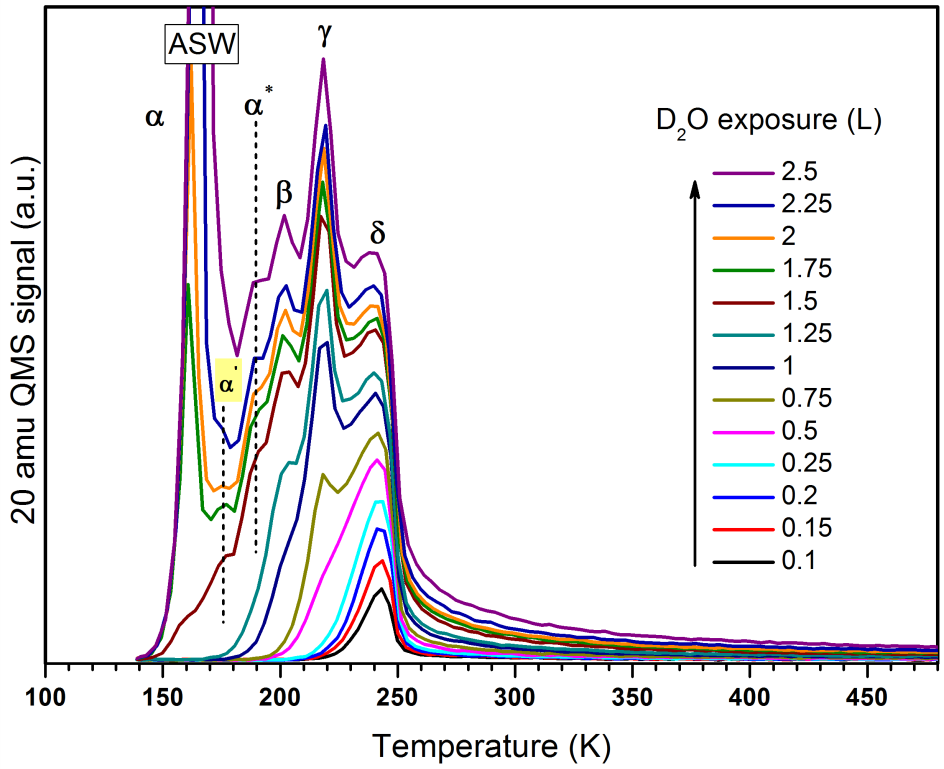

Figure 4.16: TPD spectra upon D_2O (20 amu) adsorption on $Fe_3O_4(001)$ at 140 K as a function of increasing exposure as indicated. The heating ramp was 3 K/s.

Starting at about 1.5 L, a peak at $\sim$ 188 K (α^*) develops between β and α' (177 K). Eventually, ASW desorbs at 160 K. It is important to note that at α^* peak appeared in our TPD spectra but not in Ref.[135]. Therefore, we put much effort into ensuring that the experimental results are solid and reproducible. Thus, further investigations on newly prepared samples varying the heating rate and deposition flux were performed. All obtained data reveal the existence of the α^* peak. When we consider that the two studies have different heating rate and adsorption temperature, the former observation can be explained.

The expected questions that might be interesting to address are whether the TPD profile, as well as the epitaxial growth of water ad-layer, will be affected by varying the crystallographic orientation of the magnetite film.

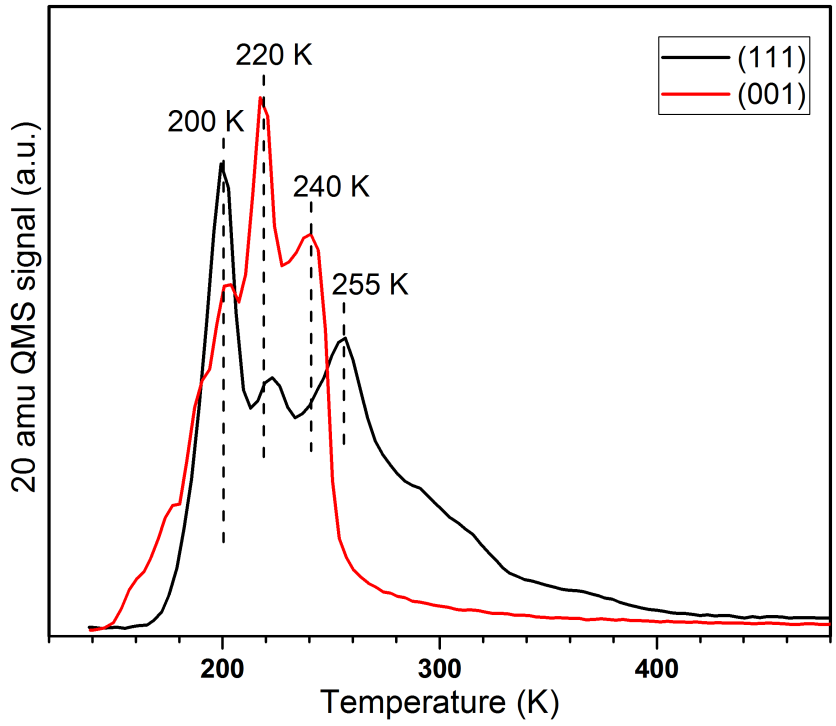

Figure 4.17: Comparison of TPD spectra obtained on Fe_3O_4(111) and (001) films after 1 and 1,5 L D_2O exposures, respectively. D_2O dosed at 140 K and the temperature ramping by 3 K/s.

Taking advantage of the fact that all TPD investigations have been done utilizing the same experimental setup, the spectra on both (111) and (001) can be safely compared. The outcome of the comparison is summarized in figure 4.17, where the TPD data for exposure prior to ASW formation of water at 140 K and heating rate 3 K/s on Fe_3O_4(111) and (001) films are shown. Both surfaces show some similarities and some differences.

Similarities clearly appear in the position of the β and γ peaks on the (001) films that almost coincide with desorption maxima at 200 and 220 K obtained on the (111) films, all peaks are related to molecular water adsorption.

At high temperatures, the differences are more obvious. In the case of (111), the surface displays a peak at 255 K and a long "tail" up to 400 K following second-order desorption kinetics due to water dissociation. While the desorption peak at 240 K, with a steep descending edge, on (001) surface showing pseudo-first-order desorption kinetics. The latter suggests that water adsorption on Fe_3O_4(001)-($\sqrt{2} \times \sqrt{2}$)R45° is either nondissociative or that

the hydroxyl groups resulting from dissociation do not separate on the surface during the TPD ramp and readily recombine.

4.3.2 LEED

Motivated by the latter observation of the resemblance between β and γ peaks on (001) with 200 and 220 K peaks on (111), that suggest water ad-layer on (001) may also form an ordered structure, a study on (001) was conducted using LEED. As noted early, the water superstructure on (111) is immediately observed at 200 K (fig.4.5).

Thus, the LEED pattern at 70 eV was monitored after Fe_3O_4(001)-($\sqrt{2}$ $\times$ $\sqrt{2}$)R45° film was exposed to 1.5 L at 200 K. No additional diffraction spots were observed. Therefore, this procedure was repeated for several exposures (1, 2, 3, 4, and 5 L), and for each of these, the LEED was taken at different electron energy i.e., 20, 40, 60, and 70 eV. Moreover, the adsorption flux, heating rate and adsorption temperature (at 200, 210, and 220 K) were all checked. Despite these many attempts, trying every possibility, it seems that water did not form an ordered superstructure on Fe_3O_4(001) surface under these conditions.

Previously, Mulakaluri et.al.[131] reported suppression in the ($\sqrt{2}$ $\times$ $\sqrt{2}$)R45° reconstruction upon water adsorption of 2 $\times 10^{-6}$ mbar for 2 min (i.e., $\sim$300 L) at 273 K. The same attenuation has been observed at 165 K for 0.01 L on Fe_3O_4/Mo(001).[133] The latter observation has been considered as indirect evidence for water dissociation, however surface termination was not precisely determined in that work.

To monitor any tiny changes in the reconstructed diffraction spots we inspected the LEED pattern at lower electron energy (E = 25 eV). LEED patterns were examined after adsorption of 1.25, 1.5, 1.75, 2, 2.5, 4, 5 and 6 L at 140 K, as displayed in fig. 4.18(b-i).

The clean Fe_3O_4(001)-($\sqrt{2}$ $\times$ $\sqrt{2}$)R45° reconstructed surface exhibits a sharp LEED pattern (fig.4.18(a)). No clear additional spots were observed after exposure of 1.25 L of D_2 at 140 K. At 1.5 L exposure, a very faint additional set of spots, highlighted in yellow circles, developed. Remarkably, at 1.75 L these additional spots become more intense revealing (2 $\times$2) symmetry (fig.4.18(d)). Increasing water exposure to 2 L, results in the disappearance

of (2 ×2) structure; additionally, the intensities of the oxide film diffraction spots get weaker upon increasing exposure. Finally, LEED disappears at water exposure above 4 L. It worth noting that 1.75 L is the only exposure revealing sharp (2 ×2) structure at 140 K.

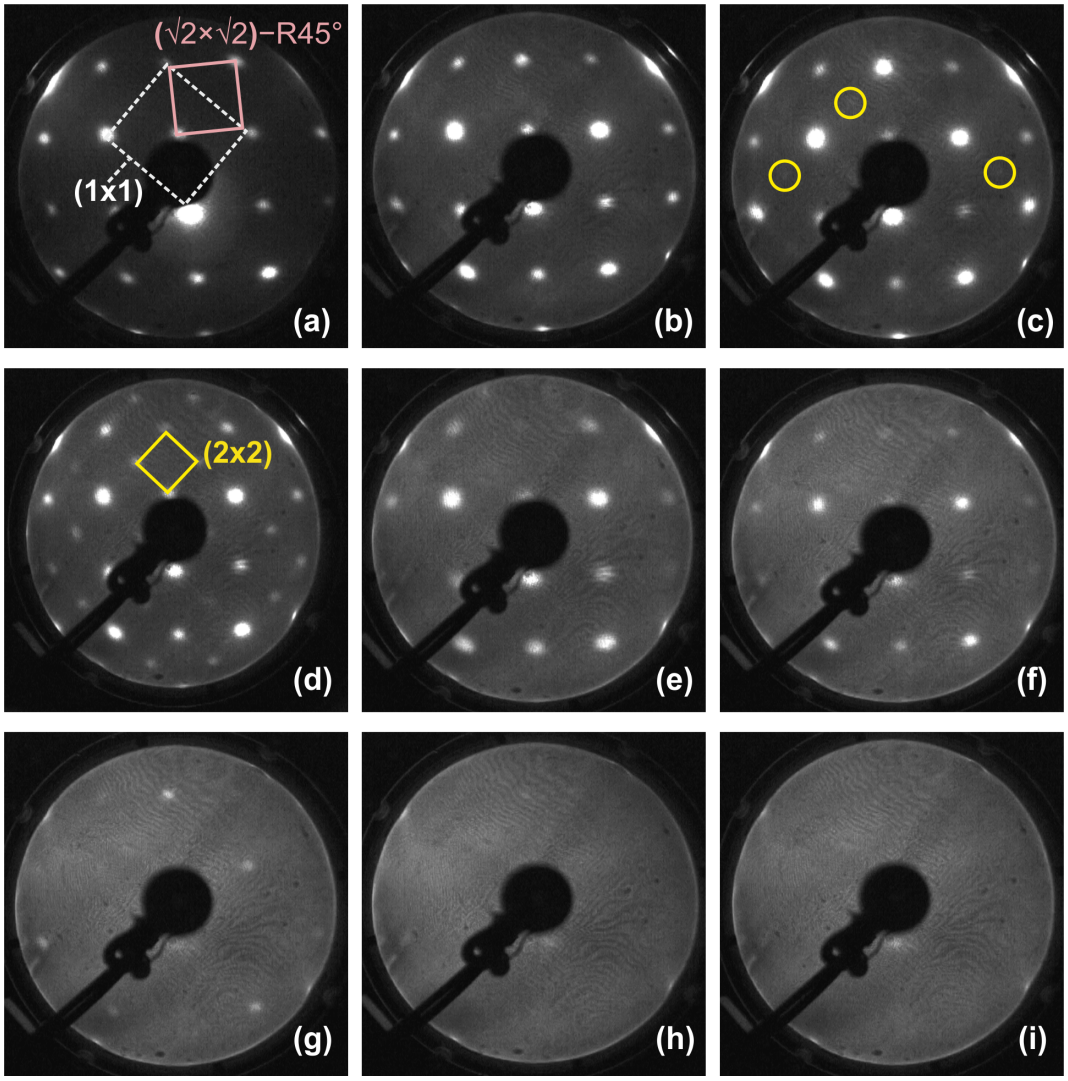

Figure 4.18: LEED patterns of $Fe_3O_4(001)$ as a function of increasing D_2O exposures; (a) without, (b) 1.25 L, (c) 1.5 L, (d) 1.75 L, (e) 2, (f) 2.5 L, (g) 4 L, (h) 5 L, and (i) 6 L at 140 K. All LEED measured at 25 eV. The unit cells are indicated.

Therefore, the TP LEED of 1.75 L water, adsorbed at 140 K, have been performed at 47 eV. A number of LEED patterns as a function of temperature

are shown in figure 4.19. As illustrated in the formation Fe_3O_4(001)-(2×2) structure is detected at 175-187 (±3) K. Importantly, the (2×2) symmetry of water ad-layer on (001) surface is observable for a small temperature window comparing with Fe_3O_4(111) surface (i.e., 200-250 K, see fig 4.5).

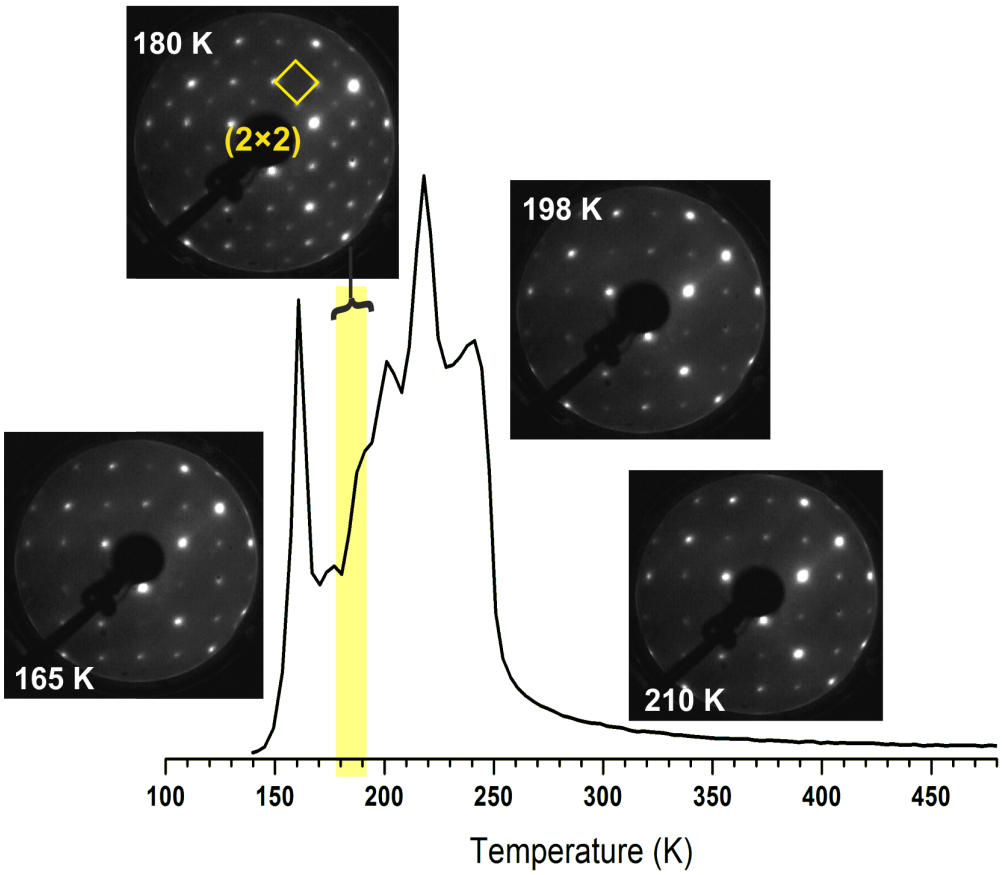

Figure 4.19: Selected snapshots from LEED video (E=47 eV) recorded during heating (3 K/s) of Fe_3O_4 (001)($\sqrt{2} \times \sqrt{2}$)R45° surface after adsorption of 1.75 L water.

The changes in the intensity with temperature, through the TP LEED video upon heating by 3 K/s, are shown in figure 4.20 (a, b) for 1.75 and 2.25 L water, respectively. The profiles present the average values for both ($\sqrt{2} \times \sqrt{2}$)R45° reconstructed surface (R-) spots and (2×2) water ad-layer

(W-) spots.

The W-spots, at 1.75 and 2.25 L, are observed for a very short period (i.e. 4 (±1) sec this about 12 (±3) K) having maximum intensity at ∼ 181 K. For comparison, the (111) surface reveals a wider temperature range, i.e., 200-250 K with maximum ∼208 K.

The R-spots show a dramatic response during water desorption; the intensity maximizes simultaneously with the appearance of the (2 ×2) water ad-layer structure. Then the intensity decreases and subsequently increases during desorption of β peak. Eventually after water desorption (via 240 K peak), the intensity stays almost unchangeable.

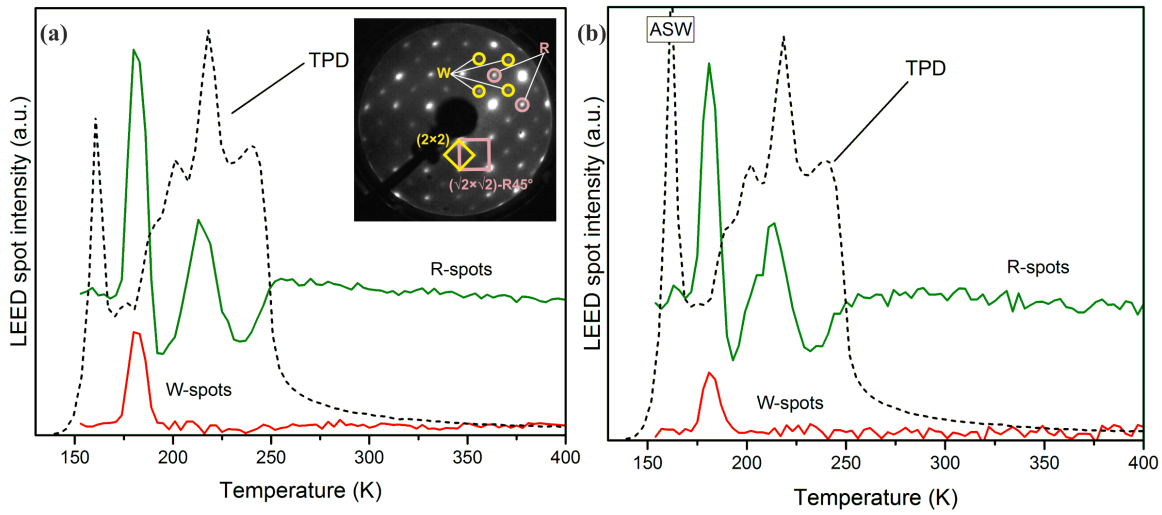

Figure 4.20: Averaged intensity of the selected (circled) diffraction spots taken from the TP LEED movie (at 47 eV) during heating (3 K/s) of the film exposed to (a)1.75L and (b) 2.25L. The corresponding TPD spectra are displayed as dashed line. W- and R-spots are referring to (2 ×2) water ad-layer and ($\sqrt{2} \times \sqrt{2}$)R45° reconstructed surface, respectively. The unit cells are indicated.

To examine the influence of water coverage on the (2 ×2) superstructure in the observed temperature region, TP LEED movies at 25 eV were investigated. A set of D_2O exposures (i.e., 1.25, 1.5, 1.75, 2, 2.5, 4, 5 and 6 L) at 140 K then heated with the same TPD heating ramp 3 K/s. The intensity profile for various exposures is plotted versus temperature in figure 4.21. The results show that the (2 ×2) structure appears at dosages from 1.75 to

5 L water. It shortly appears, for such a narrow temperature range, consistently occurring at all exposures. This makes its observation rather difficult to identify and easy to overlook.

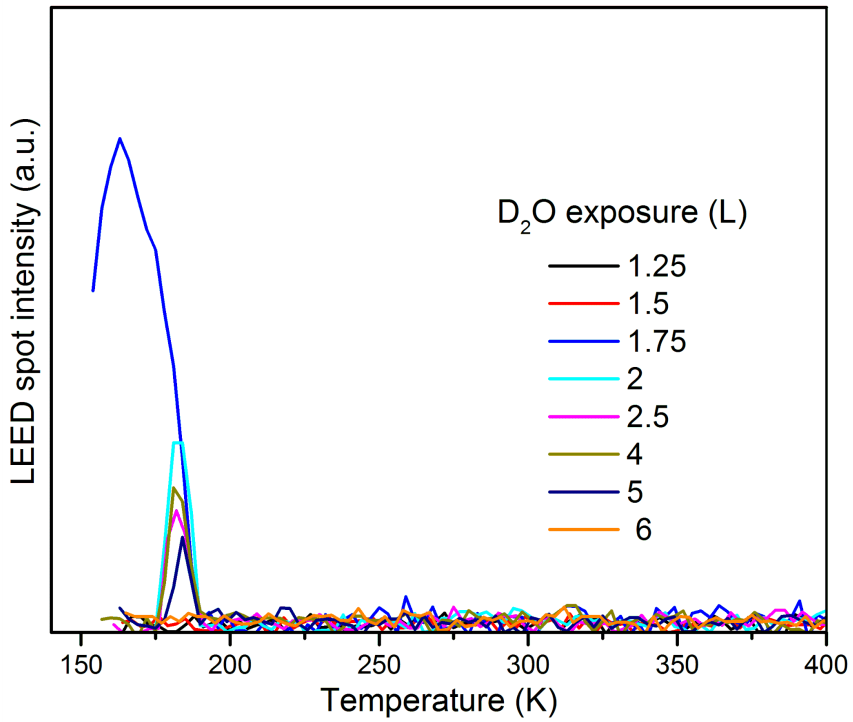

Figure 4.21: Averaged intensity of the (2 ×2) water ad-layer diffraction spots from TP LEED video (E=25 eV) at different exposure (as indicated). The heating rate 3 K/s.

There is no observation of (2×2) structure at 1.25 and 1.5 L exposures, indicating that the needed coverage is not reached yet. Despite the TPD spectrum for 1.5 L indicates that the first "monolayer" water film almost formed.

Obviously, (2×2) spots are strongly detected (intensity) at 1.75 L. The latter is especially important as it is the only coverage that displayed ordered structure at 140 K. It cannot, however, explain the much larger increase in the intensity. This can be related to this specific electron beam energy (25 eV), however, as such behaviour consists of the LEED pattern of 1.75 L water at 140 K (see fig.4.18).

Further increasing of water exposure from 2 to 5 L leads to decreasing (2×2) intensities. At 6 L, the ordered water ad-layer is not observed anymore.

This implies that the structure of the water adlayer is highly sensitive to the coverage. Also it is noticed with the existence of α^* and $\alpha^{'}$ peaks.

More specifically, the Fe_3O_4(001)-(2×2) structure is observed at a coverage of about 8 H_2O/u.c., or 1.2 × 10^{15} H_2O/cm^2, following the calibration in ref.[135]. Meanwhile, Fe_3O_4(111)-(2 ×2) is detected at coverage 5.6 × 10^{14} H_2O/cm^2. Accordingly, the surface coverage on (001) surface is twice (111).

Since we are, in particular, studying the effect of water adsorption on the intensity of the diffraction spots, a blank TP LEED video is required. Therefore, TP LEED movie of clean (001) surface heated from 140 to 400 K by 3 K/s, was also examined. The intensity profile, average values, is illustrated in figure 4.22. Clearly, the intensity is almost constant during the temperature range. This is considered as evidence that the changes were directly related to water adsorption.

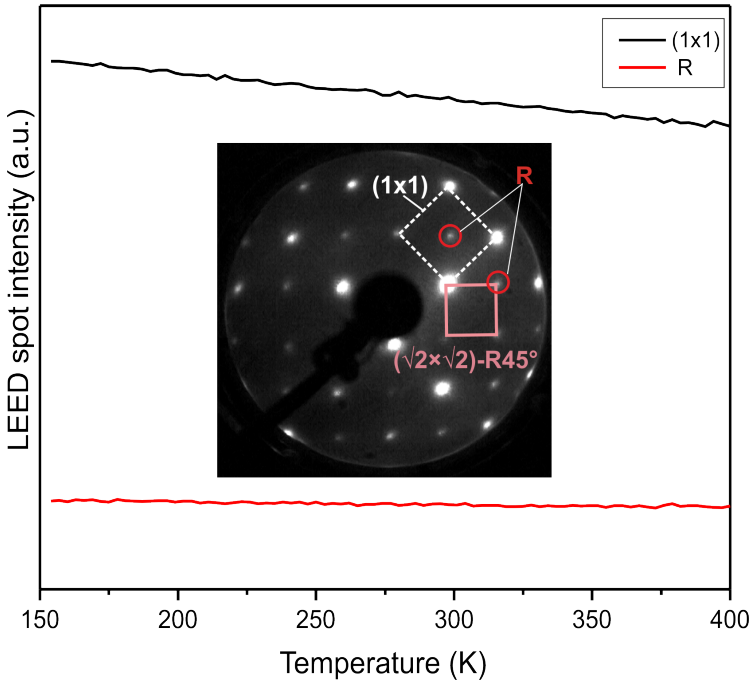

Figure 4.22: Intensity changes as a function of temperature of the detected spots of a clean Fe_3O_4(001)-($\sqrt{2} \times \sqrt{2}$)R45° film through TP-LEED movie (E = 47 eV). Heating rate 3 K/s.

4.3.3 Desorption kinetics

By performing different TPD analysis methods reliable desorption energies and pre-exponential factors can be extracted. For each TPD spectra in figure 4.16, the θ/θ_{max} vs T plots can be obtained by integration the spectra from 140 to 330 K (where all water desorbed), as given in fig. 4.23(a). Inversion analysis of Polanyi-Wigner equation [85] was applied, under the assumption that desorption kinetics are first-order and $\nu = 10^{13}$ s^{-1} is utilized, in order to compare the calculated data with (111) surface. Figure 4.23(b) shows the coverage-dependent desorption energy of water.

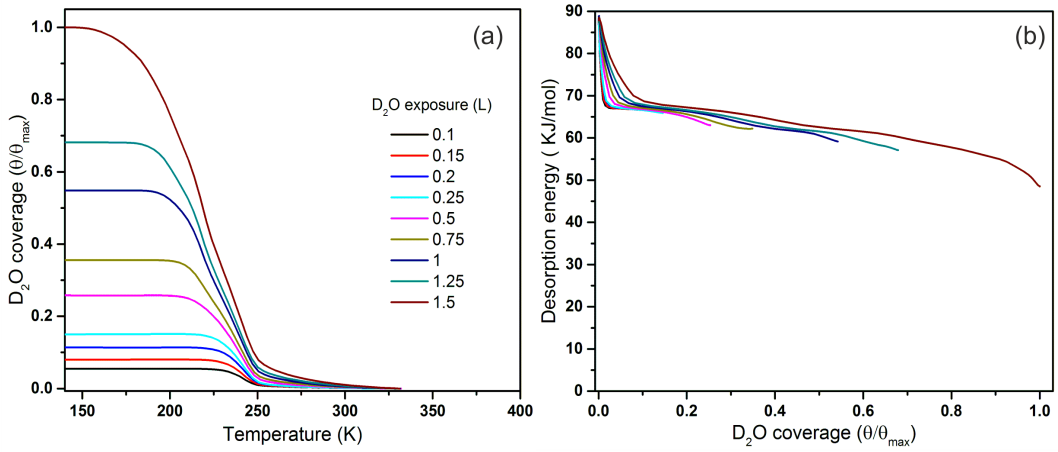

Figure 4.23: (a) D_2O coverage versus temperature plots obtained from TPD spectra. (b) Desorption energy as a function of water coverage obtained by: Inversion analysis of the Polanyi–Wigner equation with $\nu = 10^{13}$ s^{-1}. Water coverage is normalized to the maximum obtained before the ASW peak.

As was observed in fig.4.16, that with increasing water exposure the signal above 250 K continuously grows up due to the limited pumping speed. Therefore the coverage that was shown in fig 4.23 (a) is overestimated. In turn, this causes an artificial shift of curves in figure 4.23 (b).

To correct this, water coverage and desorption energy were recalculated, this time the TPD spectra (fig.4.16) were integrated over temperature range from 140 to 255 K. The corrected plots are displayed in fig. 4.24 (a and b), the new obtained energy curves are coincide and shifted to lower values (about 20 kJ/mol) than previously presented in fig 4.23 (b).

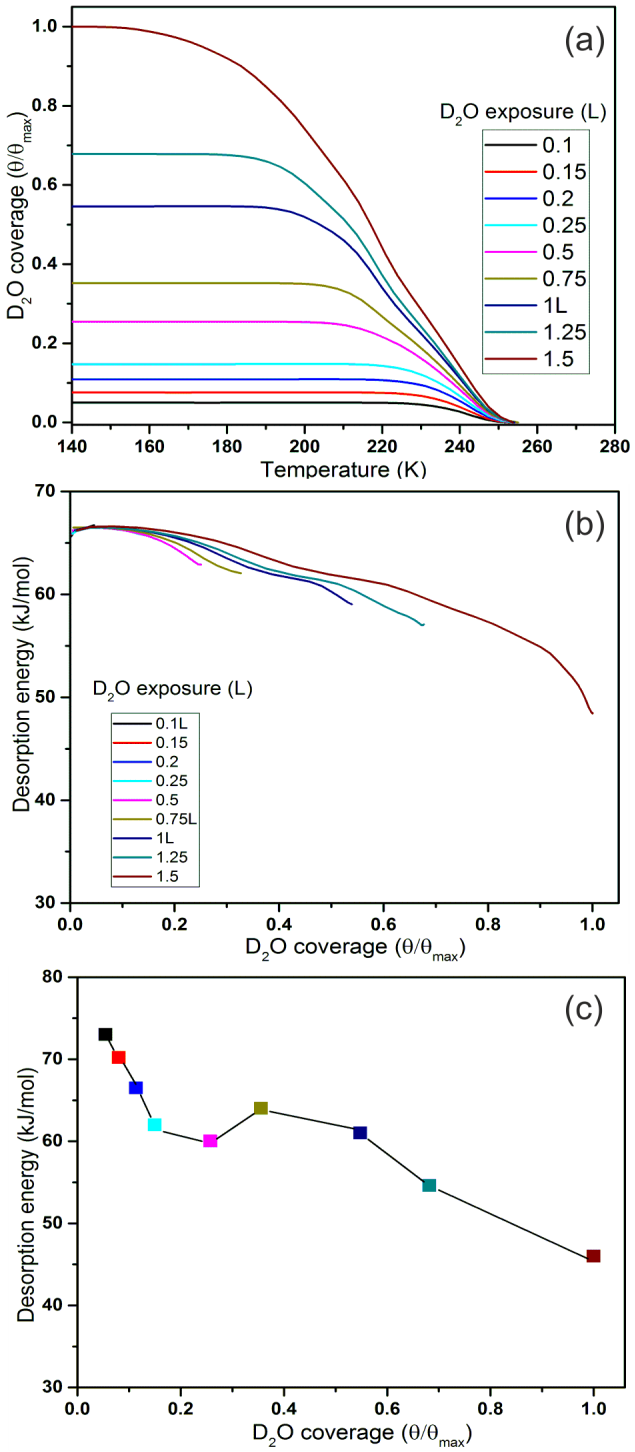

Figure 4.24: (a) D_2O coverage θ/θ_{max} versus temperature obtained from TPD spectra. Desorption energy as a function of water coverage obtained by: (b) Inversion analysis of the Polanyi–Wigner equation with $\nu = 10^{13}$ s^{-1}. (c) "leading edge" analysis. Water coverage is normalized to the maximum obtained before the ASW related peak sets in.

Figure 4.24(b) shows the general behavior of the desorption energy with respect to coverage. The energies values fall in the range of 67 kJ/mol, which then decrease with increasing coverage. Increasing the pre-factor value leads to a shift of all energies towards higher values.

Applying "leading edge" analysis [87], no assumption about ν is needed. The obtained data are displayed in fig.4.24(c) ranging 73 -46 kJ/mol. It should be noted that at 0.75 and 1 L exposures the energy slightly increasing by $\sim$ 4 kJmol (strong binding).

Employing the conventional Redhead analysis of peak maximum[75], reveals variation of the desorption energies from 61 to 45 KJ/mol, for ν= 10^{13} s^{-1}. Table 4.4 summarizes these energy values. Energy values increased by 10.7 kJ/mol using ν= 10^{15} s^{-1}.

Table 4.4: The desorption energy obtained by Redhead analysis of peak maximum and ν= 10^{13} s^{-1}.

	T_m. (K)	desorption energy $kJmol^{-1}$
Fe_3O_4(001)	177 (α')	45
	188 (α^*)	48
	200 (β)	50
	220 (γ)	56
	240 (δ)	61

Upon utilizing HRV method we get a hint about the pre-exponential factor. The initial water coverage was kept constant, at four different exposures, i.e., 0.15, 0.75, 1.25, and 2 L (fig. 4.25 (a-d)). The heating rate was varied from 0.5 to 5 K/s. Knowing that desorption process is followed first order kinetic. The obtained desorption energies and ν, for each individual desorption peak, are illustrated in fig. 4.25 (e-f).

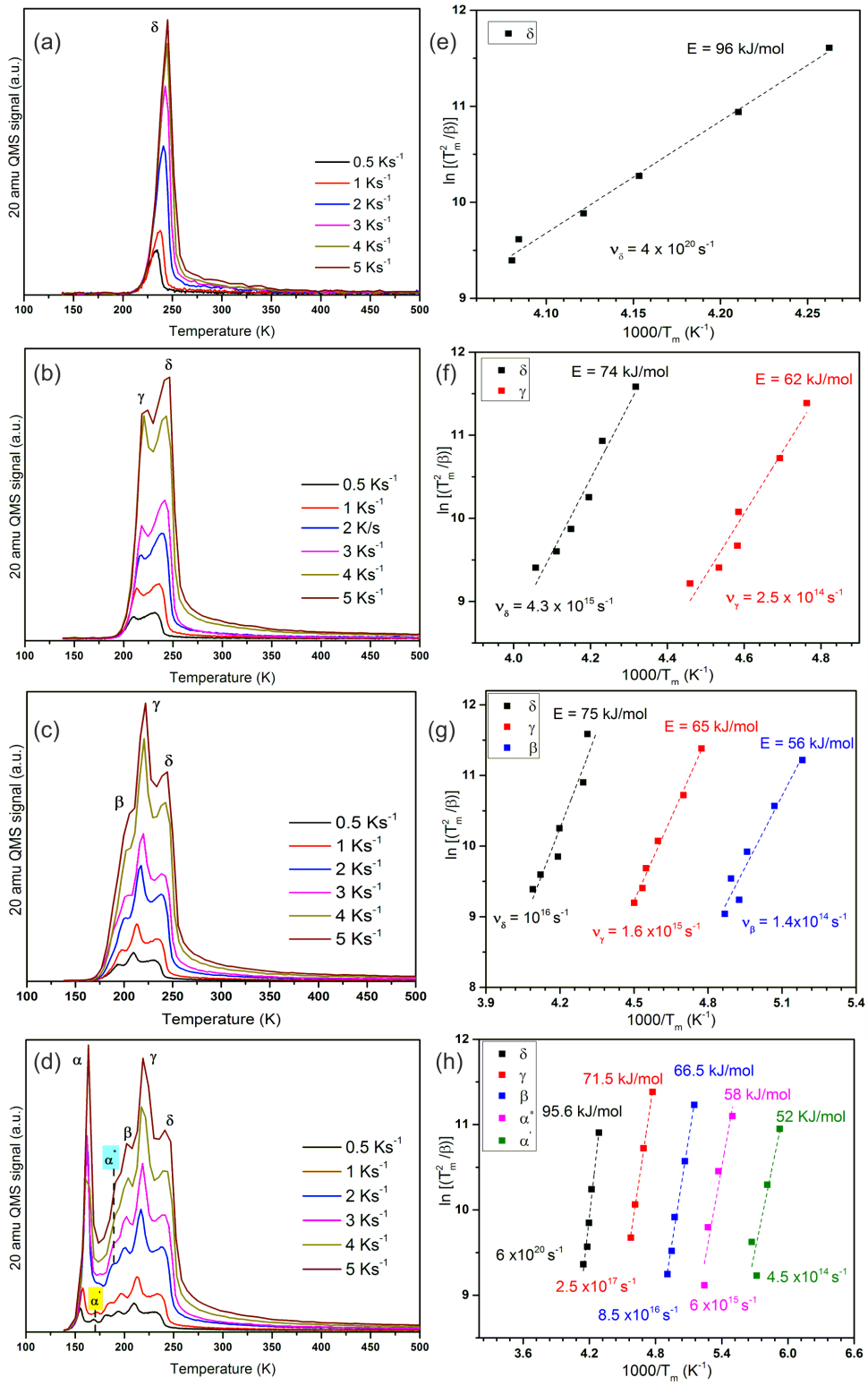

Figure 4.25: TPD spectra of fixed water exposures (a) 0.15, (b) 0.75, (c) 1.25, and (d) 2L at 144 K and different different heating rates. $\ln(T^2{}_m/\beta)$ versus $1/T_m$ plots are in parallel with its corresponding exposures. Both desorption energy (kJ/mol) and ν (s^{-1}), for each desorption peak, are displayed.

Table 4.5 lists the calculated values of desorption energy for different water exposures, as shown in fig.4.25, applying HRV method. As can be seen that the absolute values of E_d and ν (of the same desorption state) are varied with water coverage. Despite the limited number of papers dealing with the analysis of kinetic data using the VHR method from such complex TPD spectra, we still need to understand the origin of variation in E_d and ν values upon increasing coverages.

In principle, the HRV method is strongly dependent on surface coverage. Neglecting the latter condition may lead to an error of several orders of magnitude in the pre-exponential factor values, as noted by Zhdanov et al.,[136, 137] for CO oxidation on Ir(lll). In a further attempt Zhdanov [138] provided an intensive review highlighting the relationship between the experimental and theoretical kinetic parameters for desorption of simple molecules (such as H_2, NO, and CO) on solid surfaces. Briefly, two important points have to be stressed about coverage dependence of pre-exponential factor and activation energy. Firstly, the sticking effect, the higher sticking probability (the adsorbed particles are more bounded to the surface) higher ν value and vice versa. Secondly, with increasing the surface coverage and due to the occurrence of many surfaces processes, such lateral interactions between adsorbed particles (the compensation effect), adsorbate induced changes to the surface, or participation of various types of adsorption site both pre-exponential factor and activation energy are strongly affected. The compensation effect mainly caused a drop in E_d and ν values.

We would like to emphasize that kinetic data, are rather difficult to interpret in details particularly, when several elementary surface processes are involved (e.g., dissociation adsorption, molecular adsorption, associative desorption, diffusion, etc..).[139]

Table 4.5: The desorption energies estimated by HRV method of different water coverage 0.15, 0.75, 1.25, and 2 L on Fe_3O_4(001).

	D_2O exposures (L)			
	0.15	0.75	1.25	2
δ	96	74	75	95.6
γ	–	62	65	71.5
β	–	–	56	66.5
α^*	–	–	–	58
α'	–	–	–	52

On the other hand, the calculated pre-exponential factors (average value of the desorption state over all exposures), are in agreement with the values obtained previously by Meier et.al.[135] despite the fact that each one of us used different analysis method. For comparison, table 4.6 include the data for water adsorption on film (our data using HRV) and single crystal (Ref [135]).

Table 4.6: Summary of the kinetic parameters (desorption energy and pre-exponential factor) using HRV, average values, obtained from our thin film and the data from Ref. [135] for a single crystal.

	Desorption energy $kJmol^{-1}$	Pre-exponential factor s^{-1}	ν s^{-1} Ref. [135]
δ	85 ± 11	$4.7\times10^{17.5\pm2.5}$	$10^{17\pm1}$
γ	66 ± 4	$2.2\times10^{15.5\pm1.5}$	$10^{16\pm1}$
β	61 ± 5	$5\times10^{15\pm1}$	$10^{16\pm1}$
α^*	58	6×10^{15}	- -
α'	52	4.5×10^{14}	$10^{14\pm2}$

Indeed, care should be taken when comparing the absolute values for the desorption energy. For instance, the HRV reveals energies higher than those obtained by Redhead analysis of peak maximum and inversion analysis of the Polanyi–Wigner equation, originate in the difference (small) presumed prefactor value used in latter methods. However, in general, all analysis methods show a decrease in the desorption energy via increasing coverage.

Again, as in the case of (111), further DFT investigation could help us to rationalize our experimental observations, in particularly the LEED results. According to the recent DFT analysis of water adsorption on (001) surface, the following scenario was proposed:[135] isolated water molecules prefer to adsorb intact (E_d= -0.64 eV). Once two (three) molecules meet at the surface they undergo partial dissociation forming dimer (and trimer) species as shown in fig. 4.15. This Partial dissociation makes the interaction with surface metal cations more stronger. Accordingly the formation of a hexagonal ice layer is hindered by the square geometry of Fe_3O_4(001) surface. Thus water species have to follow the underlying surface periodicity forming a ring-like structure (at coverage of 8 H_2O/u.c) suggesting that water bonding to the metal dominates over H-bonding. Figure. 4.26 depicts the DFT based model at 8 H_2O/u.c. The latter coverage is already close to that of a close-packed ice layer, hence, further water adsorption leads to multilayer ice formation. At the highest coverages, where (2×2) ordering is formed, many water molecules coordinated to each other without forming direct bonds to a substrate.

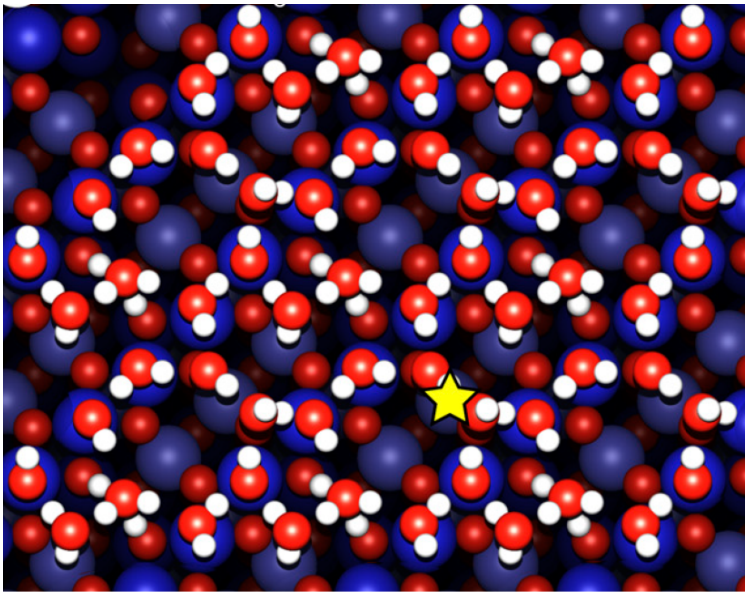

Figure 4.26: The DFT-predicted structure at the highest water coverages (8 H_2O/u.c) before multilayer formation. The yellow star marks the bridge molecules. Reproduced from Ref[135].

Based on this DFT analysis, and bearing in mind that water was experimentally (LEED) observed to be ordered at coverages between mono - and

multilayer (ASW) at a very narrow temperature range, suggesting that ordering is a metastable intermediate when hydrogen bonds begin to dominate over the water-surface interaction.

When it comes to water/oxide interface, there are too many factors involved, all interrelated and may influence each other, such as; the oxide surface imperfection. What kind of surface defect that facilitates water dissociation? The surface geometry, which acts as a template for the ordered water ad-layer. The competitive interaction between water/oxide bonding vs intermolecular H-bonding. Therefore, to generalize a model for water/oxide interface, we need to understand which of these factors are dominate the interface and why.

4.4 Summary

I studied water adsorption on two different facets of magnetite films utilizing TPD, LEEd, TP LEED, and IRAS.

Water adsorption on $Fe_3O_4(111)$ and $Fe_3O_4(001)$-$(\sqrt{2} \times \sqrt{2})R45°$ films is structure sensitive. Both facets display multi-desorption peaks in the TPD profile, however, water interacted more strongly on (111) than (001).

The desorption energies observed in the low coverage regime on the (001) surface are considerably smaller than measured on the (111) surface, 60-70 vs 90-100 kJ/mol, respectively. Generally, all applied TPD analysis methods give a similar picture and reveal that desorption energy decreases with increasing coverage.

Water ad-layer tends to order in (2 ×2) periodicity on both (111) and (001) forming hexagonal and square ice-like structure, respectively. The hexagonal symmetry of $Fe_3O_4(111)$ provides the ordered structure over a wider temperature range (200-250 K) than at (001) (175-187 K).

On (111) plane, the adsorption follows the "classical" model. Initially, the water molecule dissociates to form two surface hydroxyls O_sH and O_wH. The latter anchor the coming water molecule forming a dimer-like complex. Eventually, (2 ×2) long-range ordering hexagonal structure is formed via a hydrogen-bond network which is thermodynamically driven.

While on (001), water prefers to be molecularly adsorbed at first. With increasing coverage, water dimer and trimer are formed vai partial dissociation.

The latter reinforces the interaction with the surface metal cations, forcing ice layer to mimic the square symmetry of (001) plane. At very highest coverages, the hydrogen bonds are dominating over the water-surface interaction, hence, (2 $\times$2) structure is metastable and intermediate.

Note, that it has not been possible so far to quantify the water coverage at the maximum LEED intensity of water. It would be interesting to see whether the ordering of water ad-layer may influence the reactivity of iron oxides surfaces. To our knowledge, the reactivity at such conditions has not been studied.

Chapter 5

CO_2 Adsorption on Fe_3O_4

5.1 Introduction

Several economical and environmental aspects and various applications are the motivation for studying interactions of carbon dioxide. The greenhouse effect and global warming are mainly caused by an excess of CO_2 which absorbs energy from the sun and earth and "traps" it near the Earth's surface, thereby resulting in significant climate change. Therefore, it is important to limit the emission of carbon dioxide and utilize it in other applications as an alternative solution.[140] In addition, CO_2 is involved in many catalysis and energy applications; e.g., WGS, RWGS, the Bosch reaction, the Fischer–Tropsch reaction and methanol synthesis. However, the thermodynamic stability of carbon dioxide, with an enthalpy of -393.5 kJ/mol, hinders its activation. Generally, adding an extra electron to carbon dioxide (i.e., transfer from the surface) turns it into CO_2^- molecular anion where the bond angle changes from 180° to 135°. This bent $CO_2^{-\delta}$ exhibits higher reactivity than the linear arrangement. Thus, the catalytic transformation of CO_2 into more valuable products has become an interesting topic for research. A comprehensive review on the interaction of CO_2 on metals and oxides surfaces are presented in references [141–143].

As far as the interaction of CO_2 on magnetite surface is concerned, we will only highlight the major studies that have been conducted in this topic. Udovic et al.,[95] studied CO_2 adsorption at 150 K on poorly defined magnetite films. The latter are prepared in UHV by treatment of polycrystaline iron foil.

The TPD results revealed two peaks at 200 K and 400 K, which were assigned to monodentate (50-60 $kJmol^{-1}$) and bidentate (60-120 $kJmol^{-1}$) species, respectively.

Interestingly, Chuni-lei et al.,[144] reported that complete decomposition of carbon dioxide into carbon is accomplished if magnetite (powder) has excess cation content. However, $Na/Fe_3O_4(111)$-(1×1) surface was reported to be inert towards CO_2 as illustrated by the synchrotron-radiation based core-level studies and valence band photoemission spectroscopy and LEED.[145]

Another observation of decomposition of CO_2 into elemental carbon has been reported on magnetite powder, via electron donation from oxygen-deficient site of magnetite to carbon of CO_2.[146]

Based on DFT calculations, the adsorption of CO_2 on $Fe_3O_4(111)$, which exposes two different terminations Fe_{tet1}-and Fe_{oct2}[147], was examined. The study revealed that Fe_{oct2} is chemically more active because CO_2 accepted electrons from Fe_{oct2}, forming a covalent bond between carbon atom and surface oxygen atom.

Santos-Carballal et al.,[148, 149] simulated the vibrational frequencies and adsorption energy of adsorption of CO_2 on $Fe_3O_4(111)$ and (001) based on DFT. However, surface defects and environmental species (contamination) were not considered in the simulation. Also, the (111) plane was assumed to be Fe_{oct2} terminated. The calculations indicated that CO_2 interacts strongly with both surfaces, where it bends and forms a highly stable carbonate group and the most favorable interaction was on (111) surface having adsorption energy of 1.37 eV.

The TPD, UPS, XPS and STM were employed to investigate CO_2 adsorption on single crystal $Fe_3O_4(001)$ [150]. The data revealed that CO_2 weakly adsorbs on regular sites Fe^{3+}. The proposed mechanism is as follows: initially adsorption of CO_2 takes place on the defect sites of Fe^{2+}, as evidenced by very small desorption peaks at 125 K, 165 K and 195 K. This was followed by further adsorption of CO_2 on regular sites $\sim$ 110 K, eventually second monolayer and multilayers (zero-order kinetics).[150] These results are specifically important to us as we will compare their TPD on (001) single crystal with our film.

Below I compare the TPD results of CO_2 adsorption on both facets (111)

and (001) films. Moreover, the critical role of water and CO adsorption from the UHV background on the interaction of CO_2 will be highlighted. Finally, the activation of CO_2 by modifying the surface by water will also be examined. The results of this study are partially published in reference [151].

5.2 CO_2 adsorption on Fe_3O_4(111) films

5.2.1 Adsorption on pristine surface

As previously observed (in Chapter 3), the Fe_3O_4(111) surface is very sensitive to traces of water and CO in the residual gas. With this in mind, the signals of these gases were also monitored during investigation of CO_2 adsorption. Precautions were also taken to minimize parasitic adsorption of residual water, and a cold trap was used for CO_2 gas.

At 90 K, the Fe_3O_4(111) surface was exposed to various dosages of CO_2 in the range of 0.01-1 L. Figure 5.1 shows TPD spectra while heating the surface up to 600 K with a heating ramp of 3 K/s. The CO_2 profile displays a desorption peak at ∼150 K at low exposure that shifts to lower temperature ∼100 K when the exposure is increased. This low-temperature CO_2 peak has a sharp descending edge indicating that this signal represents solely a cutoff of the desorption signal, having a maximum at a lower temperature than 90 K. The latter observation can henceforth be assigned to weakly bonded or physisorbed CO_2. However, another desorption peaks, in the range of 320-300 K, begins to appear with increasing CO_2 exposure.

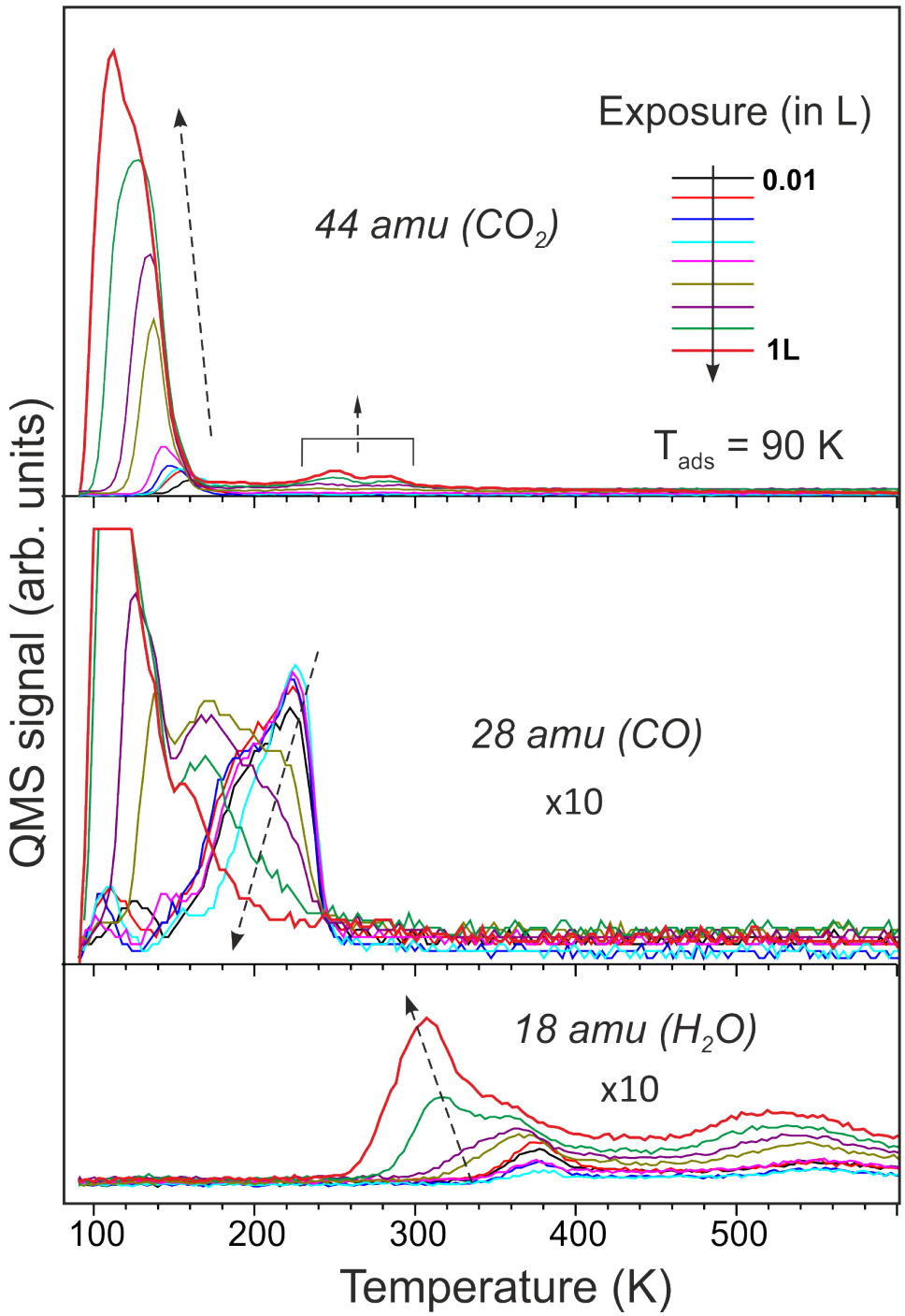

Figure 5.1: TPD profile of CO_2 (44 amu), CO (28 amu), and H_2O (18 amu) QMS signals obtained at increasing dosage of CO_2 at 90 K as indicated. Spectral evolution is highlighted by arrows to guide the eye. CO signals at temperatures below 150 K appearing at high exposures are assigned to CO_2 the fragmentation pattern. The surface is heated to 600 K using 3 K/s. Both CO and water are from the residual gases from the UHV background

Concerning the residual water and CO, both show a change in the responses with increasing CO_2 dosage. Water signal develops gradually with CO_2, resembling those spectra obtained in water adsorption experiments (see fig. 4.2). Significantly the appearance of high-temperature CO_2 peaks (i.e. 300-320 K region) are observed with increasing participation of residual water.

In the case of residual CO, the spectra exhibit a CO desorption peak at ∼235 K, i. e. in the γ-state (i.e., nearly the same peak position and amount) as in TPD data obtained upon adsorption of pure CO. It should be noted that the desorption signal below 150 K simply follows the cracking pattern of CO_2 in the QMS.

In order to minimize the CO_2 physisorption peak at low temperature, adsorption experiments were carried out at 140 K, i.e. at the descending edge of weakly bonded CO_2. TPD spectra are acquired over a wider range of CO_2 initial exposures 1-100 L and are summarized in figure 5.2.

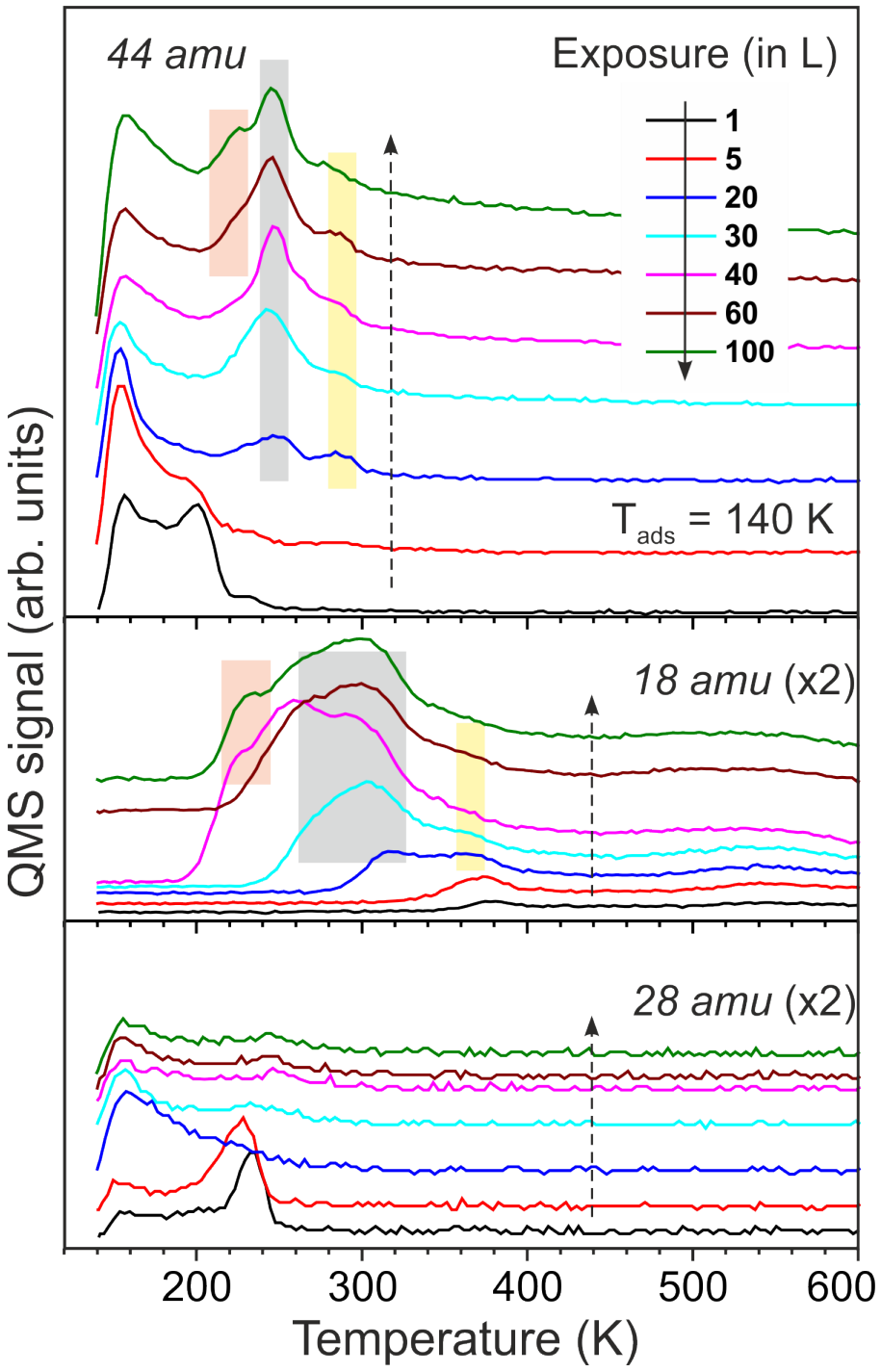

Figure 5.2: CO_2 (44 amu), CO (28 anu), and H_2O (18 amu) QMS signals monitored upon increasing CO_2 exposures (as indicated) at 140 K. The spectra are offset for clarity. Colored shaded areas highlight apparent correlation between CO_2 and H_2O desorption peaks on "water-contaminated" surfaces. Both CO and water signals participate from UHV background.

CO_2 signals exhibit several desorption states that populate with increasing exposures. At 1 and 5 L, a CO_2 peak appears at 200 K, at which the detected water is almost negligible, therefore we refer to this as "water-free" conditions. In contrast, the CO profile reveals a peak at ∼235 K, which later will be verified through a further experiment.

Much emphasis is placed here on the detailed evaluation of the TPD spectra in fig. 5.2 in order to get insights and an understanding the interference of water and CO (UHV residual gases) in CO_2 adsorption process.

Obviously, the spectra of CO_2 at high exposures > 5 L are accompanied by quite substantial desorption of water, suggesting a certain kind of correlation, as highlighted by the shaded areas in fig. 5.2, using the same color code to guide the eye.

The desorption profile of water at exposures above 30 L of CO_2 suggested it is about 1 ML. The latter statement is based on our quantification of water on (111) surfaces in Chapter 4. Such an amount of water (1 ML) suggests that its adsorption takes place on the regular $Fe_3O_4(111)$ sites as well.

It is important to note that, as the surface of $Fe_3O_4(111)$ is "water-free", CO_2 desorbs at ∼200 K. In the presence of more water (residual), CO_2 becomes more strongly bonded and therefore desorbs at a higher temperature, resulting in multiple desorption peaks of CO_2 centered at ∼260 K. This may be indicative of individual CO_2 interaction with different water species on the $Fe_3O_4(111)$ surface. This may raise the question of the origin of the increasing water signal on increasing exposure to CO_2. We need to take account of the fact that we are increasing CO_2 exposure by increasing dosage time. Accordingly, residual water molecules which, having much higher adsorption energy, have more time to react with the surface and dissociate, ultimately increasing the water desorption signal in TPD.

Turning back to the observed CO peak at 230 K (fig. 5.1 and fig. 5.2), it may be wondered whether CO_2 undergoes a dissociation process. In order to verify this possibility, adsorption of isotopically labeled CO_2^{18} on the same film was conducted. The appearance of CO^{18} (30 amu) is the expected product of CO_2^{18} (48 amu) dissociation.

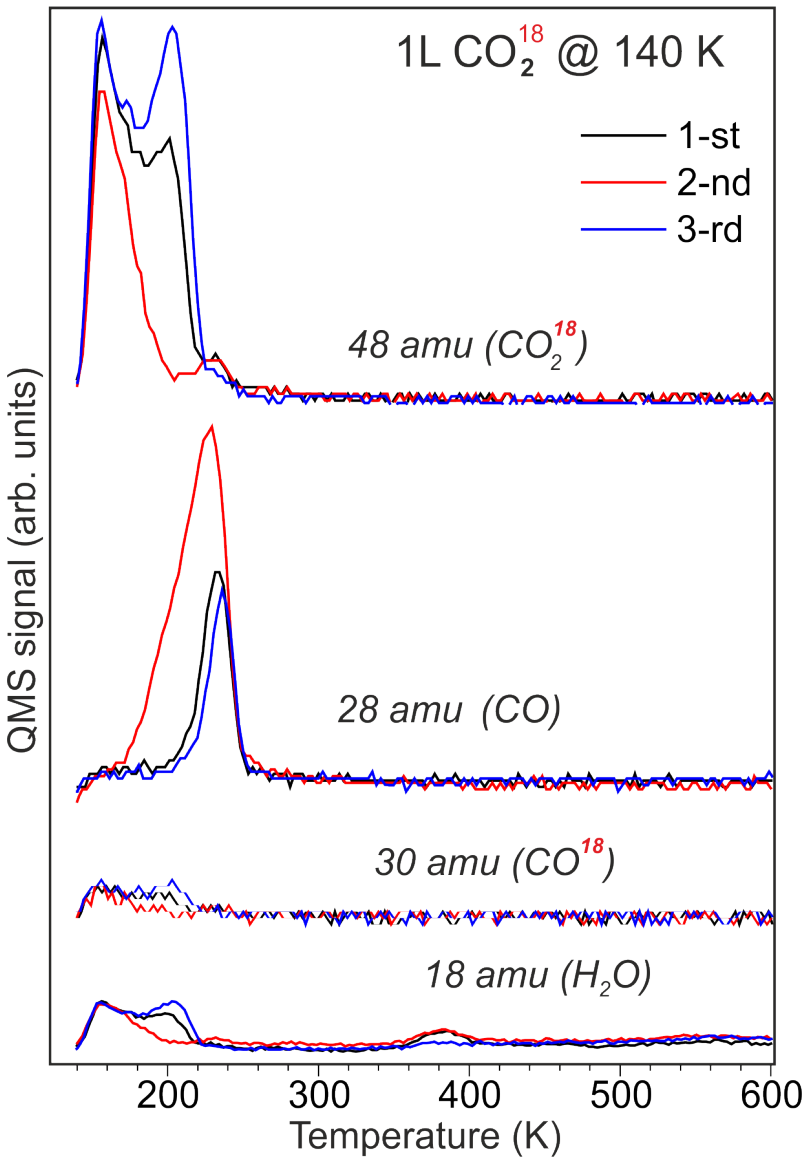

Figure 5.3: CO_2^{18} (48 amu), CO^{18} (30 amu), CO (28 anu), and H_2O (18 amu) signals collected during the three sequential TPD measurements (as indicated) following 1 L CO_2^{18} adsorption at 140 K. TPD measurements were taken at a heating rate of 3 K/s.

Three sequential runs of a constant coverage 1 L CO_2^{18} (48 amu) at 140 K were recorded. Figure 5.3 shows the obtained TPD spectra. The absence of any traces of CO^{18} (30 amu) indicates that the dissociation does not occur.

On the other hand, "normal" CO^{16} (28 amu) was observed similarly to the case of CO_2^{16} (44 amu) adsorption. The latter observation indicates that

CO originates from the UHV background and not from CO_2 dissociation or contamination. The signals of 30 and 18 amu below 220 K imitate the CO_2 signal, therefore they originate from the cracking pattern.

Attention should also be further directed towards relationships between intensities of desorption signals of CO_2 (at 200 K), CO (at 235 K), and H_2O (tiny signal at 380 K): (i) the inverse correlation between CO_2 signal and CO, whereas the water traces coincide (compare black and red curves); (ii) the CO_2 signal inversely correlates with the signal of water, whereas the adventitious CO signals are equal (compare black and blue curves). These correlations between CO_2, CO, and water, suggests that all of them are competing for the same adsorption sites.

According to previous studies [89, 115], CO and water are most strongly bound to defect sites. Besides, the low intensity of the CO_2 signal at 200 K, we may, therefore, conclude that CO_2 chemisorption on the clean $Fe_3O_4(111)$ surface most likely occurs on defect sites. However, CO and water react more strongly on these sites, hence they may block CO_2 adsorption.

5.2.2 Adsorption on water precovered surface

An important achievement in the quest for CO_2 adsorption on water precovered $Fe_3O_4(111)$ surface is a better understanding of what really happens on the surface when water is purposely introduced. To investigate further, TPD data were collected after adsorption of 1 L CO_2 on the surface first exposed to water at 140 K and heating at a rate of 3 K/s. At pre-covering the surface with 0.1 L D_2O both signals are presented in figure 5.4 (black curve). It appears that CO_2 desorption takes place at 240 K, which resembles the spectra obtained on the pristine surface at dosages above ∼30 L. The latter observation proves that water species (either from residual UHV gases or purposely pre-adsorb) have an enhancement effect, strongly binding, on CO_2 adsorption.

However, in the case of the pre-adsorption of 1 L D_2O (fig.5.4 (red curve)), the CO_2 signal only rises by a factor of ∼3, which is certainly not proportional to the water coverage which increases by a factor of ∼10. The latter finding may be explained as follows: At this coverage (∼2 ML) the entire surface is saturated by water species, binding each other and acting as isolation layer between (111) and CO_2. In other words, if the CO_2 adsorbs on the regular

sites it is to be expected that its signal will disappear when the surface is pre-covered by 1 L water (because water will completely block them), which is not the case. This again coincidences with that CO_2 interacts with (particular) water species. Otherwise a strong inhibiting effect of the water ad-layer to be expected.

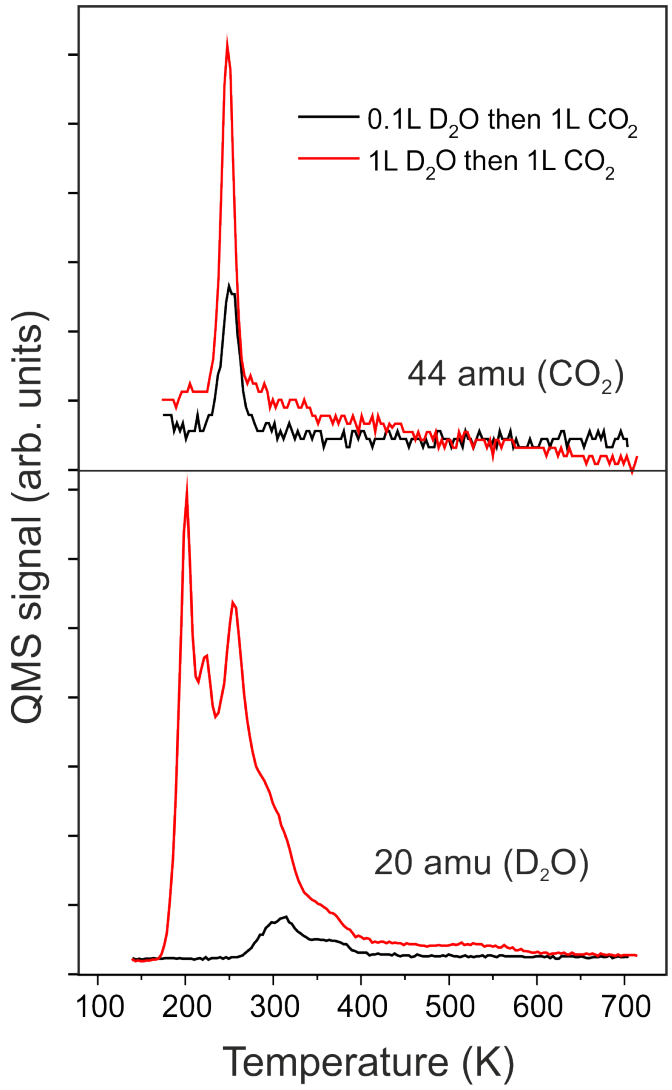

Figure 5.4: CO_2 and D_2O traces in TPD spectra obtained after 1 L CO_2 was dosed to the surface first pre-treated with 0.1 L (black curve) and 1 L (red curve) of D_2O at 140 K.

Remarkably, the water TPD profiles in the coadsorption experiments (fig. 5.4) are almost identical to those previously observed in Chapter 4, for pure

water adsorption, see fig.4.2.

It would be useful to put everything together and see what happens. CO_2 molecules weakly adsorb on the regular $Fe_3O_4(111)$ surface sites having desorption peak below 100 K. While the peak at $\sim$ 200 K reveals adsorption on defects. No CO_2 dissociation is detected. Precovering the surface with water species increases the CO_2 binding strength and thus desorbs at $\sim$ 250 K.

These results have been corroborated by IRAS investigation; all details are in our recent work.[151] The results suggest that surface hydroxyls have a crucial role in CO_2 adsorption on regular (Fe_{tet1}) tetrahedrally terminated magnetite surface, hence leading to the formation of bicarbonates species on the surface. The formation of bicarbonate (HCO_3^-) was also detected on the $TiO_2(110)$ film surface, which desorbed as water and CO_2.[152]

Before we move on, we would like to stress that, because of different kinds of bonds that may be formed between CO_2 (either through carbon or oxygen or both) and water species that exist on (111) surface, various geometry bicarbonates species may be formed. Thus the desorption of the latter species displays several TPD peaks as shown in fig. 5.2. Theoretical models, in turn, may provide validation of our hypothesis. It is therefore desirable for rationalizing our TPD data.

5.3 CO_2 Adsorption on $Fe_3O_4(001)$ films

5.3.1 Adsorption on pristine surface

As a continuation to our studies of CO_2 adsorption on $Fe_3O_4(111)$, we now investigate the adsorption behavior of CO_2 in the (001) plane. To be able to compare the adsorption behaviors of CO_2, the same procedure was followed as for $Fe_3O_4(111)$.

The adsorption of CO_2 on $Fe_3O_4(001)$ was evaluated at 90 K from lower to higher exposure ranging from 0.01 L to 1 L as indicated in Fig. 5.5. It can be seen that CO_2 is desorbed via a sharp desorption peak at $\sim$110 K at all exposures. This desorption peak intensity increases with an increase in the exposure, and the all spectra have a sharp descending edge which implies that the peak maximum is at a lower temperature than the adsorption temperature.

The presence and influence of residual gases CO and H_2O were also monitored during the TPD measurement, see Fig. 5.5. It can be seen that CO is weakly desorbed and the TPD spectra follow a fragmentation pattern of CO_2. On the other hand, water shows a desorption feature at around 220-320 K, although neither CO nor H_2O gases exhibited any influence on the desorption of CO_2. This behavior is in contrast to our observation of CO_2 adsorption on $Fe_3O_4(111)$.

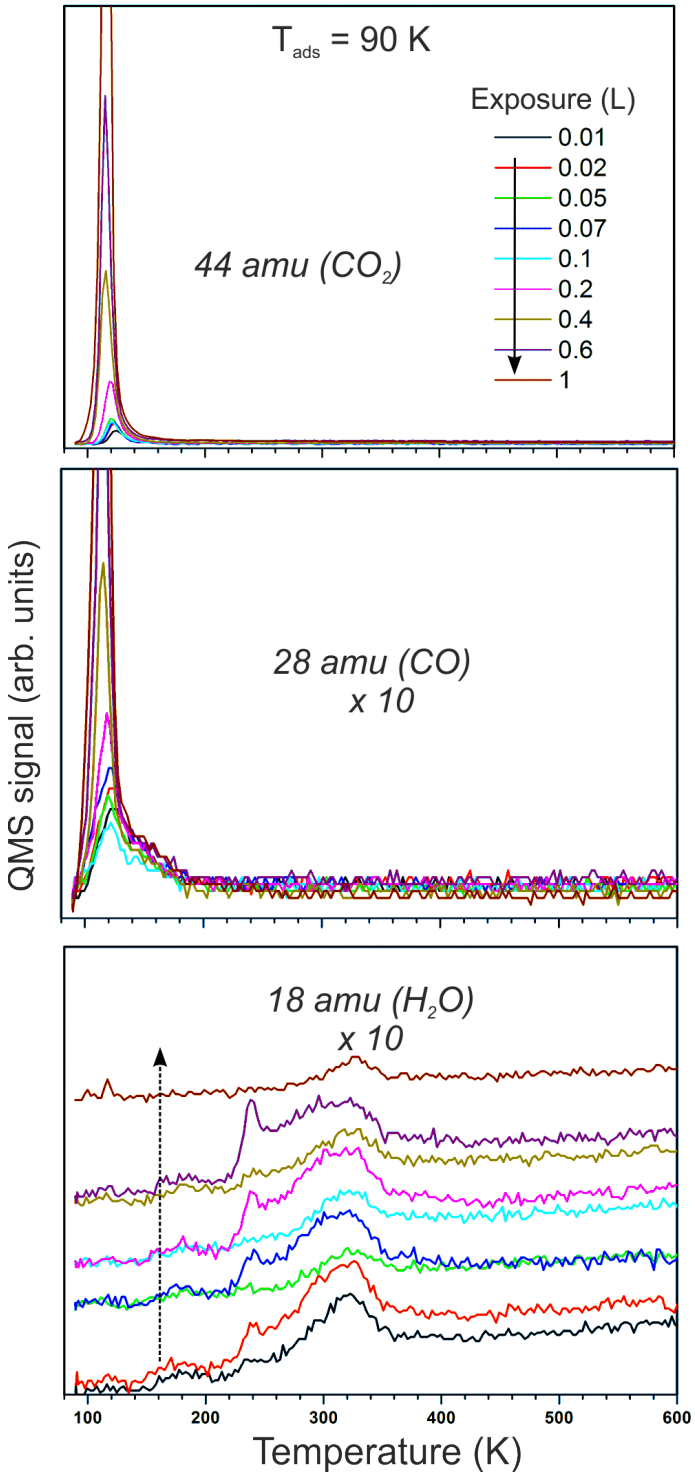

Figure 5.5: CO_2 (44 amu), CO (28 amu), and H_2O (18 amu) QMS signals recorded from $Fe_3O_4(001)$ after increasing dosage of CO_2 at 90 K as indicated. Both CO and H_2O are residual gases monitored during CO_2 desorption. CO signals are assigned to the CO_2 cracking pattern. H_2O signals are offset for clarity. The heating rate is 3 K/s.

To further investigate the adsorption behavior at higher temperature and more exposure, we studied the adsorption at 140 K with exposure ranging from 1 L to 200 L. Figure 5.6 displays the desorption profile of CO_2 along with the residual gases (CO and H_2O) during heating with heating rate 3 K/s. The desorption of CO_2 for all exposures appears at 160 K with a sharp ascending peak which indicates that it is a tail of the desorption peak at lower temperature. The residual CO gas does not show any additional features and it follows the CO_2 profile, as expected for a cracking pattern. Water shows a desorption peak at 240 K as observed in fig 4.16 (Chapter.4), however, with a broad peak over 300 K.

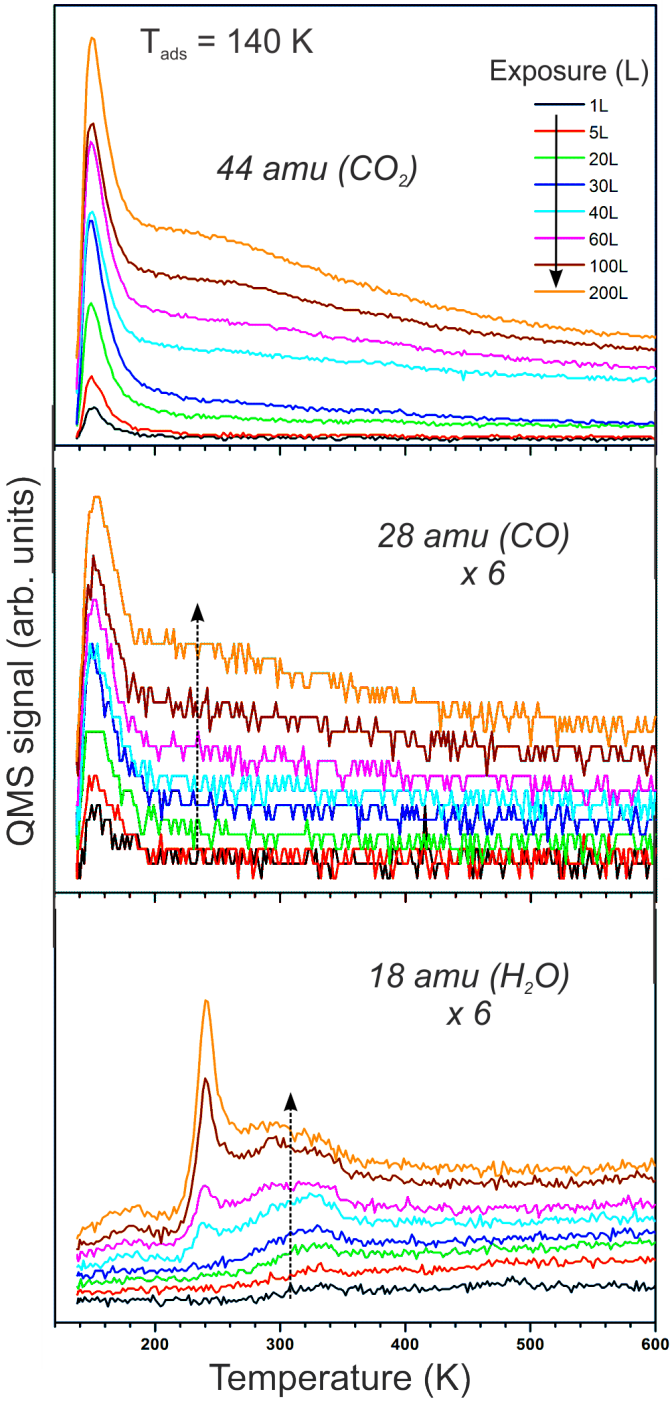

Figure 5.6: CO_2 (44 amu) QMS signal recorded at increasing exposures of CO_2 (as indicated) on Fe_3O_4(001) at 140 K. The signals of residual gases CO (28 amu), and H_2O (18 amu) are monitored upon heating with a linear ramp 3 K/s. The spectra are offset for clarity.

From all the above TPD results, we conclude that CO_2 is weakly bound at the (001) plane of Fe_3O_4 having a desorption maximum at lower temperature than our TPD experiments. These results are in good agreement with the results obtained in Ref [150].

5.3.2 Adsorption on water precovered surface

To understand the adsorption behavior of CO_2 in the presence of H_2O, we studied the CO_2 adsorption on Fe_3O_4(001) precovered with D_2O (same exposure as for (111) facet).

Figure 5.7 shows the TPD spectra for CO_2 (1 L) adsorption of two exposures of D_2O (0.1 and 1 L). Besides the CO_2 desorption peak at 150 K, no other desorption peak is observed at low water exposure (0.1 L). However, at 1 L water exposure, a sharp CO_2 desorption peak at $\sim$ 340 K is observed. This peak appears at a much higher temperature in the (001) plane than in the (111) plane (250 K). It seems that CO_2 adsorption on Fe_3O_4(001) is also water-dependent, hence various amounts of D_2O were further investigated and represented in figure 5.8.

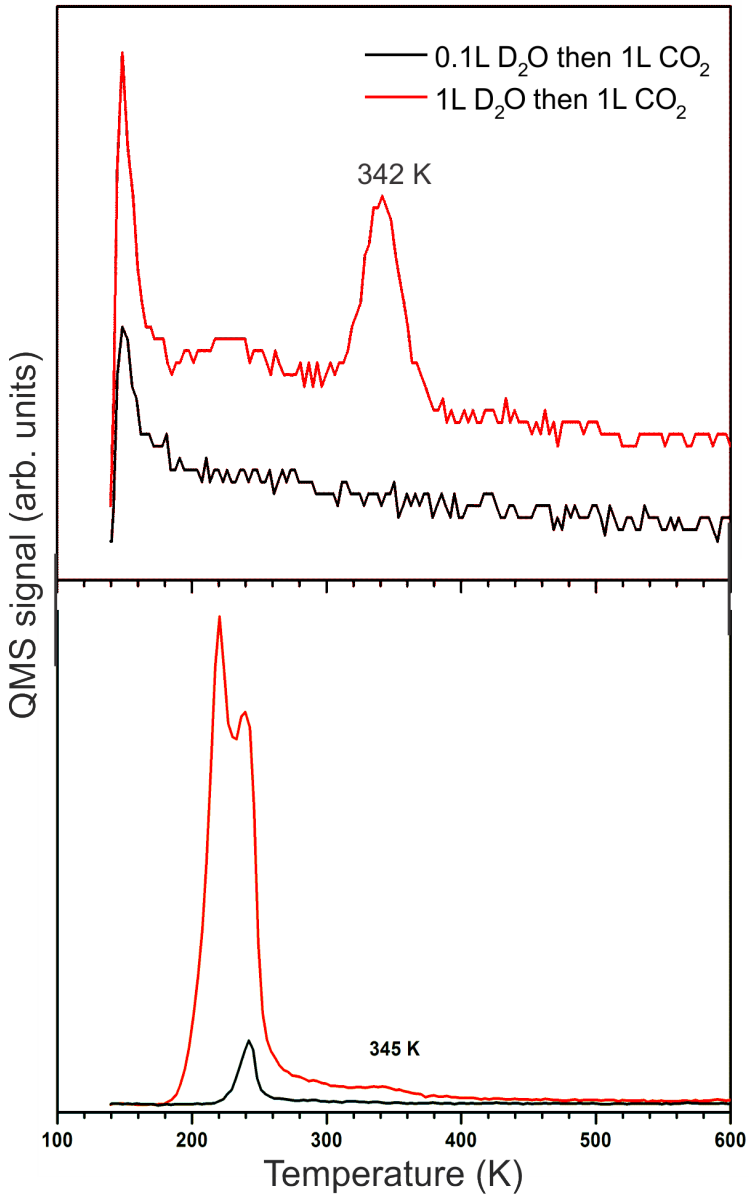

Figure 5.7: CO_2 and D_2O traces in TPD spectra recorded after 1 L CO_2 was dosed to the $Fe_3O_4(001)$ surface first pre-exposed to 0.1 L (black curve) and 1 L (red curve) of D_2O at 140 K. The TPD spectra obtained for a heating rate of 3 K/s.

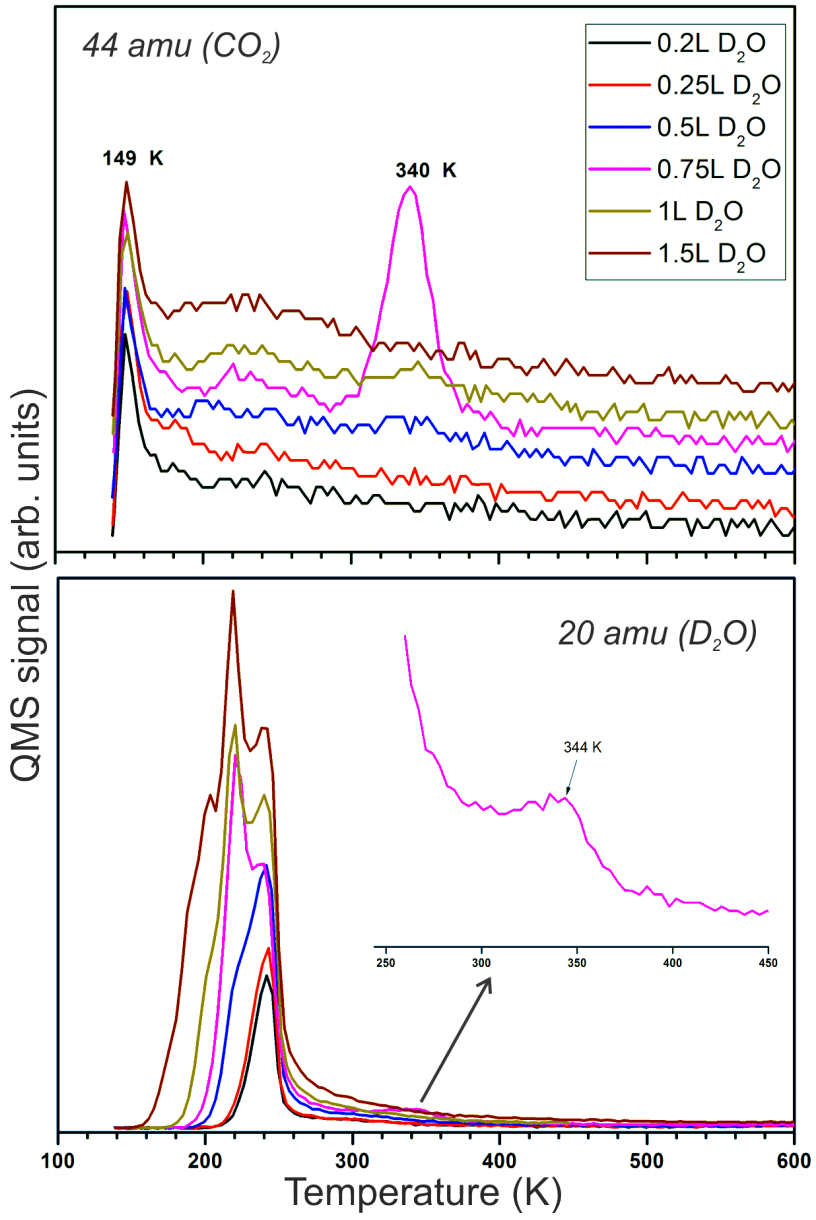

Figure 5.8: CO_2 and D_2O traces in TPD spectra recorded after 1 L CO_2 was dosed to Fe_3O_4(001) surface first pre-exposed to D_2O at 140 K. D_2O exposures are indicated and the inset zooms in 0.75 L D_2O signal.

The TPD spectra were recorded after pre-treating the (001) surface with varying amounts of D_2O ranging from 0.2 to 1.5 L and then dosing a constant exposure of 1 L CO_2. Figure 5.8 illustrates the desorption profile of CO_2 and D_2O. The desorption tail of CO_2 (at <150 K) appears in all the exposures of D_2O, however, we observed a strong desorption peak of CO_2 at 340 K if the

surface is pre-treated with 0.75 L D_2O. The D_2O desorption profile was further evaluated and compared with that of water TPD (see fig. 4.16).

As indicated in fig.5.8, the range of D_2O exposures needed to observe the CO_2 peak at 340 K is rather narrow. To investigate this effect further, D_2O exposures were varied in the range of 0.6 - 1 L as displayed in fig.5.9. Interestingly, the D_2O shows similar TPD profiles as in Chapter 4 (fig. 4.16) for pure water adsorption.

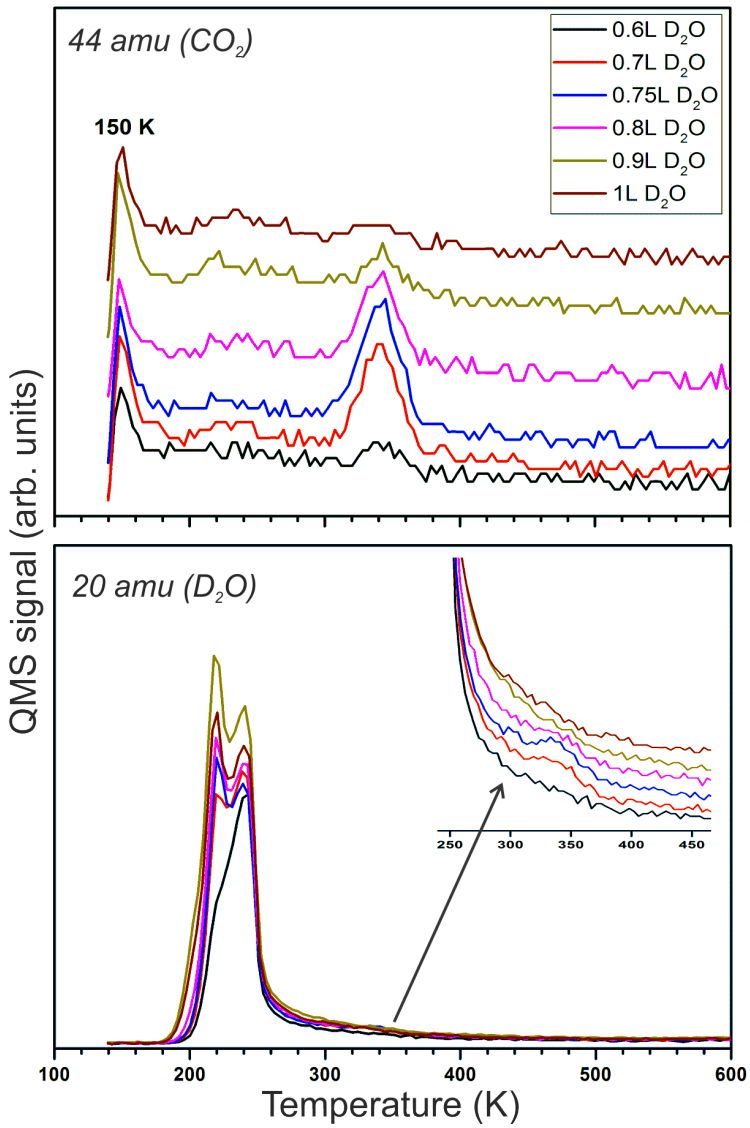

Figure 5.9: CO_2 and D_2O signals in TPD spectra recorded after 1 L CO_2 was dosed to $Fe_3O_4(001)$ surface first pre-exposed to different exposures of D_2O (as indicated) at 140 K. The spectra for D_2O signal are zoomed up in the inset.

The TPD profile of the CO_2 signal shows two peaks. The desorption peak at 150 K, at all exposures, is a tail of the low temperature peak, while, the desorption peak at 340 K shows an increase in the peak intensity from 0.6 L till 0.75 L, after which it decreases.

The CO_2 peak intensity has a maximum when the surface was pre-treated to 0.75 L D_2O. The TPD profile of the D_2O signal (inset of fig.5.9) reveals the presence of a very tiny peak at $\sim$ 340 K. Therefore, the integrated area under this peak is plotted in figure 5.10 for both CO_2 and D_2O signals. It appears that both signals coincide, suggesting that they belong to the same species.

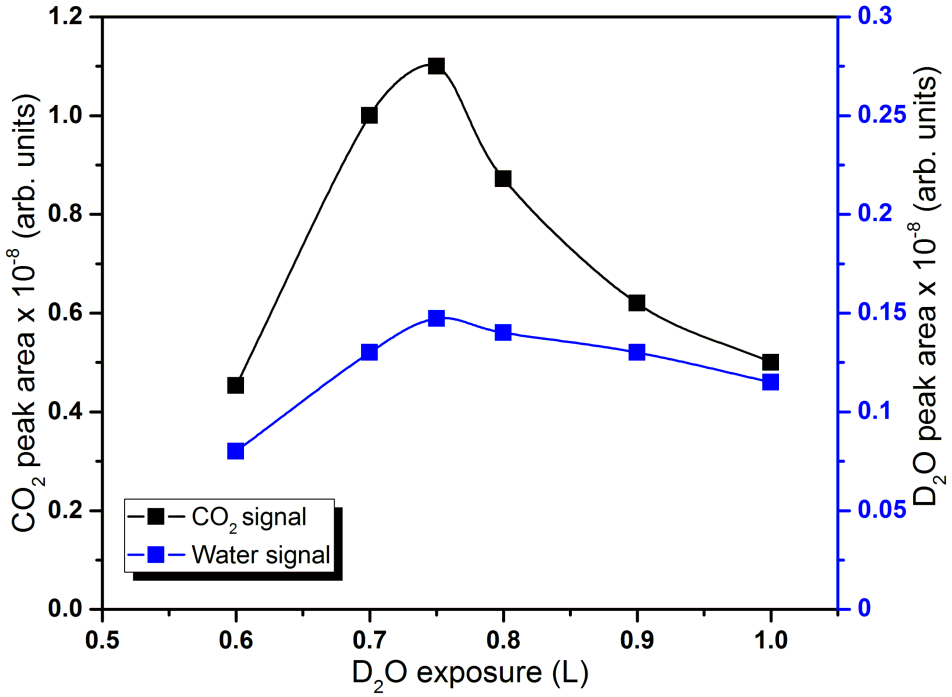

Figure 5.10: Integral of the peak at 344 K, for both CO_2 and D_2O signals (in arb. units), as a function of D_2O exposures.

The water desorption peak at $\sim$340 K cannot be assigned to pure water desorption (e.g. from the defect sites) as it correlates with CO_2, and is missing in pure D_2O adsorption experiments. Therefore, we conclude that D_2O is a result of decomposition of bicarbonate species.

From the TPD perspective, it can be speculated that at a certain exposure, water forms certain species (geometries) which are strongly bound to

the (001) surface in the presence of CO_2 and vice versa. Nevertheless, there is also a possibility that, upon desorption, there might be a change in the surface structure, e.g., creation of defect sites during TPD runs. To assess this hypothesis, we performed the experiments as in fig.5.9 by exposing the surface to 0.6 and 1 L D_2O and vice-versa several times (spectra not shown). No change was observed in the TPD profiles suggesting that the surface structure does not change upon adsorption processes.

This raises the question of why this effect (CO_2 and D_2O desorption at 340 K) is observed at particular D_2O exposures (coverage). In this respect, we note that the desorption energy of pure water calculated by "leading edge" analysis (fig. 4.24(c)) shows some local peculiarity in the energy versus coverage plot such that E_{de} slightly increases at this coverage regime (0.75 and 1 L). On the other hand, E_{de} decreases with increasing coverage on average.

Knowing that 0.75 L D_2O is the maximum exposure for production of strongly bound CO_2 the reversibility of the co-adsorption process was examined in another set of experiments, i. e. by first pre-treating the surface with CO_2 and then exposing to D_2O.

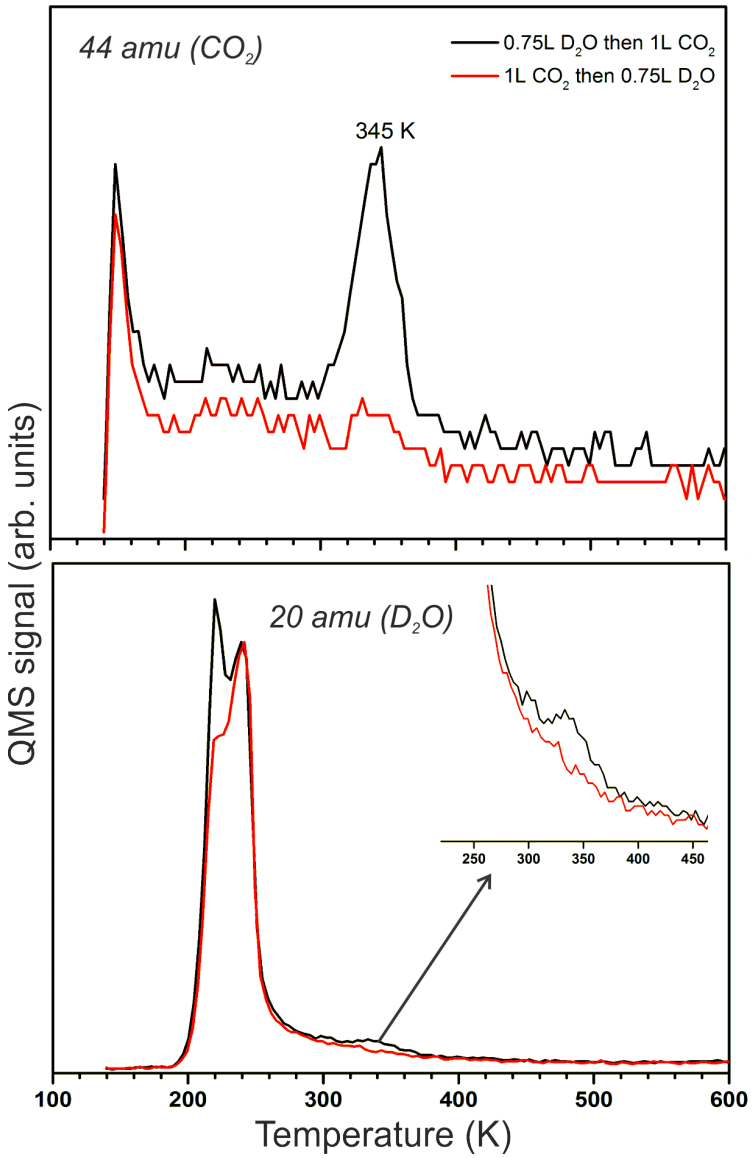

Figure 5.11: CO_2 and D_2O traces in TPD spectra recorded after 1 L CO_2 was dosed to Fe_3O_4(001) surface first pre-exposed to 0.75 L of D_2O at 140 K (black curve). The red curve is obtained for 0.75 L of D_2O dosed to the surface, first pre-treated with 1 L CO_2 at 140 K. The heating rate 3 K/s.

Figure 5.11 shows the TPD spectra for the desorption profiles of CO_2 and D_2O when the temperature is increased to 600 K with 3 K/sec. It is observed that when the (001) surface is first pre-treated with CO_2 and then D_2O, the desorption peak of CO_2 does not appear at 345 K, unlike the case of pre-treated with D_2O. This may be due to the fact that once the pre-treatment

is done first with CO_2, it probably blocks some sites which are required for D_2O to form the binding species for attachment with CO_2 or each other. It is also possible that D_2O need to remain close to each other for forming a particular geometry to react with CO_2.

It seems most likely that it will be bicarbonate which decomposes and releases water and carbon dioxide. Further investigation applying other techniques like STM, IRAS and theoretical calculations will provide more insights into the identification of these species.

The residual CO does not influence the adsorption of CO_2 in either of the planes (111 and 001) but it is more weakly adsorbed on (001) than on (111) surfaces. In the case of residual H_2O, it can be seen that the adsorption of CO_2 in the (111) plane is greatly influenced by the presence of H_2O which probably enhances the binding of CO_2 with the surface. However, in the (001) plane, the residual H_2O does not show any observable effect on the adsorption of CO_2.

5.4 Summary

The above studies again show that the UHV residual gases play a vital role for CO_2 adsorption. It can be summarized that adsorption of CO_2 on (111) is stronger than (001) and is dependent on the presence of water, either from residual gases or from the pre-treatment of the surface.

The pristine Fe_3O_4(111) and (001) weakly adsorb CO_2 on regular sites, having a desorption maximum below 100 K. However, the defect sites on (111) reveal a small peak around 200 K. It seems that, on a clean (111) surface, CO_2, water and CO interact with same sites. Besides, the (111) plane is more sensitive to traces of residual water as it is found that, with an increase in water content, the CO_2 binding gets stronger and hence desorption takes place at a higher temperature, i.e. 250 K.

For (001) surface, the residual water does not influence the adsorption of CO_2. However, in case of pre-treatment of (001) with D_2O, a particular exposure causes the adsorption, resulting in CO_2 desorption at a higher temperature, up to 340 K, which is substantially higher than observed for (111). Tentatively, we assigned simultaneous CO_2 and D_2O desorption at 340 K to

decomposition of bicarbonate species.

Finally, on both (001) and (111) facets, the residual CO (in UHV background) does not play any role in CO_2 adsorption. Besides, no evidence for water dissociation has been observed on either plane.

Chapter 6

Summary

Heterogeneous catalysts are widely used in the industrial sectors. Utilizing a model system approach, with its ultra-high vacuum conditions, tools, and techniques, is a key factor in understanding how (the mechanism by which) the active site of a heterogeneous catalyst works.Such model systems can be used to study structure reactivity relationships, thus bridging the "material" and "pressure" gaps, which remain challenging. The information obtained can furthermore be used to improve the catalytic processes, i.e. by developing new research strategies or by modifying the catalytic protocols.

In this Thesis, I have investigated the adsorption behavior of two differently oriented magnetite films (111) and (001) towards H_2O and CO_2, using LEED, IRAS, TP LEED, and TPD. The TPD data were thoroughly analyzed to calculate the adsorption parameters by applying different analysis methods, i.e., inversion analysis of the Polanyi–Wigner equation, "leading edge" analysis, the Redhead analysis, and the heating rate variation method (HRV).

First, the surface termination of prepared films was characterized by using CO as a probe molecule. There were contradictory reports on the surface termination of the (111) plane (Fe_{tet1} vs Fe_{oct}), hence I studied the termination using TPD. The latter method was compiled by IRAS and DFT investigations. The results clearly favor the model which shows that the Fe_3O_4(111) surface is tetrahedrally terminated by 1/4 monolayer Fe_{tet1} cations over closely-packed oxygen layer. Based on this knowledge the adsorption results were rationalized.

Then I addressed water adsorption. It has turned out that, the orientation of magnetite (111) and (001) affects the interaction of the water molecules

on the surface, through mechanisms like dissociation or molecular adsorption, thereby influencing the TPD profile and LEED pattern of the ice-like layer. The desorption energies were found to decrease from 110 to 50 kJ/mol as the coverage increased, thus indicating molecular adsorption. On the (111) plane, when the first water molecule approaches the surface, it dissociates to form hydroxyl ion on top of the Fe cation and a hydrogen ion that spills over surface oxygen to form the second hydroxyl. The hydroxyl groups then anchor other approaching water molecules and form dimer complexes. As the surface coverage increases, the dimer complexes form H-bond network resulting in ordered water ad-layer, as proved by LEED over the temperatures between 200 and 250 K. This process is thermodynamically driven.

In the case of the (001) plane, water initially follows molecular adsorption on the surface and as the coverage increases, partial dissociation of the water molecules takes place, forming dimer (or trimer)-like complexes that are bonded more strongly to the surface metal cations. Due to the square geometry of the (001) surface, water orders in (2×2) periodicity in a narrow temperature window, i.e. 175-187(±3) K showing a square symmetry. Such a structure was detected at high coverages, and is probably metastable and/or intermediate between mono- and multilayer water films.

Based on DFT-derived structures, one major difference between square and hexagonal ordered water driving force is that, for the (001) facet, at the highest coverage, the water molecules coordinate intermolecularly without forming direct bonds to the oxide surface. However, on the (111) facet, water hydrogen bonding network is the thermodynamically driving force. To the best of our knowledge, this is the first report of such an experimental LEED verification of two different ice-like layers on the same oxide surface. Temperature programmed LEED showed varying intensity of LEED spots upon desorption of water. This may be related to the change in the inter-layer of the surface due to the adsorption-desorption process of water. A complete I-V analysis over the studied temperature range is required in order to shed more light on the TP-LEED results. This remains a challenge.

It appears that carbon dioxide interaction with iron oxide is also structure sensitive. The study revealed differences in the desorption behavior of CO_2 on both facet surfaces. The critical role of the residual water is quite evident in

enhancing the adsorption process. CO residues seem to not affect the CO_2 adsorption.

On (111) orientation, at low dosage, the majority of CO_2 is physisorbed, leading to desorption at low temperature, <100 K. However, minority species may be chemisorbed (at $\sim$ 200 K) on defect sites. The greater the participation of residual water from UHV, the more strongly the CO_2 ($\sim$240 K) bonds to the surface. It noted that at low exposures, all the molecules, namely, CO, water, and CO_2 compete for defect sites.

For the water pre-treated surface, the CO_2 desorption takes place at a higher temperature ($\sim$250 K). When the surface is fully covered by water (2 ML) CO_2 signal increases by a factor of $\sim$3, which is indicative that probably CO_2 interacts with water species at specific sites and not directly bonded to the oxide surface.

Unlike (111), no evidence of chemisorption is observed, and the adsorption of CO_2 on (001) surface is only weak and hence the desorption occurred at low temperature (<100 K). The residual water and CO (in UHV background) did not show any significant influence on CO_2 adsorption. Once the surface has been pretreated with water, CO_2 interacts more strongly than in (111) facet, resulting in simultaneous CO_2 and D_2O desorption at 345 K. This interaction is seen only at a specific surface coverage, where water species seem to form a certain geometry to react with CO_2 molecules.

On either surface, the participation of residual water or pre-treated surfaces with water, plays a crucial role in CO_2 adsorption. However, the adsorption pattern is dependent on a certain limit of water coverage (species or/and geometry) which facilitates the interaction of CO_2 to the surface to be more efficient. The mechanism remains unknown, but we may speculate that the final product will be as bicarbonate.

From a future perspective, it would be good to identify the water species which are involved in enhanced reactivity of CO_2. Furthermore, it might be interesting to investigate whether the ordered structure of water ad-layer alters the chemistry of magnetite films.

It is also highly recommended to always monitor the participation of residual gases, in UHV background, otherwise the results might be misinterpreted.

Bibliography

[1] Krijn P De Jong. *Synthesis of solid catalysts*. John Wiley & Sons, 2009.

[2] Rochelle M Cornell and Udo Schwertmann. *The iron oxides: structure, properties, reactions, occurrences and uses*. John Wiley & Sons, 2003.

[3] Werner Weiss and Wolfgang Ranke. "Surface chemistry and catalysis on well-defined epitaxial iron-oxide layers". In: *Progress in Surface Science* 70.1-3 (2002), pp. 1–151.

[4] Helmut Kuhlenbeck, Shamil Shaikhutdinov, and Hans-Joachim Freund. "Well-ordered transition metal oxide layers in model catalysis–a series of case studies". In: *Chemical reviews* 113.6 (2013), pp. 3986–4034.

[5] Gareth S Parkinson. "Iron oxide surfaces". In: *Surface Science Reports* 71.1 (2016), pp. 272–365.

[6] Guido Ketteler, Werner Weiss, Wolfgang Ranke, and Robert Schlögl. "Bulk and surface phases of iron oxides in an oxygen and water atmosphere at low pressure". In: *Physical Chemistry Chemical Physics* 3.6 (2001), pp. 1114–1122.

[7] RM Cornel and Udo Schwertmann. *The iron oxides. Structure, properties, reactions and uses*. 1996.

[8] Gerd Binnig and Heinrich Rohrer. *Scanning tunneling microscope*. US Patent 4,343,993. Aug. 1982.

[9] CH Albright, PH Kasper, and Raja Rajendran. *Fermilab Meeting (Dpf 92), The-Proceedings Of The 7th Meeting Of The Aps Division Of Particles And Fields (In 2 Volumes)*. World Scientific, 1993.

[10] RM Cornell and U Schwertmann. "Properties". In: *The Iron Oxides, Structure, Properties, Reaction, Occurrence and Uses (Cornell RM, Schwertman U., Eds), VCH Weinheim-NewYork-Basel-Cambridge-Tokyo* (1996), pp. 87–121.

[11] EJW Verwey. "Electronic conduction of magnetite (Fe 3 O 4) and its transition point at low temperatures". In: *Nature* 144.3642 (1939), p. 327.

[12] RM Cornell and U Schwertmann. *The Iron Oxides, VCH*. 1996.

[13] JMD Coey and CL Chien. "Half-metallic ferromagnetic oxides". In: *Mrs Bulletin* 28.10 (2003), pp. 720–724.

[14] G Hu and Y Suzuki. "Negative Spin Polarization of F e 3 O 4 in Magnetite/Manganite-Based Junctions". In: *Physical review letters* 89.27 (2002), p. 276601.

[15] John C Mallinson. *The foundations of magnetic recording*. Elsevier, 2012.

[16] JW Geus. "Preparation and properties of iron oxide and metallic iron catalysts." In: *Applied Catalysis* 25.1-2 (1986), pp. 313–333.

[17] Do-Kyung Kim, Yu Zhang, W Voit, KV Rao, J Kehr, B Bjelke, and Mamoun Muhammed. "Superparamagnetic iron oxide nanoparticles for bio-medical applications". In: *Scripta materialia* 44.8-9 (2001), pp. 1713–1717.

[18] Andreas Jordan, Regina Scholz, Peter Wust, Horst Fähling, and Roland Felix. "Magnetic fluid hyperthermia (MFH): Cancer treatment with AC magnetic field induced excitation of biocompatible superparamagnetic nanoparticles". In: *Journal of Magnetism and Magnetic materials* 201.1-3 (1999), pp. 413–419.

[19] CFR Lund and E Kubsh Joseph. "A. J. Dumesic, Water gas shift over magnetite based catalysts, solid state chemistry in catalysis". In: *Chem. Soc. Symp. Ser.* Vol. 279. 1985, pp. 313–338.

[20] Senzi Li, George D Meitzner, and Enrique Iglesia. "Structure and site evolution of iron oxide catalyst precursors during the Fischer- Tropsch synthesis". In: *The Journal of Physical Chemistry B* 105.24 (2001), pp. 5743–5750.

[21] Kurt O Konhauser. "Diversity of bacterial iron mineralization". In: *Earth-Science Reviews* 43.3-4 (1998), pp. 91–121.

[22] Eman Zaki, Zdenek Jakub, Francesca Mirabella, Gareth S Parkinson, Shamil Shaikhutdinov, and Hans-Joachim Freund. "Water Ordering on the Magnetite Fe3O4 Surfaces". In: *The journal of physical chemistry letters* 10 (2019), pp. 2487–2492.

[23] PW Tasker. "The stability of ionic crystal surfaces". In: *Journal of Physics C: Solid State Physics* 12.22 (1979), p. 4977.

[24] A Barbieri, W Weiss, MA Van Hove, and GA Somorjai. "Magnetite Fe3O4 (111): surface structure by LEED crystallography and energetics". In: *Surface Science* 302.3 (1994), pp. 259–279.

[25] W Weiss, A Barbieri, MA Van Hove, and Gabor A Somorjai. "Surface structure determination of an oxide film grown on a foreign substrate: Fe 3 O 4 multilayer on Pt (111) identified by low energy electron diffraction". In: *Physical review letters* 71.12 (1993), p. 1848.

[26] M Ritter and W Weiss. "Fe3O4 (111) surface structure determined by LEED crystallography". In: *Surface Science* 432.1-2 (1999), pp. 81–94.

[27] Alessandro Sala, Helder Marchetto, Z-H Qin, Sh Shaikhutdinov, Th Schmidt, and H-J Freund. "Defects and inhomogeneities in Fe 3 O 4 (111) thin film growth on Pt (111)". In: *Physical Review B* 86.15 (2012), p. 155430.

[28] YJ Kim, C Westphal, RX Ynzunza, Z Wang, HC Galloway, M Salmeron, MA Van Hove, and CS Fadley. "The growth of iron oxide films on Pt (111): a combined XPD, STM, and LEED study". In: *Surface Science* 416.1-2 (1998), pp. 68–111.

[29] IV Shvets, N Berdunov, G Mariotto, and S Murphy. "Formation of the strain-induced electronic superstructure on the magnetite (111) surface". In: *EPL (Europhysics Letters)* 63.6 (2003), p. 867.

[30] AR Lennie, NG Condon, FM Leibsle, PW Murray, G Thornton, and DJ Vaughan. "Structures of Fe 3 O 4 (111) surfaces observed by scanning tunneling microscopy". In: *Physical Review B* 53.15 (1996), p. 10244.

[31] NG Condon, FM Leibsle, T Parker, AR Lennie, DJ Vaughan, and G Thornton. "Biphase ordering on Fe 3 O 4 (111)". In: *Physical Review B* 55.23 (1997), p. 15885.

[32] Céline Lemire, Randall Meyer, Victor E Henrich, Sh Shaikhutdinov, and H-J Freund. "The surface structure of Fe3O4 (1 1 1) films as studied by CO adsorption". In: *Surface science* 572.1 (2004), pp. 103–114.

[33] RS Cutting, CA Muryn, DJ Vaughan, and G Thornton. "Substrate-termination and H2O-coverage dependent dissociation of H2O on Fe3O4 (1 1 1)". In: *Surface Science* 602.6 (2008), pp. 1155–1165.

[34] Pengyan Xue, Zhaoming Fu, and Zongxian Yang. "The density functional theory studies on the promoting effect of the Cu-modified Fe3O4 catalysts". In: *Physics Letters A* 379.6 (2015), pp. 607–612.

[35] Dong-Mei Huang, Dong-Bo Cao, Yong-Wang Li, and Haijun Jiao. "Density function theory study of CO adsorption on Fe3O4 (111) surface". In: *The Journal of Physical Chemistry B* 110.28 (2006), pp. 13920–13925.

[36] Adam Kiejna, Tomasz Ossowski, and Tomasz Pabisiak. "Surface properties of the clean and Au/Pd covered Fe 3 O 4 (111): DFT andDFT+ U study". In: *Physical Review B* 85.12 (2012), p. 125414.

[37] Jamila Ahdjoudj, Cyril Martinsky, Christian Minot, Michel A Van Hove, and Gabor A Somorjai. "Theoretical study of the termination of the Fe3O4 (111) surface". In: *Surface science* 443.1-2 (1999), pp. 133–153.

[38] L Zhu, KL Yao, and ZL Liu. "First-principles study of the polar (111) surface of Fe 3 O 4". In: *Physical Review B* 74.3 (2006), p. 035409.

[39] Xiaohu Yu, Chun-Fang Huo, Yong-Wang Li, Jianguo Wang, and Haijun Jiao. "Fe3O4 surface electronic structures and stability from GGA+ U". In: *Surface Science* 606.9-10 (2012), pp. 872–879.

[40] Maria Elena Grillo, Mike W Finnis, and Wolfgang Ranke. "Surface structure and water adsorption on Fe 3 O 4 (111): Spin-density functional theory and on-site Coulomb interactions". In: *Physical Review B* 77.7 (2008), p. 075407.

[41] Junghyun Noh, Osman I Osman, Saadullah G Aziz, Paul Winget, and Jean-Luc Brédas. "Magnetite Fe3O4 (111) surfaces: Impact of defects on structure, stability, and electronic properties". In: *Chemistry of Materials* 27.17 (2015), pp. 5856–5867.

[42] R Bliem, E McDermott, P Ferstl, M Setvin, O Gamba, J Pavelec, MA Schneider, M Schmid, U Diebold, P Blaha, et al. "Subsurface cation vacancy stabilization of the magnetite (001) surface". In: *Science* 346.6214 (2014), pp. 1215–1218.

[43] Gareth S Parkinson, Zbyněk Novotný, Peter Jacobson, Michael Schmid, and Ulrike Diebold. "A metastable Fe (A) termination at the Fe3O4 (001) surface". In: *Surface Science* 605.15-16 (2011), pp. L42–L45.

[44] Earl M Davis, Ke Zhang, Yi Cui, Helmut Kuhlenbeck, Shamil Shaikhutdinov, and Hans-Joachim Freund. "Growth of Fe3O4 (001) thin films on Pt (100): Tuning surface termination with an Fe buffer layer". In: *Surface Science* 636 (2015), pp. 42–46.

[45] David A King and Michael G Wells. "Molecular beam investigation of adsorption kinetics on bulk metal targets: Nitrogen on tungsten". In: *Surface Science* 29.2 (1972), pp. 454–482.

[46] M Pl Seah and WA Dench. "Quantitative electron spectroscopy of surfaces: A standard data base for electron inelastic mean free paths in solids". In: *Surface and interface analysis* 1.1 (1979), pp. 2–11.

[47] Michel A Van Hove, William H Weinberg, and Chi-Ming Chan. "The LEED Experiment". In: *Low-Energy Electron Diffraction*. Springer, 1986, pp. 13–46.

[48] Michel A Vanhove, William Henry Weinberg, and Chi-Ming Chan. *Low-energy electron diffraction: experiment, theory and surface structure determination*. Vol. 6. Springer Science & Business Media, 2012.

[49] G Ertl, J Küppers, and Manfred Grasserbauer. *Low energy electrons and surface chemistry, 2nd edn.: VCH, Weinheim, 1985 (ISBN 3-527-26056-0). xii+ 374 pp. Price DM 168.* 1987.

[50] John Brian Pendry. *Low energy electron diffraction: the theory and its application to determination of surface structure*. Vol. 2. Academic Press, 1974.

[51] Louis De Broglie. "Recherches sur la théorie des quanta". PhD thesis. Migration-université en cours d'affectation, 1924.

[52] BE Warren. "X-ray Diffraction. Dover". In: *New York* 253 (1990).

[53] Vitalij K Pecharsky and Peter Y Zavalij. "Fundamentals of diffraction". In: *Fundamentals of Powder Diffraction and Structural Characterization of Materials* (2003), pp. 99–260.

[54] Mario Birkholz. *Thin film analysis by X-ray scattering*. John Wiley & Sons, 2006.

[55] Pierre Auger. "Sur l'effet photoélectrique composé". In: *Journal de Physique et le Radium* 6.6 (1925), pp. 205–208.

[56] PW Palmberg and TN Rhodin. "Auger electron spectroscopy of fcc metal surfaces". In: *Journal of Applied Physics* 39.5 (1968), pp. 2425–2432.

[57] LA Harris. "Analysis of materials by electron-excited Auger electrons". In: *Journal of Applied Physics* 39.3 (1968), pp. 1419–1427.

[58] Gerhard Ertl and Jürgen Küppers. *Low energy electrons and surface chemistry*. 1985.

[59] FP Larkins. "Theoretical developments in high resolution Auger electron studies of solids". In: *Applications of Surface Science* 13.1-2 (1982), pp. 4–34.

[60] Brian E Hayden. "Reflection absorption infrared spectroscopy". In: *Vibrational spectroscopy of molecules on surfaces*. Springer, 1987, pp. 267–344.

[61] RJ Bell. "Introductory Fuorier Transform Spectroscopy, Acad". In: *Press, New York* (1972).

[62] Peter R Griffiths et al. *Chemical infrared Fourier transform spectroscopy*. Wiley, 1975.

[63] Günzler Helmut and Hans Michael Heise. *IR Spectroscopy: An Introduction*. Wiley-VCH, 2000.

[64] H Günzler and HM Heise. *IR spectroscopy: an introduction. 2002*.

[65] B Schraeder. "Early history of vibrational spectroscopy". In: *Infrared and Raman Spectroscopy: Methods and Applications" Edited by Schrader, B., VCH, Weinheim, Germany* (1995).

[66] Robert G Greenler, Robert R Rahn, and John P Schwartz. "The effect of index of refraction on the position, shape, and intensity of infrared bands in reflection-absorption spectra". In: *Journal of catalysis* 23.1 (1971), pp. 42–48.

[67] JDE McIntyre and David E Aspnes. "Differential reflection spectroscopy of very thin surface films". In: *Surface Science* 24.2 (1971), pp. 417–434.

[68] Susan B Piepho and Paul N Schatz. *Group theory in spectroscopy: with applications to magnetic circular dichroism*. Vol. 1. 337. Wiley-Interscience, 1983.

[69] H Ibach. "Proceedings of the Conference on Vibrations in Adsorbed Layers". In: *Julich, Germany* (1978), p. 64.

[70] Friedrich M Hoffmann. "Infrared reflection-absorption spectroscopy of adsorbed molecules". In: *Surface Science Reports* 3.2-3 (1983), pp. 107–192.

[71] TB Grimley. "The Normal Mode Frequencies of Chemisorbed Atoms and Molecules". In: *Proceedings of the Physical Society* 79.6 (1962), p. 1203.

[72] G Blyholder. "CNDO model of carbon monoxide chemisorbed on nickel". In: *The Journal of Physical Chemistry* 79.7 (1975), pp. 756–761.

[73] Shlomo Efrima and Horia Metiu. "The role of the electrostatic interaction in shifting the vibrational frequencies for two adsorbed molecules". In: *Surface Science* 109.1 (1981), pp. 109–126.

[74] Le Roy Apker. "Surface phenemona useful in vacuum technique". In: *Industrial & Engineering Chemistry* 40.5 (1948), pp. 846–847.

[75] PA Redhead. "Thermal desorption of gases". In: *vacuum* 12.4 (1962), pp. 203–211.

[76] Y Amenomiya and RJ Cvetanovic. "Application of flash-desorption method to catalyst studies.I. Ethylene- alumina system1". In: *The Journal of Physical Chemistry* 67.1 (1963), pp. 144–147.

[77] K Wittmaack. "Successful operation of a scanning ion microscope with quadrupole mass filter". In: *Review of Scientific Instruments* 47.1 (1976), pp. 157–158.

[78] JW Niemantsverdriet. *Spectroscopy in Catalysis, an Introduction, VCl—l.* 1993.

[79] Richard I Masel. *Principles of adsorption and reaction on solid surfaces.* Vol. 3. John Wiley & Sons, 1996.

[80] David A King. "Thermal desorption from metal surfaces: A review". In: *Surface Science* 47.1 (1975), pp. 384–402.

[81] JB Miller, HR Siddiqui, SM Gates, JN Russell Jr, JT Yates Jr, JC Tully, and MJ Cardillo. "Extraction of kinetic parameters in temperature programmed desorption: A comparison of methods". In: *The Journal of chemical physics* 87.11 (1987), pp. 6725–6732.

[82] AM De Jong and JW Niemantsverdriet. "Thermal desorption analysis: Comparative test of ten commonly applied procedures". In: *Surface Science* 233.3 (1990), pp. 355–365.

[83] DLS Nieskens, AP Van Bavel, and JW Niemantsverdriet. "The analysis of temperature programmed desorption experiments of systems with lateral interactions; implications of the compensation effect". In: *Surface science* 546.2-3 (2003), pp. 159–169.

[84] JW Niemantsverdriet, P Dolle, K Markert, and K Wandelt. "Thermal desorption of strained monoatomic Ag and Au layers from Ru (001)". In: *Journal of Vacuum Science & Technology A: Vacuum, Surfaces, and Films* 5.4 (1987), pp. 875–878.

[85] Steven L Tait, Zdenek Dohnálek, Charles T Campbell, and Bruce D Kay. "n-alkanes on MgO (100). I. Coverage-dependent desorption kinetics of n-butane". In: *The Journal of chemical physics* 122.16 (2005), p. 164707.

[86] R Scott Smith and Bruce D Kay. "Desorption Kinetics of Benzene and Cyclohexane from a Graphene Surface". In: *The Journal of Physical Chemistry B* 122.2 (2017), pp. 587–594.

[87] E Habenschaden and J Küppers. "Evaluation of flash desorption spectra". In: *Surface science letters* 138.1 (1984), pp. L147–L150.

[88] Frances M Lord and JS Kittelberger. "On the determination of activation energies in thermal desorption experiments". In: *Surface Science* 43.1 (1974), pp. 173–182.

[89] X Li, J Paier, Joachim Sauer, Francesca Mirabella, Eman Zaki, Francisco Ivars-Barceló, S Shaikhutdinov, and H-J Freund. "Surface termination of Fe3O4 (111) films studied by CO adsorption revisited". In: *The Journal of Physical Chemistry B* 122.2 (2017), pp. 527–533.

[90] L Torrente-Murciano, D Mattia, MD Jones, and PK Plucinski. "Formation of hydrocarbons via CO2 hydrogenation–A thermodynamic study". In: *Journal of CO2 Utilization* 6 (2014), pp. 34–39.

[91] Nikolay G Petrik and Greg A Kimmel. "Adsorption Geometry of CO versus Coverage on TiO2 (110) from s-and p-Polarized Infrared Spectroscopy". In: *The journal of physical chemistry letters* 3.23 (2012), pp. 3425–3430.

[92] Zdenek Dohnálek, Jooho Kim, Oleksandr Bondarchuk, J Mike White, and Bruce D Kay. "Physisorption of N2, O2, and CO on fully oxidized TiO2 (110)". In: *The Journal of Physical Chemistry B* 110.12 (2006), pp. 6229–6235.

[93] P Ferstl, S Mehl, Mohammad A Arman, M Schuler, A Toghan, B Laszlo, Y Lykhach, O Brummel, Edvin Lundgren, Jan Knudsen, et al. "Adsorption and activation of CO on Co3O4 (111) thin films". In: *The Journal of Physical Chemistry C* 119.29 (2015), pp. 16688–16699.

[94] Mohammad A Arman, Lindsay R Merte, Edvin Lundgren, and Jan Knudsen. "Co3O4 (100) films grown on Ag (100): Structure and chemical properties". In: *Surface Science* 657 (2017), pp. 90–95.

[95] Terrence J Udovic and JA Dumesic. "Adsorptive properties of magnetite surfaces as studied by temperature-programmed desorption: Studies of O2, NO, CO2, and CO adsorption". In: *Journal of Catalysis* 89.2 (1984), pp. 314–326.

[96] Masao Watanabe and Toru Kadowaki. "Dissociation reactions of CO gas on Fe and Fe3O4 surfaces observed by Raman-ellipsometry spectroscopy". In: *Applied Surface Science* 28.2 (1987), pp. 147–166.

[97] Pengyan Xue, Zhaoming Fu, Xingli Chu, Yanxing Zhang, and Zongxian Yang. "Density functional theory study on the interaction of CO with the Fe3O4 (0 0 1) surface". In: *Applied Surface Science* 317 (2014), pp. 752–759.

[98] G Ertl, M Neumann, and KM Streit. "Chemisorption of CO on the Pt (111) surface". In: *Surface Science* 64.2 (1977), pp. 393–410.

[99] H Steininger, S Lehwald, and H Ibach. "On the adsorption of CO on Pt (111)". In: *Surface Science* 123.2-3 (1982), pp. 264–282.

[100] Victor E Henrich and Shamil K Shaikhutdinov. "Atomic geometry of steps on metal-oxide single crystals". In: *Surface science* 574.2-3 (2005), pp. 306–316.

[101] Gianfranco Pacchioni, Giuseppe Cogliandro, and Paul S Bagus. "Characterization of oxide surfaces by infrared spectroscopy of adsorbed carbon monoxide: a theoretical investigation of the frequency shift of CO on MgO and NiO". In: *Surface science* 255.3 (1991), pp. 344–354.

[102] Jan Hulva, Zdeněk Jakub, Zbynek Novotny, Niclas Johansson, Jan Knudsen, Joachim Schnadt, Michael Schmid, Ulrike Diebold, and Gareth S Parkinson. "Adsorption of CO on the Fe3O4 (001) surface". In: *The Journal of Physical Chemistry B* 122.2 (2017), pp. 721–729.

[103] MM Khader, GH Vurens, IK Kim, M Salmeron, and GA Somorjai. "Photoassisted catalytic dissociation of water to produce hydrogen on partially reduced. alpha.-iron (III) oxide". In: *Journal of the American Chemical Society* 109.12 (1987), pp. 3581–3585.

[104] W Weiss, D Zscherpel, and R Schlögl. "On the nature of the active site for the ethylbenzene dehydrogenation over iron oxide catalysts". In: *Catalysis letters* 52.3-4 (1998), pp. 215–220.

[105] David S Newsome. "The water-gas shift reaction". In: *Catalysis Reviews Science and Engineering* 21.2 (1980), pp. 275–318.

[106] Yvonne Joseph, Christian Kuhrs, Wolfgang Ranke, Michael Ritter, and Werner Weiss. "Adsorption of water on FeO (111) and Fe3O4 (111): identification of active sites for dissociation". In: *Chemical Physics Letters* 314.3-4 (1999), pp. 195–202.

[107] Yvonne Joseph, Wolfgang Ranke, and Werner Weiss. "Water on FeO (111) and Fe3O4 (111): Adsorption behavior on different surface terminations". In: *The Journal of Physical Chemistry B* 104.14 (2000), pp. 3224–3236.

[108] Ulrich Leist, Wolfgang Ranke, and Katharina Al-Shamery. "Water adsorption and growth of ice on epitaxial Fe 3 O 4 (111), FeO (111) and Fe 2 O 3 (biphase)". In: *Physical Chemistry Chemical Physics* 5.11 (2003), pp. 2435–2441.

[109] Petr Dementyev, Karl-Heinz Dostert, Francisco Ivars-Barceló, Casey P O'Brien, Francesca Mirabella, Swetlana Schauermann, Xiaoke Li, Joachim Paier, Joachim Sauer, and Hans-Joachim Freund. "Water interaction with iron oxides". In: *Angewandte Chemie International Edition* 54.47 (2015), pp. 13942–13946.

[110] K Adib, GG Totir, JP Fitts, KT Rim, T Mueller, GW Flynn, SA Joyce, and RM Osgood Jr. "Chemistry of CCl4 on Fe3O4 (1 1 1)-(2× 2) surfaces in the presence of adsorbed D2O studied by temperature programmed desorption". In: *Surface science* 537.1-3 (2003), pp. 191–204.

[111] T Kendelewicz, Ping Liu, CS Doyle, GE Brown Jr, Eric J Nelson, and Scott A Chambers. "Reaction of water with the (100) and (111) surfaces of Fe3O4". In: *Surface Science* 453.1-3 (2000), pp. 32–46.

[112] Kwang Taeg Rim, Daejin Eom, Siu-Wai Chan, Maria Flytzani-Stephanopoulos, George W Flynn, Xiao-Dong Wen, and Enrique R Batista. "Scanning tunneling microscopy and theoretical study of water adsorption on Fe3O4: Implications for catalysis". In: *Journal of the American Chemical Society* 134.46 (2012), pp. 18979–18985.

[113] Chenggang Zhou, Qingfan Zhang, Lei Chen, Bo Han, Gang Ni, Jinping Wu, Diwakar Garg, and Hansong Cheng. "Density functional theory study of water dissociative chemisorption on the Fe3O4 (111) surface". In: *The Journal of Physical Chemistry C* 114.49 (2010), pp. 21405–21410.

[114] Xiaoke Li and Joachim Paier. "Adsorption of water on the Fe3O4 (111) surface: Structures, stabilities, and vibrational properties studied by density functional theory". In: *The Journal of Physical Chemistry C* 120.2 (2016), pp. 1056–1065.

[115] Francesca Mirabella, Eman Zaki, Francisco Ivars-Barceló, Xiaoke Li, Joachim Paier, Joachim Sauer, Shamil Shaikhutdinov, and Hans-Joachim Freund. "Cooperative Formation of Long-Range Ordering in Water Ad-layers on Fe3O4 (111) Surfaces". In: *Angewandte Chemie International Edition* 57.5 (2018), pp. 1409–1413.

[116] Eman Zaki, Francesca Mirabella, Francisco Ivars-Barceló, Jan Seifert, Spencer Carey, Shamil Shaikhutdinov, Hans-Joachim Freund, Xiaoke Li, Joachim Paier, and Joachim Sauer. "Water adsorption on the Fe 3 O 4 (111) surface: dissociation and network formation". In: *Physical Chemistry Chemical Physics* 20.23 (2018), pp. 15764–15774.

[117] Patricia A Thiel and Theodore E Madey. "The interaction of water with solid surfaces: fundamental aspects". In: *Surface Science Reports* 7.6-8 (1987), pp. 211–385.

[118] Michael A Henderson. "The interaction of water with solid surfaces: fundamental aspects revisited". In: *Surface Science Reports* 46.1-8 (2002), pp. 1–308.

[119] A Glebov, AP Graham, A Menzel, and JP Toennies. "Orientational ordering of two-dimensional ice on Pt (111)". In: *The Journal of chemical physics* 106.22 (1997), pp. 9382–9385.

[120] N Materer. "N. Materer, U. Starke, A. Barbieri, MA van Hove, GA Somorjai, GJ Kroes, and C. Minot, Surf. Sci. 381, 190 (1997)." In: *Surf. Sci.* 381 (1997), p. 190.

[121] S Haq, J Harnett, and A Hodgson. "Growth of thin crystalline ice films on Pt (111)". In: *Surface science* 505 (2002), pp. 171–182.

[122] PA Thiel, FM Hoffmann, and WH Weinberg. "Monolayer and multilayer adsorption of water on Ru (001)". In: *The Journal of Chemical Physics* 75.11 (1981), pp. 5556–5572.

[123] Theodore E Madey and Faiko P Netzer. "The adsorption of H2O on Ni (111); influence of preadsorbed oxygen on azimuthal ordering". In: *Surface Science* 117.1-3 (1982), pp. 549–560.

[124] KD Gibson, M Viste, and SJ Sibener. "The adsorption of water on clean and oxygen predosed Rh (111): Surface templating via (1× 1)-O/Rh (111) induces formation of a novel high-density interfacial ice structure". In: *The Journal of Chemical Physics* 112.21 (2000), pp. 9582–9589.

[125] Sheng Meng, Efthimios Kaxiras, and Zhenyu Zhang. "Water wettability of close-packed metal surfaces". In: *The Journal of chemical physics* 127.24 (2007), p. 244710.

[126] H Ogasawara, B Brena, D Nordlund, M Nyberg, A Pelmenschikov, LGM Pettersson, and A Nilsson. "Structure and bonding of water on Pt (111)". In: *Physical review letters* 89.27 (2002), p. 276102.

[127] Bernd Meyer, Dominik Marx, Olga Dulub, Ulrike Diebold, Martin Kunat, Deler Langenberg, and Christof Wöll. "Partial dissociation of water leads to stable superstructures on the surface of zinc oxide". In: *Angewandte Chemie International Edition* 43.48 (2004), pp. 6641–6645.

[128] C Xu and DW Goodman. "Structure and geometry of water adsorbed on the MgO (100) surface". In: *Chemical physics letters* 265.3-5 (1997), pp. 341–346.

[129] D Ferry, A Glebov, V Senz, J Suzanne, JP Toennies, and H Weiss. "Observation of the second ordered phase of water on the MgO (100) surface: Low energy electron diffraction and helium atom scattering studies". In: *The Journal of chemical physics* 105.4 (1996), pp. 1697–1701.

[130] Radosław Włodarczyk, Marek Sierka, Karolina Kwapien, Joachim Sauer, Esther Carrasco, Andreas Aumer, Janaina F Gomes, Martin Sterrer, and Hans-Joachim Freund. "Structures of the ordered water monolayer on MgO (001)". In: *The Journal of Physical Chemistry C* 115.14 (2011), pp. 6764–6774.

[131] Narasimham Mulakaluri, Rossitza Pentcheva, Maria Wieland, Wolfgang Moritz, and Matthias Scheffler. "Partial dissociation of water on Fe 3 O 4 (001): Adsorbate induced charge and orbital order". In: *Physical review letters* 103.17 (2009), p. 176102.

[132] Narasimham Mulakaluri, Rossitza Pentcheva, and Matthias Scheffler. "Coverage-dependent adsorption mode of water on Fe3O4 (001): Insights from first principles calculations". In: *The Journal of Physical Chemistry C* 114.25 (2010), pp. 11148–11156.

[133] Shuming Liu, Shuai Wang, Wentao Li, Jiandong Guo, and Qinlin Guo. "Water dissociation on magnetite (001) films". In: *The Journal of Physical Chemistry C* 117.27 (2013), pp. 14070–14074.

[134] Gareth S Parkinson, Zbyněk Novotný, Peter Jacobson, Michael Schmid, and Ulrike Diebold. "Room temperature water splitting at the surface of magnetite". In: *Journal of the American Chemical Society* 133.32 (2011), pp. 12650–12655.

[135] Matthias Meier, Jan Hulva, Zdeněk Jakub, Jiř'ı Pavelec, Martin Setvin, Roland Bliem, Michael Schmid, Ulrike Diebold, Cesare Franchini, and Gareth S Parkinson. "Water agglomerates on Fe3O4 (001)". In: *Proceedings of the National Academy of Sciences* 115.25 (2018), E5642–E5650.

[136] VP Zhdanov. "On the kinetics of CO oxidation over the Ir (111) surface". In: *Surface science* 137.2-3 (1984), pp. 515–526.

[137] VP Zhdanov. "Lattice-gas model for description of adsorbed molecules; Application to CO oxidation on Ir (110)". In: *Surface Science* 123.1 (1982), pp. 106–116.

[138] Vladimir Petrovich Zhdanov. "Arrhenius parameters for rate processes on solid surfaces". In: *Surface Science Reports* 12.5 (1991), pp. 185–242.

[139] VP Zhdanov, J Pavl'ıček, and Z Knor. "Preexponential factors for elementary surface processes". In: *Catalysis Reviews Science and Engineering* 30.4 (1988), pp. 501–517.

[140] Bert Metz, Ogunlade Davidson, Heleen De Coninck, Manuela Loos, and Leo Meyer. *IPCC special report on carbon dioxide capture and storage*. Tech. rep. Intergovernmental Panel on Climate Change, Geneva (Switzerland). Working . . ., 2005.

[141] H-J Freund and Meirion Wynn Roberts. "Surface chemistry of carbon dioxide". In: *Surface Science Reports* 25.8 (1996), pp. 225–273.

[142] Uwe Burghaus. "Surface chemistry of CO2–Adsorption of carbon dioxide on clean surfaces at ultrahigh vacuum". In: *Progress in Surface Science* 89.2 (2014), pp. 161–217.

[143] William Taifan, Jean-François Boily, and Jonas Baltrusaitis. "Surface chemistry of carbon dioxide revisited". In: *Surface Science Reports* 71.4 (2016), pp. 595–671.

[144] Zhang Chun-lei, Liu Zhi-qiang, Wu Tong-hao, Yang Hong-mao, Jiang Yu-zi, and Peng Shao-yi. "Complete reduction of carbon dioxide to carbon and indirect conversion to O2 using cation-excess magnetite". In: *Materials chemistry and physics* 44.2 (1996), pp. 194–198.

[145] Jesper Nerlov, Søren V Hoffmann, Masaru Shimomura, and Preben J Møller. "Coadsorption of Na and CO2 on the Fe3O4 (111) termination of α-Fe2O3 (0001): relations between structure and activation". In: *Surface science* 401.1 (1998), pp. 56–71.

[146] Yutaka Tamaura and Ken'ichi Nishizawa. "CO2 decomposition into C and conversion into CH4 using the H2-reduced magnetite". In: *Energy Conversion and Management* 33.5-8 (1992), pp. 573–577.

[147] Tongming Su, Zuzeng Qin, Guan Huang, Hongbing Ji, Yuexiu Jiang, and Jianhua Chen. "Density functional theory study on the interaction of CO2 with Fe3O4 (111) surface". In: *Applied Surface Science* 378 (2016), pp. 270–276.

[148] David Santos-Carballal, Alberto Roldan, Nelson Y Dzade, and Nora H de Leeuw. "Reactivity of CO2 on the surfaces of magnetite (Fe3O4), greigite (Fe3S4) and mackinawite (FeS)". In: *Philosophical Transactions of the Royal Society A: Mathematical, Physical and Engineering Sciences* 376.2110 (2017), p. 20170065.

[149] David Santos-Carballal, Alberto Roldan, Ricardo Grau-Crespo, and Nora H de Leeuw. "A DFT study of the structures, stabilities and redox behaviour of the major surfaces of magnetite Fe 3 O 4". In: *Physical Chemistry Chemical Physics* 16.39 (2014), pp. 21082–21097.

[150] Jiri Pavelec, Jan Hulva, Daniel Halwidl, Roland Bliem, Oscar Gamba, Zdenek Jakub, Florian Brunbauer, Michael Schmid, Ulrike Diebold, and Gareth S Parkinson. "A multi-technique study of CO2 adsorption on Fe3O4 magnetite". In: *The Journal of chemical physics* 146.1 (2017), p. 014701.

[151] Francesca Mirabella, Eman Zaki, Francisco Ivars-Barcelo, Swetlana Schauermann, Shamil Shaikhutdinov, and H-J Freund. "CO2 Adsorption on Magnetite Fe3O4 (111)". In: *The Journal of Physical Chemistry C* 122.48 (2018), pp. 27433–27441.

[152] Michael A Henderson. "Evidence for bicarbonate formation on vacuum annealed TiO2 (110) resulting from a precursor-mediated interaction between CO2 and H2O". In: *Surface Science* 400.1-3 (1998), pp. 203–219.

appendix

List of Abbreviations

UHV Ultra High Vacuum
STM The Scanning Tunneling Microscopy
LEED Low Energy Electron Diffraction
IRAS Infrared Reflection Absorption Spectroscopy
TP- Temperature-Programmed
TPD Temperature-Programmed Desorption
QMS Quadrupole Mass Spectrometer
XPS X-Ray Photoelectron Spectroscopy
XRD X-Ray Diffraction
DFT Density Functional Theory
GC Gas Chromatography
AFM Atomic Force Microscopy
ML Monolayer

List of Publications

1- Water ordering on the magnetite Fe_3O_4 surfaces, **E. Zaki**, Z. Jakub, F. Mirabella, G. S. Parkinson, S. Shaikhutdinov, H.-J. Freund. J. Phys. Chem. Lett., 2019, 10, pp 2487–2492, DOI: 10.1021/acs.jpclett.9b00773.

2- CO_2 Adsorption on Magnetite $Fe_3O_4(111)$, F. Mirabella*, **E. Zaki***, F. Ivars-Barceló, S. Shaikhutdinov, H.-J. Freund, J. Phys. Chem. C, 22, (2018) 27433–27441.

3 - Water Adsorption on the $Fe_3O_4(111)$ Surface: Dissociation and Network Formation, **E. Zaki***, F. Mirabella*, F. Ivars-Barceló, J. Seifert, S. Carey, S. Shaikhutdinov, H.-J. Freund, X. Li*, J. Paier, J. Sauer, Phys. Chem. Chem. Phys., 20 (2018)15764-15774. This article is part of the themed collection: 2018 PCCP HOT Articles

4- Cooperative Formation of Long-Range Ordering in Water Ad-layers on $Fe_3O_4(111)$ Surfaces, F. Mirabella*, **E. Zaki***, F. Ivars-Barceló, X. Li*, J. Paier, J. Sauer, S. Shaikhutdinov, H.- J. Freund, Angew. Chem. Int. Ed. 2018, 57, 1409-1413; Angew. Chem. 130 (2018) 1423- 1428.

5- Surface Termination of $Fe_3O_4(111)$ Films Studied by CO Adsorption Revisited, X. Li, J. Paier, J. Sauer, F. Mirabella, **E. Zaki**, F. Ivars-Barceló, S. Shaikhutdinov, H.-J. Freund, J. Phys. Chem. B., 122 (2018) 527-533.

6- Effect of Water on Inorganic Acids Doped Polyaniline, M.M. Ayad and **E. A. Zaki**, J Appl Polym Sci, 114 (2009) 1384-1389.

7- Dielectric properties investigation of polyaniline prepared by using Fenton reagent, M.M. Ayad, M.K. El –Nimr and **E.A. Zaki**, International Journal of Polymer Anal. Charact.14 (2009) 652–665.

8- Synthesis and characterization of silver–polypyrrole film composite, M.M. Ayad and **E. A. Zaki**, Applied Surface Science, 256 (2009)787–791.

9- Quartz crystal microbalance and spectroscopy measurements for acid dop-

ing in polyaniline films, M.M. Ayad and **E. A. Zaki**, Sci. Technol. Adv. Mater. 9 (2008)015007(10 pp).

10- Doping of polyaniline films with organic sulfonic acids in aqueous media and the effect of water on these doped films, M.M. Ayad and **E. A. Zaki**, Eur. Polym. J. 44 (2008) 3741–3747.

11- Chemical Synthesis and Characterization of Polyaniline Films using Fenton Reagent M.M. Ayad and **E. A. Zaki**, J Appl. Polym. Sci, Vol. 110, 3410–3419 (2008).

12- Determination of the dopant weight fraction in polyaniline films using a quartz Crystal microbalance, M.M. Ayad, J. Stejskal and **E. A. Zaki**, Thin Solid Films, 515 (2007) 8381– 8385.

(*equal contribution)

Talks

Adsorption of CO and water on magnetite Fe_3O_4 surfaces **E. Zaki**, F. Mirabella, F. Ivars-Barceló, J. Seifert, S. Carey, S. Shaikhutdinov, H.-J. Freund, The 33^{rd} European Conference on Surface Science (ECOSS- 33), Szeged, Hungary, from 27 August – 1 September 2017.

Posters

Adsorption of H_2O and CO_2 on Fe_3O_4 Surfaces, **Eman Zaki**, Shamil Shaikhutdinov, Hans-Joachim Freund., Japan-Germany joint symposium (FHI-JST joint Symposium) "Current Topics and Challenges for Innovative Catalysts" Harnack-Haus, Fritz-Haber-Institut der Max-Planck-Gesellschaft–Berlin - 31.10.2018 – 2.11.2018.

Adsorption of H_2O and CO_2 on Fe_3O_4 Surfaces, **Eman Zaki**, Shamil Shaikhutdinov, Hans-Joachim Freund., The 34^{th} European Conference on Surface Science (ECOSS-34), Aarhus, Denmark, from the $26^{th}$to the 31^{st} of August 2018.

The poster win ECOSS-34-EPS Poster Prize.

H_2O and CO_2 adsorption on Fe_3O_4 Surfaces, **Eman Zaki**, Shamil Shaikhutdinov, Hans-Joachim Freund., International Symposium of the Collaborative

Research Center 1109, "Metal Oxide – Water Systems" Erkner, February 19-22, 2017.

Adsorption of H_2O and CO_2 on Fe_3O_4 surfaces as studied by TPD, **Eman Zaki**, Xuefei Weng, Shamil Shaikhutdinov, Hans-Joachim Freund., CRC 1109 Summer School, Berlin, Germany, from 22 to 25 of August 2016.

Aknowledgements

I am deeply indebted to Prof. Hans-Joachim Freund for giving me the opportunity to join the Department of Chemical Physics at the Fritz-Haber-Institute of the Max Planck Society (FHI) and being my Ph.D. supervisor. I am also thankful to my second supervisor Prof. Dr. Reinhard Schomäcker at the Technical University Berlin for his kind support. I owe a great debt of gratitude to Dr. Shamil Shaikhutdinov, daily scientific advisor, whose comments, and expertise have always been helpful and appreciated.

I would like to extend my deepest gratitude to Prof. Ernst Bauer, with whom I had the pleasure to work with briefly during my Ph.D., for his substantial encouragement and advice.

I am greatly thankful to Xiaoke Li, Joachim Paier and Prof. Joachim Sauer in the Humboldt University of Berlin for their theoretical collaboration.

As our department secretaries, Frau Manuela Misch and Frau Daniela Nikolaus deserve thanks for their kind support and guidance, which ensured that all the administrative processes went very smoothly.

I want to thank Uwe Härtel, Jens Hartmann, Klaus-Peter Vogelgesang, Burkhard Kell, Matthias Naschitzki and Walter Wachsmann for their assistance and technical support.

I gratefully acknowledge the funding from CRC 1109 (The Collaborative Research Centre funded by the DFG 2014 – 2018) and IMPRS (International Max Planck Research School) that made my Ph.D. work possible. I would particularly like to thank Frau Ines Bressel and Dr. Alexander Paarmann for their support and concern.

My appreciation also to all my colleagues in the Chemical Physics department that I have had the pleasure to work with or alongside. To name a few: Dr. Qiushi Pan, Dr. Jagriti Pal, Adrián Lewandowski, Dr. Georg Simon,

Leonard Gura, Dr. Zechao Yang, Dr. David Kuhness, Dr. Patrik Marschalik, Dr. Linfei Li, Dr. Xuefei Weng, Zhang Ke, Agata Plucienik, Kristin Werner, and Dr. Héloise Tissot.

My utmost gratitude to my family for all their countless love, support, and encouragement.

Thank you, everyone!!!